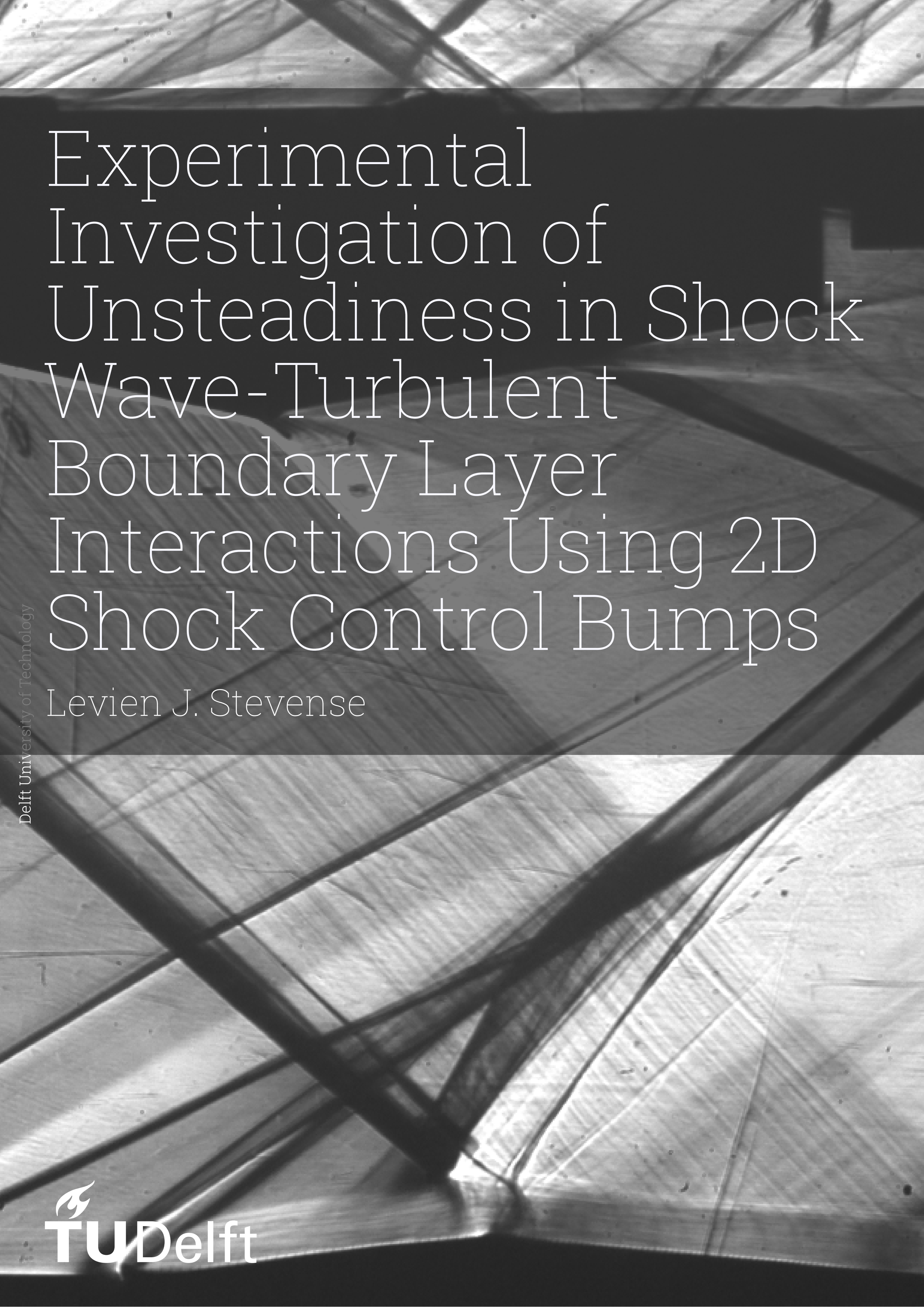

Experimental Investigation of Unsteadiness in Shock Wave-Turbulent Boundary Layer Interactions Using 2D Shock Control Bumps

Levien J. Stevense

Delft University of Technology

Experimental Investigation of Unsteadiness in Shock Wave-Turbulent Boundary Layer Interactions Using 2D Shock Control Bumps

by

Levien J. Stevense

to obtain the degree of Master of Science
at the Delft University of Technology,
to be defended publicly on the 21st of February 2025 at 11:00.

Student number:	5651964	
Project duration:	18 June 2024 - 21 February 2025	
Assessment Committee:	Dr. ir. B.W. van Oudheusden	TU Delft, chair
	Dr. ir F.F.J. Schrijer	TU Delft, daily supervisor
	J. Bulut	TU Delft, supervisor
	Prof. Dr. S. Hickel	TU Delft, external member
	Dr. ir. W.J. Baars	TU Delft, external member
Faculty:	Aerospace Engineering	

TU Delft

Preface

Who would have thought: I am graduating with a master's degree in Aerodynamics from the Technical University of Delft. If you told the 17-year-old me this, he would say, 'Are you joking?'

I have always been an aviation enthusiast. From the age of four, I wrote reports at primary school in which I wondered about the art of flying. The logical educational path for me was to pursue a career in aviation. I have a BSc in Flight Operations Engineering from the University of Applied Sciences Amsterdam which gave me insights into aviation but, unfortunately for me, no theory behind it. This is why I have decided to continue my studies at the TU Delft.

After having completed this master's thesis, only one word comes to mind to describe everything. Proud. I am so proud that I accomplished this, purely by motivation, perseverance, and studying very hard. From starting at VMBO/HAVO level at high school, I did not know I had what it takes to accomplish something this significant. It only proves to me that everything is possible as long as you believe in yourself.

I want to thank my supervisors Dr. ir. F.F.J. Schrijer, Dr. ir. B.W. van Oudheusden, and J. Bulut for their invaluable input during the thesis. I would also like to thank the technicians for their help during the wind tunnel experiments. Finally, I want to thank my girlfriend for her continuous mental support during the process and just being there for me. She can relate to what I was doing from beginning to end and she gave me helpful advice which I appreciated immensely. I will join her in pursuing our aerodynamic careers while living abroad and I am really looking forward to it.

Levien J. Stevense
Delft, February 2025

Summary

During high-speed aerodynamic applications, the interaction between shock waves and boundary layers becomes inevitable. The Shock Wave-Boundary Layer Interaction (SWBLI) is associated with unsteady fluctuations of the separation shock, thickening of the boundary layer, and possibly flow separation. The unsteadiness is often characterised by frequencies two to three orders of magnitude lower than fluctuations of the boundary layer, and the origin of this low-frequency unsteadiness is unknown. The effects associated with SWBLIs occur on transonic aircraft wings and supersonic engine inlets, so the control of this phenomenon is of high importance. Shock Control Bumps (SCBs) are a potential candidate for these applications, and their working principle is based on replacing the separation bubble with a solid object. They have been investigated extensively in the context of normal shock waves and their performance, but not for oblique shock waves and the changes in unsteadiness. Therefore, the aim of this research is to experimentally investigate on a fundamental level the changes in unsteadiness of an oblique SWBLI with a turbulent boundary layer and the implementation of a 2D-SCB. Although the origin of unsteadiness is unknown, it is assumed that a downstream mechanism with its origin in the separation bubble drives the unsteady fluctuations of the interaction.

Schlieren and oil flow measurements were performed in the ST-15 supersonic wind tunnel at the High Speed Laboratory at the Technical University of Delft. The unsteady behaviour was quantified through spectral analysis using Welch's method and a Canny-based edge-detection algorithm. The inviscid oblique SWBLI model and its isobaric boundary form the basis of the bump design. The boundary was approximated for a Mach 2 flat plate flow with an impinging shock strength of $\phi = 12°$, and this design was referred to as the baseline bump. The experimental campaign was divided into two investigations. Campaign A focussed on the spanwise design of the baseline bump to mitigate corner effects in the wind tunnel. Furthermore, it investigated the impingement location of the incident shock and the effect on unsteadiness for the interaction with a baseline bump. The bump with nominal two-dimensional behaviour was selected for campaign B. This campaign aimed to observe possible trends in the individual geometry variation of the ramp and tail angle.

The results of campaign A revealed that an uncontrolled interaction could successfully be reciprocated. Oil flows showed a well-defined separation bubble, and spectral analysis computed a range of low-frequencies of $0.02 \leq St_{L_{int}} \leq 0.09$ where $St_{L_{int}} = fL/u_\infty$ is the normalised frequency or interaction length-based Strouhal number. This is in line with the $St_{L_{int}} \approx 0.03$ reported in literature. A spanwise baseline bump design which spanned the entire wind tunnel test section showed the most two-dimensional behaviour, and the spectral analysis showed that the low-frequency content was removed. It does so by effectively replacing the separation shock with a compression ramp shock such that the boundary layer is subjected to a pressure gradient of the compression ramp shock rather than the impinging shock.

Campaign B showed that an increase in ramp angle generated unsteady behaviour upstream of the bump leading edge, but no characteristic frequencies of the uncontrolled interaction were obtained. Oil flows confirmed that a bubble of recirculation was generated in this region. It is hypothesised that the boundary layer becomes increasingly subjected to the impinging shock pressure gradient rather than the compression-ramp pressure gradient. This allows for a separation shock to be formed as well as a separation bubble, but this bubble is restricted by the bump leading edge. This does not allow for the bubble to fully evolve the unsteady dynamics. The increase in tail angle revealed compression wave formation on the tail part but no changes in interaction unsteadiness compared to the baseline bump. Local compression of the streamlines due to the short tail section is suspected to generate these compression waves. A downstream impingement relative to the bump crest resulted in local recirculating flow downstream of the bump crest with no change in unsteadiness. Upstream impingement resulted, similarly to the ramp angle variation, in a separation shock formation with frequencies trending towards the low-frequency unsteadiness of the uncontrolled interaction.

Although the spectral analysis demonstrated more conclusive results, the edge-detection algorithm performed poorly due to noise levels in the Schlieren images. The standard deviations associated with the impinging shock wave were around $\sigma/\delta_0 \approx 0.2$ for all bump cases suggesting that image noise influences the results significantly. The noise can be classified as the measurement uncertainty of the Schlieren technique. No conclusions could be drawn from the edge-detection results even though such a method has the potential to work properly with further optimisation. For future research, it is suggested to extend the efforts of the edge-detection algorithm to mitigate noise in Schlieren images. Furthermore, a different experimental technique can be applied to obtain centred-interaction information rather than spanwise integrated results from the Schlieren technique. Numerical results through Large Eddy Simulation (LES) or Direct Numerical Simulation (DNS) can be used to conduct a verification and validation study and obtain a more detailed flow analysis of the unsteady dynamics. An integrated approach combining 2D-SCBs with an industrial application would be beneficial in fully realising the performance advantages of these bumps for variations in unsteady dynamics.

Contents

List of Figures

List of Tables

Nomenclature

Abbreviations

Abbreviation	Definition
DNS	Direct Numerical Simulation
F	Focal point
LE	Leading Edge
LES	Large-Eddy Simulation
N	Nodal point
PIV	Particle Image Velocimetry
PSD	Power Spectral Density ($P(f)$)
SCB	Shock Control Bump
SWBLI	Shock Wave-Boundary Layer Interaction
SWTBLI	Shock Wave-Turbulent Boundary Layer Interaction
S	Saddle point
TE	Trailing Edge

Symbols

Symbol	Definition	Unit
H_i	Incompressible shape factor	[-]
I	Intensity of light	[-]
K	Gladstone-Dale constant, number of periodograms	[m^3/kg], [-]
L	Characteristic length, length of periodogram	[m], [-]
L_{int}	Interaction length	[m]
M_∞, M	Free-stream Mach number, Mach number	[-], [-]
N	Number of observations in a signal	[-]
$P(f)$	Power spectral density of $X(f)$	[W/Hz]
Re	Reynolds number	[-]
$St_{L_{int}}$	Interaction length-based Strouhal number	[-]
T, T_0	Static temperature, total temperature	[K], [K]
$X(f)$	Fourier transform of a time signal $x(t)$	[-]
a	Speed of sound	[m/s]
$c_{f,0}$	Free-stream friction coefficient	[-]
f	Frequency, focal length	[Hz], [m]
f_s	Sampling frequency	[Hz]
h	Height of Shock Control Bump	[m]
k	Reynolds number dependent constant for free-interaction theory	[-]
l	Length of Shock Control Bump	[m]
n	Refractive index	[-]
p, p_0	Static pressure, total pressure	[Pa], [Pa]
u	Streamwise velocity	[m/s]
u_τ	Wall-friction velocity	[m/s]
u_∞	Free-stream velocity	[m/s]
w	Width of Shock Control Bump	[m]
x	Streamwise direction	[m]

Symbol	Definition	Unit
x_0	Interaction origin	[m]
y	Wall-normal direction	[m]
z	Spanwise direction	[m]
Δ	Difference between two quantities	[-]
β	Shock wave angle	[°]
γ	Ratio of specific heats	[-]
δ	Boundary layer thickness	[m]
δ_0	Free-stream boundary layer thickness	[m]
δ_i^*	Incompressible displacement thickness	[-]
ϵ	Uncertainty, light ray deflection angle	[m],[°]
θ_i^*	Incompressible momentum thickness	[-]
θ_r	Ramp angle of Shock Control Bump	[°]
θ_t	Tail angle of Shock Control Bump	[°]
μ	Dynamic viscosity	[Pa s]
ρ	Density	[kg/m^3]
σ	Standard deviation	[-]
σ_I	Standard deviation of the pixel intensity	[-]
τ	Shear stress	[Pa]
ϕ	Flow deflection angle	[°]

1

Introduction

Shock waves become inevitable when the velocity of an object travelling through air is higher than the speed of sound. When these shock waves interact with the turbulent boundary layer on the object, an interaction will be generated referred to as a Shock Wave-Turbulent Boundary Layer Interaction (SWTBLI). These interactions occur on transonic commercial aircraft wings, in supersonic engine inlets, and at compressor/turbine blades of an aircraft engine (Sabnis and Babinsky, 2023). The significance of these interactions becomes evident through analysis of their behaviour, and its result frequently consists of high local heat transfer, low-frequency unsteadiness of the separation shock, and substantial downstream flow separation (Sabnis and Babinsky, 2023). The need for flow control of this interaction is highly desirable as these effects are detrimental to aerodynamic performance.

The dynamics of a SWTBLI can be explained using Figure 1.1 which shows a flat plate oblique SWTBLI. When an incident shock impinges on a surface and is strong enough to separate the boundary layer, a separation shock will be generated. This shock intersects the incident shock and a refraction into a reflection and transmitted shock is generated. The transmitted shock penetrates the separated boundary layer and reflects as an expansion fan on the separation bubble due to the near-constant pressure level in this bubble (Babinsky and Harvey, 2011). As a result, the boundary layer flow is deflected towards the wall. The shear layer emanating from the separation point reattaches again, and a reattachment shock will be generated in the reattachment region. The downstream boundary layer has thickened causing it to be less resistant against flow separation.

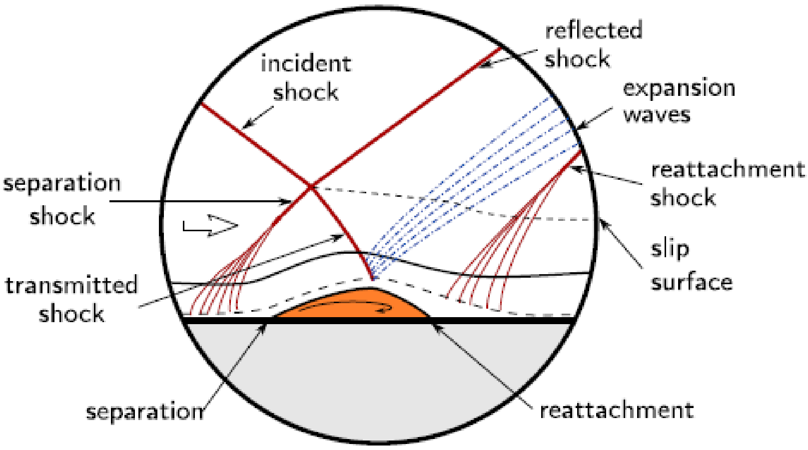

Figure 1.1: Sketch of a flat plate oblique shock wave-turbulent boundary layer interaction for a well-separated interaction (Sabnis and Babinsky, 2023).

This is an example of a well-separated SWTBLI, but interactions with no separation or no mean separation can be generated as well. These are called weak and incipient SWTBLIs respectively, and mostly depend on the status of the upstream boundary layer and incident shock strength (Clemens and Narayanaswamy, 2014). In extreme cases, the flow might not reattach and generate fully separated flow downstream of the interaction. Such interactions can result in highly unsteady flows, potentially causing adverse effects like buffeting on transonic airfoils or inlet instability in supersonic engines (Sabnis and Babinsky, 2023). Moreover, the unsteadiness of SWTBLIs spans a broad frequency range, which may induce metal fatigue or even structural failure in aircraft components (Clemens and Narayanaswamy, 2014). The SWTBLI also occurs on, for instance, blunt fins or compression corner flows, and they entail comparable flow dynamics (Babinsky and Harvey, 2011).

Research on SWTBLI unsteadiness has demonstrated that the interaction is characterised by fluctuations of the shock upstream of the separation point, i.e. the separation shock (Dussage et al., 2005). The associated frequencies are often two to three orders of magnitude smaller than the fluctuations in the upstream turbulent boundary layer (Souverein et al., 2013), and its source, or driving mechanism, is still under debate (Clemens and Narayanaswamy, 2014). Literature seems to agree that the low-frequency unsteadiness occurs at the nondimensionalised frequency, i.e. Strouhal number, of $St_{L_{int}} = \frac{fL_{int}}{u_\infty} \approx 0.03$. This frequency is normalised based on the interaction length which represents the distance between the inviscid impingement and separation location. Such a scaling was originally proposed by Erengil and Dolling (1991). Further experimental and numerical investigations confirmed to have found the same Strouhal number (Pasquariello et al. (2017), Dupont et al. (2006), Wu and Martín (2008), Touber and Sandham (2009)). A comparison of interactions in different geometrical settings by Dussage et al. (2005) found, despite some scatter in the data, a general Strouhal similarity. This suggests that low-frequency unsteadiness is to some extent independent of the interaction geometry. These findings are valid for well-separated SWTBLIs, and differences are observed for weak, incipient, and fully separated interactions (Souverein et al., 2013).

To this day, the exact driving mechanism of the low-frequency unsteadiness remains unknown. Various models have been proposed, and these can be mainly divided into upstream effects, downstream effects, or the coexistence of the two. The hypothesis for upstream effects, or *amplifier models* (Poggie et al., 2015), is that superstructures or velocity fluctuations in the upstream boundary layer drive the unsteadiness of the separation shock. Experimental investigations by Ganapathisubramani et al. (2007, 2009) argued that superstructures as long as 40 times the boundary layer thickness δ are present in the upstream turbulent boundary layer and excite low-frequency unsteadiness. This upstream behaviour was confirmed by Touber and Sandham (2009), but Souverein et al. (2010) noted that this effect weakened as the interaction length increased.

Downstream effects, or *oscillator models* (Poggie et al., 2015) argue that global and/or local instabilities from the separation bubble/reattachment zone induce the unsteadiness. For instance, the acoustic feedback model by Pirozzoli and Grasso (2006) argued that there is an acoustic resonance through the subsonic part of the boundary layer between the interaction of the transmitted shock and the upstream separated boundary layer. This then generates unsteady behaviour and serves as a continuous forcing. On the other hand, Pipponiau et al. (2009) proposed a mass-entrainment model where the shedding of vortices in the shear layer emanating from the separation point generates a periodic 'breathing' of the separation bubble. Finally, observations by Loginov et al. (2006) argued that Görtler-like vortices were present downstream of the interaction. Further investigations by Hu et al. (2022) and Pasquariello et al. (2017) confirmed the existence of these vortices and found strong correlations with the low-frequency unsteadiness. Fan et al. (2024) argued that upstream and downstream effects are coexistent in the interaction while investigating a compression ramp SWTBLI. Hence, the origin of low-frequency unsteadiness remains unclear, and it seems to be dependent on the magnitude of the interaction.

While the origin of unsteadiness remains a question, investigating the control of the interaction is of high interest. The interaction can be controlled by influencing the shock system characteristics or improving the health of the boundary layer, and this can be done actively or passively. Active control systems such as micro and plasma jets are successful ways of mitigating the SWTBLI detrimental effects, but these require an external source of energy (Jana and Kaushik, 2022). A different passive flow control technique is the surface bump, or Shock Control Bump (SCB), which has the objective of suppressing the boundary layer separation by 'filling up' the separation bubble of the interaction (Bruce and Colliss, 2015). This device can act both as a means to control the shock system and the status of the boundary layer (Bruce et al., 2014), and they can have a two- and three-dimensional shape. Figure 1.2 shows a sketch of the flow structure for an uncontrolled normal SWTBLI and compares it to the implementation of an SCB. Figure 1.2a shows the uncontrolled interaction with the compression waves coalescing in the normal shock. Figure 1.2b shows the interaction with a rounded SCB, and it can be seen that the normal shock near the surface is transformed into a set of compression waves. This increases the total pressure recovery near the surface and reduces the imposed adverse pressure gradient. Figure 1.2c shows a bump where the crest is positioned downstream, and it generates a λ-shock structure. The replacement of the normal shock by two oblique shocks near the bump increases the total pressure recovery and reduces the imposed pressure gradient.

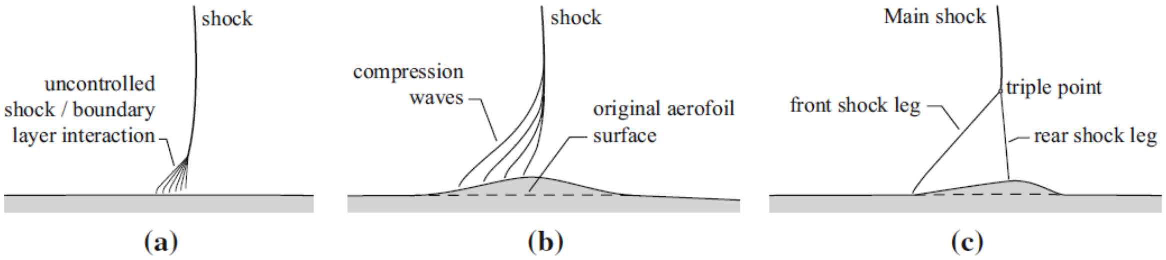

Figure 1.2: Sketch of the effect of SCBs on the uncontrolled normal SWTBLI: a) uncontrolled interaction, b) rounded bump interaction, and c) interaction with a downstream crest (Bruce and Colliss, 2015).

Ogawa and Babinsky (2008) and Ogawa et al. (2008) performed research into different three-dimensional shapes of the SCB in transonic and supersonic normal SWTBLIs conditions. They observed that an array of carefully positioned 3D-SCBs resulted in the highest reduction in wave drag while obtaining little viscous penalty. This was analysed during 'on-design' conditions, i.e. when the bump fills the separation bubble optimally, but 'off-design' conditions showed significant increases in both wave and viscous drag. This was also observed by Colliss et al. (2016) where the flow structure showed signs of downstream separation or local separation bubbles. Not only is the impingement location of the incident shock of importance, but the height of the bump is vital for the production of streamwise vortices in the vicinity of the downstream boundary layer. The study by Colliss et al. (2016) suggested that the front of the bump is a primary driver of the vortex generation in SCBs, and they hypothesised that bumps can be used as a shock and boundary layer control device. However, each bump has specific changes in aerodynamic performance making it complicated to implement bumps on a wide range of applications. Therefore, Bruce and Colliss (2015) state that the true potential of SCBs lies in an integrated approach of next-generation wings and these bumps.

In that case, it is important to understand the effect of the SCB on the low-frequency SWTBLI unsteadiness. The bumps have largely been investigated in terms of their performance benefits for normal shocks, but no real efforts have been made yet towards the changes in unsteadiness in oblique shock situations. Bulut et al. (2023, 2024) made efforts by investigating 3D-SCBs at supersonic conditions while changing the impingement position and ramp shape of the bump. As expected, a variance of incident shock position showed a negative impact on the effectiveness of the bump although the bumps fulfilled their objective of removing separation in the interaction (Bulut et al., 2024). The variance of the ramp shape showed that turbulence intensity levels increased when the ramp part was shortened, but due to the three-dimensional nature of the geometry and its flow structure, no conclusion could be drawn on the alteration in unsteadiness (Bulut et al., 2023). Missing et al. (2024) developed a separation-bubble-shaped SCB of an oblique SWTBLI at Mach 2 to investigate its effect on suppression of the separation bubble breathing of the interaction. Through Schadowgraphy and Particle Image Velocimetry (PIV), it was observed that the bump removed the low-frequency unsteadiness. The bump had an irregular shape, so it would be beneficial if 2D-SCBs were investigated while altering the SCB shape. In this way, the flow dynamics can be understood fundamentally while a possible explanation can be provided for the driving mechanisms in well-separated oblique SWTBLIs.

The purpose of this thesis is to experimentally investigate the unsteady behaviour of an impinging SWTBLI while implementing a 2D-SCB at Mach 2 and a shock strength of $\phi = 12°$. It aims to identify the effect of the 2D-SCBs on the unsteady behaviour and determine if the bumps are an effective way to reduce SWTBLI low-frequency unsteadiness. Furthermore, the shape of the SCB is varied through their ramp and tail angle to observe the individual effect of SCB shape on the overall unsteady dynamics. Schlieren and oil flow visualisations are used to assess these dynamics. It is initially suspected that the driving mechanism of low-frequency separation shock unsteadiness originates from the separation bubble breathing. In essence, the research objective is:

To identify the suitability of a 2D-SCB and its shape as a passive flow control technique for the unsteadiness of oblique SWTBLIs by using High-Speed Schlieren and Oil Flow Visualisations at supersonic conditions.

This research aims to answer the following questions:

1. How does the 2D-SCB affect the unsteadiness of an oblique SWTBLI?
    (a) What is the effect of changing the ramp angle on the SWTBLI unsteadiness?
    (b) What is the effect of changing the tail angle on the SWTBLI unsteadiness?
2. How does the impingement location on the 2D-SCB affect the unsteadiness of oblique SWTBLI?
3. What is the suitability of 2D-SCBs as a passive flow control technique in reducing the unsteadiness of oblique SWTBLI?
4. What are the driving mechanisms of unsteadiness in well-separated oblique SWTBLIs?

To answer these research questions, the thesis will have the following structure. Relevant literature for general SWTBLIs, flow control, and unsteadiness will be reviewed in Chapter 2 including the working principles of the experimental techniques. The methodology of the experimental campaign will be given in Chapter 3 and the results and discussion will be given in Chapter 4. Finally, the conclusion and recommendations for future research will be presented in Chapter 5.

2

Literature Review

The theory needed to conduct this research will be discussed in this chapter. This will be divided into the fundamentals of SWBLIs (section 2.1), their unsteady characteristics (section 2.2), the SCBs (section 2.3), and the intended measurement techniques (section 2.4).

2.1. Fundamentals of Shock Wave-Boundary Layer Interactions

At the basis of this research lies the interaction between shock waves and boundary layers. Subsection 2.1.1 will state the foundation of these aspects, and subsection 2.1.2 will elaborate on their combination.

2.1.1. Shock Waves and Boundary Layers

Shock waves will be generated in compressible flows where the velocity is higher than the speed of sound. The fluid velocity is usually quantified in terms of Mach number which is defined as $M = u/a$ where u is the local fluid velocity and a is the local speed of sound. These waves are phenomena where flow is compressed into a thin region, and the coalescence of compression waves forms the shock wave. This process changes the flow properties like density (ρ), velocity, pressure (p), temperature (T), and entropy (s) almost discontinuously. This process is generic, but the change in magnitude of the flow properties depends on the strength and type of shock wave. This can be in the form of a normal wave, oblique wave, shear wave, or contact discontinuity. A combination of oblique waves (waves which imping walls at an angle) and normal waves (waves which imping the wall perpendicularly) is shown in the converging-diverging nozzle in Figure 2.1. There, supersonic flow ($M_1 > 1$) enters the nozzle and leaves in a subsonic state ($M_2 < 1$). The associated entropy increases over the nozzle, and the total pressure reduces. This principle is frequently used in supersonic engine inlets to reduce the fluid velocity to an optimal range of the engine.

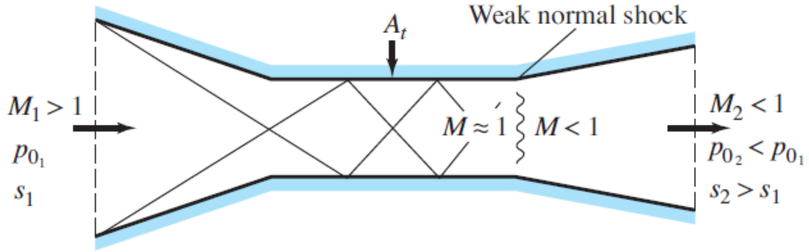

Figure 2.1: Visualisation of a supersonic flow through a nozzle with oblique and a weak normal shock wave (Anderson, 2017).

Apart from changing the characteristics of the flow, shock waves also change the flow direction by an angle ϕ. This angle is intrinsic to oblique shock waves while normal shock waves do not alter the flow direction. The shock strength can be quantified in terms of the change in pressure (p_2/p_1), total pressure recovery across the shock wave (p_{0_2}/p_{0_1}), or the imposed flow deflection angle. As the Mach number increases, the shock wave becomes stronger with a higher ratio of p_2/p_1 and an increase in flow deflection angle. This can be quantified using the $\phi - \beta - M$ relation in Equation 2.1 (Anderson, 2017) where the flow deflection angle can be calculated using the pre-state Mach number M_1, shock wave angle β, and the specific heat ratio $\gamma = 1.4$ (for air). The angle β is defined as the angle between the pre-state Mach number and the oblique shock wave

$$\tan\phi = 2\cot\beta\frac{M_1^2\sin^2\beta - 1}{M_1^2\left(\gamma + \cos 2\beta\right) + 2}. \tag{2.1}$$

Whereas flow is compressed through shock wave formation, flow can also expand through an *expansion region*. Such a region consists of an infinite number of Mach waves each having a Mach angle $\mu = \arcsin(1/M)$. An expansion fan is bounded by two expansion waves having a Mach angle μ_1 and μ_2, and the entropy of the flow does not change when traversing through a Mach wave. Hence, an expansion region is isentropic which is the opposite of shock waves (Anderson, 2017). Shock waves and expansion regions generate *wave drag* which is a result of the increase and decrease of pressure imposed by the compression and expansion regions. The generation of wave drag is in general not desired for aerodynamic applications.

There is also the distinction between inviscid and viscous flows. The latter gives rise to the presence of *boundary layers* which are characterised by a thin layer close to the object in which there is a gradient in velocity and temperature. At the wall, the velocity is zero (no-slip condition) and it increases to 99% of the free-stream velocity. The distance above the wall where this is achieved is called the boundary layer thickness (δ_{99} or simply δ). Due to the velocity gradient at the wall, a retarding shear stress τ_{wall} is generated. In addition, there is an adverse pressure gradient (i.e. the pressure increases in the downstream direction) which also acts as a retarding force to the boundary layer. Both effects cause the boundary layer flow to reverse and increase the boundary layer thickness (Babinsky and Harvey, 2011). A continuous increase can cause flow separation which is, in general, unfavourable. Figure 2.2 visualises the evolution of a boundary layer in terms of its velocity profile due to frictional and pressure forces at three different stations along a wall. It can be seen that the flow reverses its direction once it traverses from s_1 to s_3.

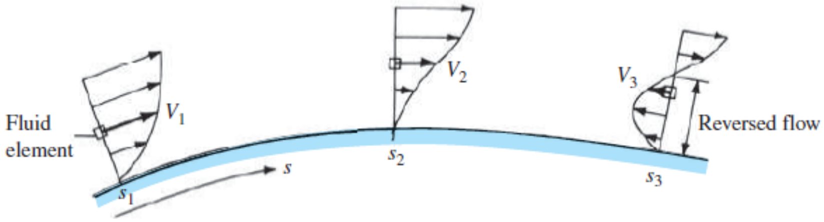

Figure 2.2: Sketch of the evolution of a boundary layer due to shear stresses and an adverse pressure gradient (Anderson, 2017).

The characteristics of boundary layers can be further quantified in terms of the incompressible displacement thickness δ_i^*, momentum thickness θ_i^*, and its shape factor H_i (Equation 2.2). In this equation, u_∞ is the free-stream velocity and y_1 is an arbitrary location outside the boundary layer. The equations are presented in the incompressible form since the response of the boundary layer due to a shock depends on the velocity distribution rather than the compressibility of the flow (Babinsky and Harvey, 2011). The displacement thickness is a parameter which indicates the displacement of the external flow streamlines due to the presence of the boundary layer. The momentum thickness is, in a similar way, the deficit in momentum under the presence of the boundary layer (Anderson, 2017). The shape factor is then defined as the ratio between the displacement and momentum thickness which serves as a quantification of the 'health' of the boundary layer. Health refers to the ability of the boundary layer to resist flow separation when subjected to shear stresses and an adverse pressure gradient. When H_i is small, the velocity profile is more similar to that of the velocity profile at s_1 in Figure 2.2. If H_i increases, the 'health' is degraded and flow is reversed (Babinsky and Harvey, 2011).

$$\delta_i^* = \int_0^{y_1} \left(1 - \frac{u}{u_\infty}\right) dy, \quad \theta_i^* = \int_0^{y_1} \frac{u}{u_\infty} \left(1 - \frac{u}{u_\infty}\right) dy, \quad \text{and} \quad H_i = \frac{\delta_i^*}{\theta_i^*}. \tag{2.2}$$

Finally, the characteristics of the boundary layer can be further divided into a laminar or turbulent state. The main difference is, as can be seen in Figure 2.3, the shape of the velocity profile. The laminar boundary layer has lower flow momentum compared to the turbulent layer such that the laminar layer is less resistant to the retarding shear stress and pressure gradient forces (White and Majdalani, 2022). Considering boundary layers in supersonic conditions, there is a *sonic point* at a distance above the wall where the local Mach number is one. When this point is relatively high, the region of low-momentum fluid is large such that the boundary layer is more prone to flow separation. The opposite is true when the sonic point is low. Hence, turbulent supersonic boundary layers which have a sonic point closer to the wall will be more resistant to flow retardation and show flow reversal at a later stage compared to laminar supersonic boundary layers (Babinsky and Harvey, 2011). The shape of the velocity profile and the growth of the layer in the streamwise direction depends strongly on the Reynolds number $Re = \frac{\rho u L}{\mu}$ which represents the ratio between the inertial and viscous forces of the flow. There, L is the characteristic length and μ is the dynamic viscosity. When the Reynolds number increases, the momentum in the boundary layer increases. However, the *transition* from a laminar to a turbulent layer occurs relatively earlier. Finally, the growth of the layer in the streamwise direction reduces as the Reynolds number increases (Anderson, 2017).

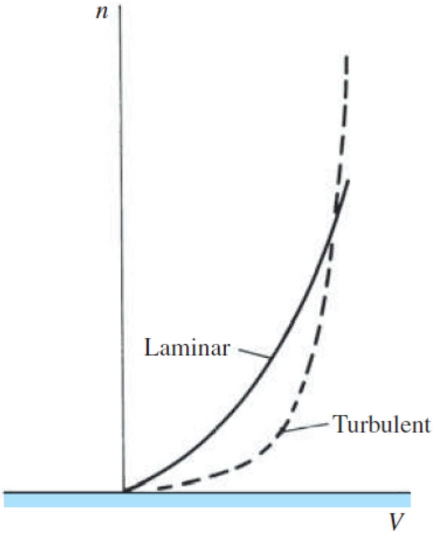

Figure 2.3: Comparison of the velocity profile between a laminar and turbulent boundary layer (Anderson, 2017).

2.1.2. Shock Wave-Boundary Layer Interaction

As discussed in subsection 2.1.1, it is evident that the behaviour of shock waves and boundary layer depends on several parameters. The interaction of these two in Shock Wave-Turbulent Boundary Layer Interactions (SWTBLIs) can be best understood by considering Figure 2.4. This figure shows a typical SWTBLI for an oblique shock on a flat plate.

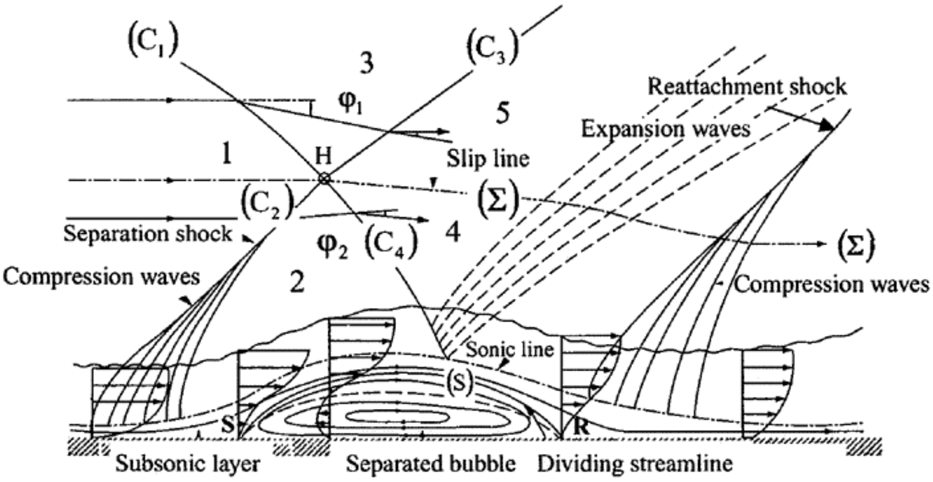

Figure 2.4: Sketch of a typical oblique SWTBLI with a separation bubble (Babinsky and Harvey, 2011).

The physical mechanism of a SWTBLI starts with an incoming turbulent boundary layer and an incident shock (or impinging shock) referred to as (C_1). The shock induces an adverse pressure gradient on the streamlines which intersect the shock wave. Then, the boundary layer thickens as it approaches the incident shock, and it virtually generates a compression ramp for the incoming boundary layer flow. This ramp generates compression waves which coalesce in the separation shock (C_2). Furthermore, the streamlines which cross the incident and separation shock wave are deflected by ϕ_1 and ϕ_2, respectively. The incident and separation shock intersect at point H and are refracted into the reflected shock (C_3) and the transmitted shock (C_4). The streamlines are again deflected due to these shocks. The flow in the boundary layer will reverse and eventually separate at point **S** forming a shear layer, or dividing streamline, *S*. This layer separates the recirculating flow inside the separation bubble from the 'outer' flow going in the streamwise direction. The dividing streamline goes from the separation point to the reattachment point and has a strong mechanical-energy transfer from the 'outer' flow towards the separated flow (Babinsky and Harvey, 2011). The shear layer generates spanwise-oriented vortices which share similarities with the Kelvin-Helmholtz instability (Hadjadj et al., 2010). The pressure in the separation bubble is relatively constant, and the transmitted shock is followed by an expansion wave causing the shear layer to deflect towards the wall. This layer will reattach at point **R** creating a *separation bubble* and a second set of compression waves which coalesce in the reattachment shock. The boundary layer reattaches downstream of the separation bubble and its thickness has increased relative to the incoming boundary layer.

The associated variance in wall pressure is shown in Figure 2.5. This figure shows both the inviscid and viscous pressure distribution for a well-separated oblique SWTBLI. Indeed, for the inviscid solution, the variance in pressure shows a discontinuity at the location of the impinging shock wave $x = 0$. For the viscous solution, the pressure starts to rise at some distance before the inviscid impingement location. This distance is referred to as the upstream influence and has an associated *interaction origin* x_0 (Babinsky and Harvey, 2011). Then, as the point of separation **S** is reached, the pressure shows a plateau-like behaviour, meaning that the pressure remains almost constant within the separation bubble. As reattachment starts, the pressure rises again to the inviscid pressure solution which is often relatively gentle in the downstream direction (Sabnis and Babinsky, 2023). The interaction origin is frequently called the interaction length L_{int}, and the length between separation and reattachment is denoted as L_{sep}.

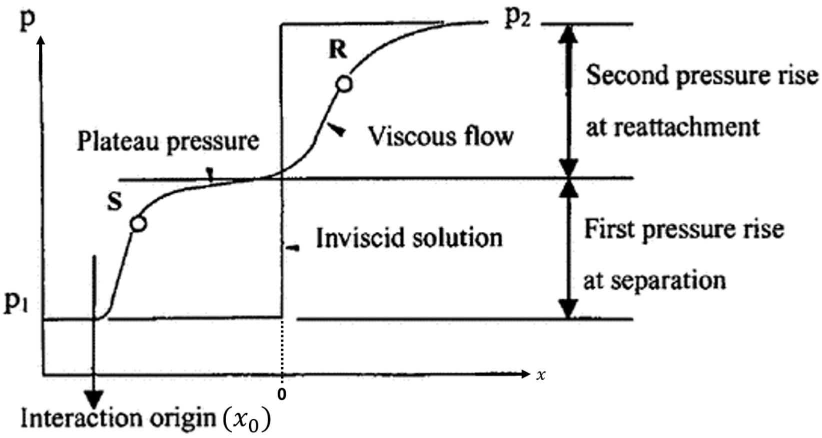

Figure 2.5: Comparison between the inviscid and viscous wall-pressure distribution of an oblique SWTBLI as a function of the streamwise direction x (adapted from Babinsky and Harvey, 2011).

In general, three variants of the SWTBLI can be distinguished (based on the boundary layer status and/or strength of the incident shock, (Clemens and Narayanaswamy, 2014)):

- The *weakly separated* interaction: it induces no boundary layer separation but only thickens it;
- The *incipient* interaction: it induces no mean separation, so the interaction is strong enough to produce a separation bubble but not evident enough; and
- The *well-separated* interaction: it induces strong boundary layer separation with a well-defined separation bubble.

It is also possible for boundary layers to transition within the SWTBLI called *transitional* SWBLI. Furthermore, laminar and turbulent boundary layers can separate during an interaction when the shock wave is strong enough to induce this separation. Hence, the health of the boundary layer and/or strength of the incident shock plays a large role in the SWBLI dynamics.

2.1.3. Free-Interaction Theory

To improve the understanding of the SWTBLI dynamics, an equivalent inviscid flow model can be reconstructed of the generic oblique SWBLI as proposed by Delery (1985). This model replaces the recirculating flow in the separation bubble by a region where the pressure is equal to the plateau pressure in Figure 2.5, i.e. the *dead-air* region. This model is visualised in Figure 2.6.

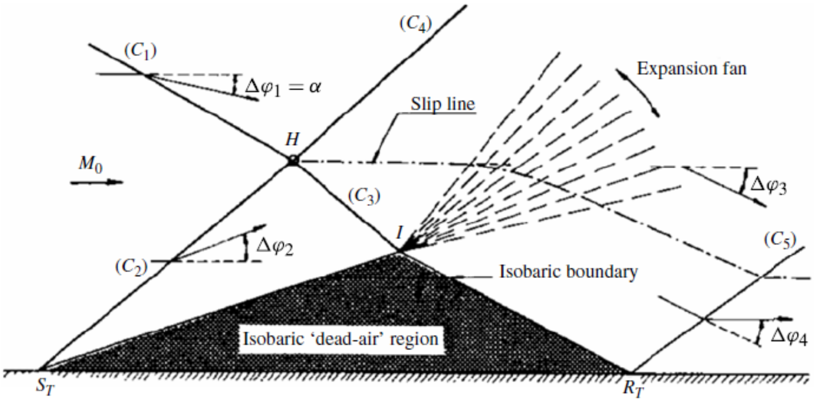

Figure 2.6: Inviscid flow model representation of an oblique SWBLI (Souverein et al., 2013).

The inviscid model comprises the same elements as the viscous SWTBLI in Figure 1.1: the incident shock (C_1) and separation shock (C_2) which intersect at H and each have a flow deflection angle $\Delta\phi_1$

and $\Delta\phi_2$, respectively. A slip line is generated from point H together with the reflection shock (C_3) and the transmitted shock (C_4). To ensure continuity, the pressure rise excited by shock (C_3) must be compensated by the pressure decrease of the centred expansion at point I. Also, the reattachment shock (C_5) makes sure the flow after reattachment is parallel to the wall with an equivalent angle $\Delta\phi_4$. Finally, the separation bubble is now an isobaric or dead-air region with its isobaric boundary. This model holds for a well-separated SWBLI. In this way, the initial pressure rise at separation does not depend on downstream conditions. It is otherwise referred to as a local self-induced free-interaction process, and Chapman et al. (1958) performed a simplified analysis describing this interaction. As a result, Equation 2.3 (Bulut et al., 2023) describes the required increase in pressure Δp_{sep} to excite flow separation. This equation is only a function of upstream influences: the Mach number and the boundary layer friction coefficient $c_{f,0}$. Furthermore, it is dependent on the (momentum thickness-based) Reynolds number-dependent constant k (Souverein et al., 2013). Equation 2.3 argues that the increase in pressure due to the separation shock is only dependent on upstream influences, and extensive research has confirmed this both numerically and experimentally (see e.g. Katzer (2006)).

$$\Delta p_{sep} = k\gamma M_\infty^2 \sqrt{\frac{2c_{f,0}}{(M_\infty^2-1)^{1/2}}}, \quad \text{where} \quad k = \begin{cases} 3.0 : Re_\theta \leq 1\cdot 10^4, \\ 2.5 : Re_\theta > 1\cdot 10^4. \end{cases} \tag{2.3}$$

2.2. Unsteadiness in Shock Wave-Boundary Layer Interactions

A general introduction of unsteadiness will be given in subsection 2.2.1 after which upstream and downstream effects will be discussed in subsection 2.2.2 and subsection 2.2.3, respectively.

2.2.1. General Aspects of Unsteadiness

The fluctuating behaviour or *unsteadiness* of the shock system is an intrinsic effect of SWTBLIs. Often, unsteadiness is observed in the reflected shock, separation shock, and separation bubble region, and it has the detrimental ability to induce vibration on the aerodynamic structure or provide unsteady mass flow rates in supersonic engines (Rohlfs et al., 2022). It is therefore vital to understand the driving mechanisms behind the SWTBLI unsteadiness. However, these driving mechanisms are still not thoroughly understood and discussion exists about the origin of these mechanisms (Clemens and Narayanaswamy, 2014).

Unsteadiness describes the fluctuating behaviour of the shock system through time, and it can be distinguished into low-, medium-, or high-frequency unsteadiness (Sabnis and Babinsky, 2023). The fluctuating behaviour of the SWTBLI can be analysed using spectral analysis methods, and it often includes the nondimensionalisation of the frequency or Strouhal number. This can be used to compare interactions of different magnitudes and geometrical conditions, and it was originally proposed by Erengil and Dolling (1991). The definition of the Strouhal number is given in Equation 2.4 which consists of the frequency f, the interaction length L_{int}, and the free-stream velocity u_∞

$$St_{L_{int}} = \frac{fL_{int}}{u_\infty}. \tag{2.4}$$

In general, Figure 2.7 can be used to give an approximation of the location of the spectral content within a SWTBLI. This figure shows a typical well-separated oblique SWTBLI with annotations of the frequency content in three regions. The upstream region of the SWTBLI is the incoming turbulent boundary layer. This consists of high frequencies originating from the integral-scale turbulent fluctuations which convect and modulate within the incoming boundary layer (Gaitonde and Adler, 2023). The same high-frequency content is observed in the downstream reattached boundary layer downstream of the separation bubble. Low-frequency spectral content is observed within the separated region, and the driving mechanisms of this content are yet under debate. Moreover, it seems that the origin of this driving or forcing is different for weak, incipient, and well-separated SWBLIs (Clemens and Narayanaswamy, 2014).

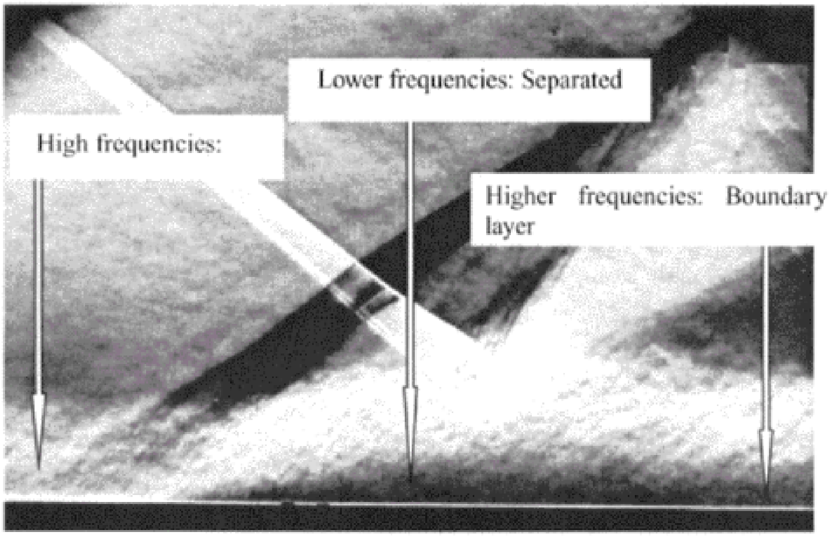

Figure 2.7: Distribution of frequency content within a SWTBLI (Babinsky and Harvey, 2011).

While there are various models which attempt to describe the driving mechanisms of the low-frequency oscillation, there seems to be agreement that it occurs at a ‘universal’ Strouhal number of $St_{L_{int}} \approx 0.03$. Studies such as Pasquariello et al. (2017), Gaitonde and Adler (2023), and Touber and Sandham (2009) support this finding.Dussage et al. (2005) retrieved information from various studies which investigated the low-frequency unsteadiness for different flow cases and concluded that, even though there is some dispersion, most of the experiments identify a Strouhal number of 0.03 – 0.04 at the separation shock. In terms of frequency, it largely depends on the upstream flow properties, the type of SWTBLI, and the dimension of the model geometry (Dolling, 2001). For example, experiments by Erengil and Dolling (1991), of which the results are given in Figure 2.8, reviewed the wall pressure fluctuations in terms of pre-multiplied variance-normalised Power Spectral Densities (PSDs) ($(f \cdot P(f)/\sigma^2$) at various locations of a Mach 5 compression ramp SWTBLI. In line with Figure 2.7, high frequencies occur in the upstream and downstream turbulent boundary layer, and low frequencies are obtained at the location of the separation shock. Often, the terminology of the intermittent region L_i is used to denote the spatial distance in which the separation shock fluctuates. In this case, the high- and low-frequencies occur at around 30-40 kHz and 0.2-0.5 kHz, respectively. In general, there is a difference of two to three orders of magnitude in frequencies between the low frequencies associated with the separation shock and the higher frequencies from the fluctuations in the turbulent boundary layer (Clemens and Narayanaswamy, 2014).

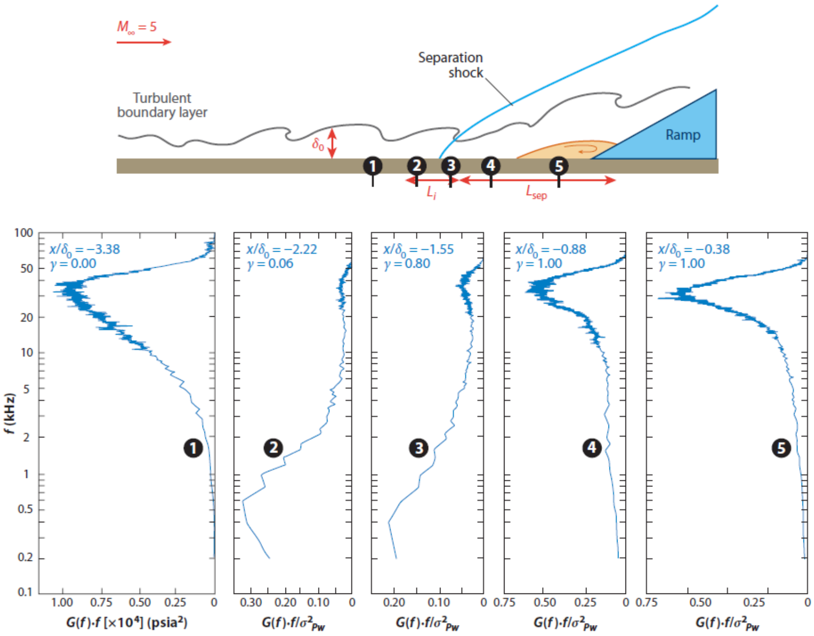

Figure 2.8: Pre-multiplied variance-normalised PSDs of the wall pressure at five locations in a Mach 5 compression ramp SWTBLI (results from Erengil and Dolling (1991), figure from Clemens and Narayanaswamy (2014)).

In all cases, it is argued that both upstream and downstream mechanisms are present which act as a forcing mechanism for the low-frequency shock oscillation (Clemens and Narayanaswamy, 2014). Upstream mechanisms suggest that turbulent fluctuations in the upstream boundary layer excite unsteadiness in the shock system while downstream mechanisms imply that large-scale instabilities generated by the separated flow of the bubble are at the origin of this unsteadiness. Upstream and downstream mechanisms will be reviewed independently, and it will become evident that both mechanisms occur simultaneously despite researchers focussing on a single mechanism in their investigation.

2.2.2. Upstream Effects

As discussed in subsection 2.2.1, upstream mechanisms can be a cause of low-frequency unsteady behaviour in SWTBLIs. Significant research has focused on the upstream boundary layer and its structures, and it is argued that SWTBLI unsteadiness arises from the interaction with these structures and the separation shock wave. Models centred around this principle are often classified as amplifier models (Poggie et al., 2015). For instance, McClure (1992) and Gramann and Dolling (1992) argued that the upstream and downstream movement of the separated shock foot was correlated with decreasing and increasing pitot pressures within the upstream boundary layer, respectively. Beresh et al. (2002) investigated this further using PIV and tried correlating negative and positive velocity fluctuations u' in the upstream boundary layer to the separated shock foot motion. They concluded that, as the boundary layer velocity profile is traversed from its edge towards the wall, the influence of these velocity fluctuations on the shock motion increases. More specifically, in the lower part of the boundary layer, negative velocity fluctuations excite an upstream movement of the shock whereas positive fluctuations excite a downstream movement. Therefore, a fuller boundary layer profile leads to downstream motion, and a more retarded profile leads to an upstream motion of the shock foot. This is visually shown in Figure 2.9. Here, it shows the effect of positive and negative velocity fluctuations in the boundary layer on the shift of the separation shock foot. Despite this, Beresh et al. (2002) concluded that this mechanism does not excite the well-known low-frequency unsteadiness of the separation shock.

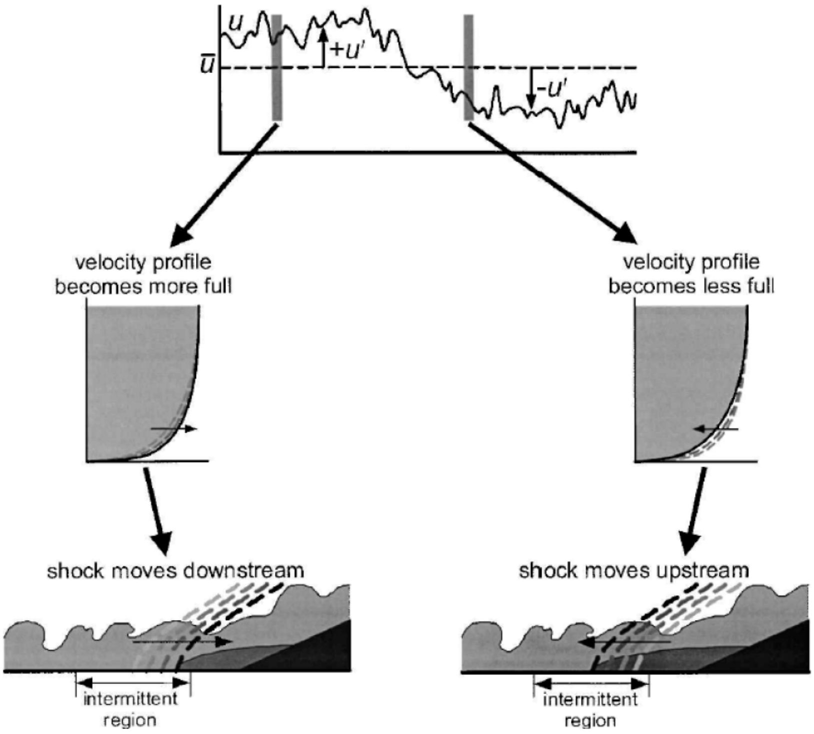

Figure 2.9: Relation between velocity fluctuations in the upstream boundary layer and the translation of the separation shock foot in SWTBLI (Beresh et al., 2002).

Ganapathisubramani et al. (2007, 2009) investigated the two-dimensional upstream boundary layer structure and the effect on the low-frequency unsteady dynamics for a Mach 2 compression ramp flow while employing PIV. One of the results of this research indicated that there are regions of low-velocity fluid located in the log-region that remained coherent for lengths up to 40δ upstream of the separation shock. These then correlated significantly with the streamwise and spanwise fluctuating behaviour of the surrogate separation location. To visualise this, consider Figure 2.10 which shows a u/u_∞-velocity contour plot of the upstream boundary layer. The Taylor hypothesis of frozen turbulence allowed them to reconstruct the upstream velocity profile by shifting recorded velocity plots by the free-stream convection speed. It can be seen that there are relatively large coherent structures of low- and high velocity throughout the entire log-region of the boundary layer. Wu and Martín (2008) investigated a comparable interaction through DNS and argued that the surrogate representation of the separation location does not necessarily represent the true separation. They pointed out that a separation location based on the skin friction coefficient gave a lower correlation with the mass flux fluctuations in the upstream boundary layer.

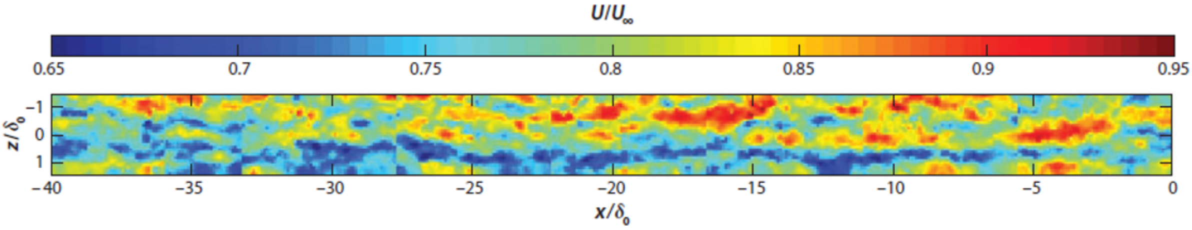

Figure 2.10: Reconstruction of the upstream log-region boundary layer for a Mach 2 compression ramp SWTBLI using PIV and the Taylor hypothesis where the velocity is normalised by the free-stream velocity u_∞ (adapted from Clemens and Narayanaswamy (2014)).

Humble et al. (2009) also investigated the upstream boundary layer using tomographic PIV measurements to obtain an instantaneous three-dimensional velocity field. This allowed them to examine the spanwise and streamwise variances of the separation shock and upstream boundary layer. They found similar low-speed superstructures in the upstream boundary layer and a correlation between the surrogate separation location and upstream velocity fluctuations. It is argued that the streamwise oscillation of the separation location is generated by the bulk momentum changes in the upstream boundary layer (i.e. regions with positive and negative velocity fluctuations) whereas the spanwise organisation of the upstream structures causes spanwise ’wrinkling’ of the separated flow.

In a different approach, Touber and Sandham (2011) developed a first-order mathematical model based on the model by Plotkin (1975). This model describes an excitation mechanism for the convection and restoration of the separation shock position due to velocity fluctuations in the boundary layer and mean flow stability. They observed large-scale motions similar to those in experimental and numerical simulations when introducing white noise. The white noise represented the fluctuations in the turbulent boundary layer. Notably, the low-frequency oscillations were removed when the white noise was high-pass filtered. Thus, it seems that there is a direct correlation between the fluctuations in the upstream boundary layer and the SWTBLI low-frequency unsteadiness.

2.2.3. Downstream Effects

Downstream effects consider the forcing of the low-frequency oscillation through global and/or local instabilities of the separated flow downstream of the separation shock foot. This type of forcing is often classified as an oscillatory model (Poggie et al., 2015). Despite the evidence in favour of upstream mechanisms, Thomas et al. (1994) showed that correlations exist between the reattachment region fluctuations and those in the intermittent region. It was found that the separation and reattachment points moved in opposite directions as the separation bubble expanded and contracted. This indicated that possibly a downstream mechanism can generate the unsteadiness. The findings by Dupont et al. (2006) supported this hypothesis where they found high coherence and phase relation between the separation bubble and separation shock motions. Wu and Martín (2008) confirmed to have found similar coherence between the separation and reattachment point through DNS and argued that large-scale motion of the separation shock can be due to the pulsation of the separated flow while smaller-scale fluctuations can be attributed to upstream boundary layer structures. The pulsation can be generated because of the entrainment of the shear layer and separation bubble recharge rate in the reattachment region.

The possible driving mechanisms argued by Wu and Martín (2008) are similar to the model proposed by Pipponiau et al. (2009). They present a model based on fluid-mass entrainment in the shear layer downstream of the separation point. To illustrate this, consider Figure 2.11 which shows a general SWTBLI with a well-defined separation bubble, the separation shock, and the entrainment in the mixing layer. At the start of the bubble (S), eddies are generated in the mixing layer region and grow as they convect downstream. These eddies are comparable to the coherent motion of Kelvin-Helmholtz-like vortices (Hadjadj et al., 2010). At some point (assumed at half the length of the bubble) the eddies are shed downstream which bring with them mass, momentum and vorticity such that there is a ‘mass deficit’ in the separation bubble. When this process continues, the mass of fluid in the bubble decreases over time and the steady separated region cannot be maintained. Therefore, to restore this deficit in mass, a certain amount of air needs to enter the bubble again. When this occurs, the bubble increases in size and this process will continue. Often, this behaviour is called *breathing* of the separation bubble and can be at the origin of the low-frequency movement of the separation shock. The large-scale shedding of vortices by the shear layer is often referred to as *flapping* (Clemens and Narayanaswamy, 2014). Grilli et al. (2012) support this theory as long as the SWTBLI is far from the incipient case. Finally, Pipponiau et al. (2009) conclude that small variations in the upstream boundary layer are unlikely to exhibit the low-frequency unsteadiness of the shock when the SWTBLI is far from the incipient case. This is supported by findings of Wu and Martín (2008) and Priebe and Martín (2011). Souverein et al. (2010) investigated incipient SWTBLI for a range of impinging SWTBLIs with differing Mach and Reynolds numbers and found that upstream boundary layer fluctuations indeed influence the separated flow but the effect weakened as the interaction size increased. This can be seen as a combination of both the amplifier and oscillator model, and it is frequently argued that both models are present in SWTBLIs but that one of the two dominates in the forcing of unsteadiness (Poggie et al., 2015).

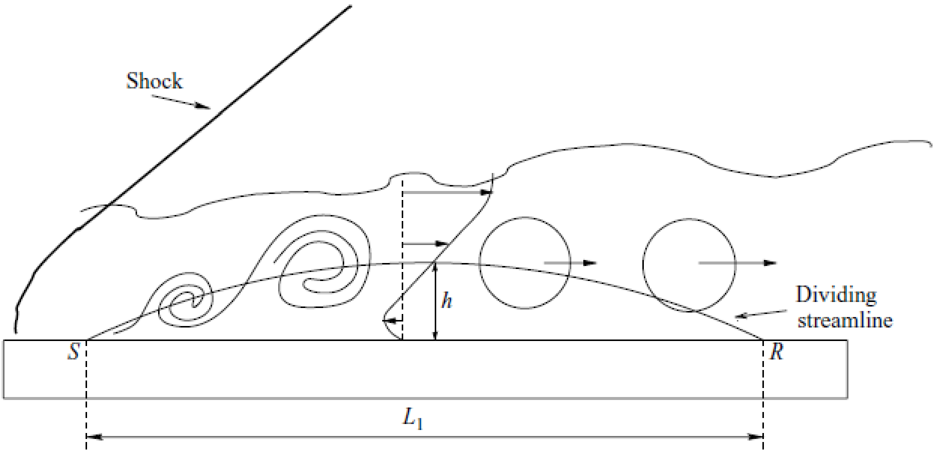

Figure 2.11: Visualisation of the mass-entrainment model with a well-defined separation bubble of length L_1 and the dividing streamline (i.e. mixing layer) (Pipponiau et al., 2009).

Another model by Pirozzoli and Grasso (2006) states that an acoustic feedback mechanism drives the separated flow unsteadiness. They examined DNS data for an impinging SWTBLI at Mach 2.25 on a flat plate. A shear layer between the separation bubble and the subsonic part of the separated boundary layer is generated at the average separation point of the separation shock. This creates spanwise coherent structures or eddies. They convect and grow in the streamwise direction and interact with the transmitted shock foot such that acoustic disturbances are generated. These propagate to the separation shock through the subsonic part of the boundary layer and induce an oscillatory motion. This behaviour is then sustained by an acoustic resonance mechanism originating from the separated region. It is argued, however, by Clemens and Narayanaswamy (2014) that it would mainly contribute to small-scale unsteadiness excited by high frequencies rather than large-scale fluctuations.

The advancements in numerical simulations of high-speed aerodynamics have led to an increase in research of LES and DNS while using global and/or local stability analysis. Nichols et al. (2017) mined an LES database for various impinging shock strengths using Dynamic Mode Decomposition (DMD) which showed the presence of two flow modes: one low-frequency mode associated with the breathing of the separation bubble and flapping of the reflection shock, and one high-frequency type depicting the upstream propagation of instability waves through the interaction zone. Flapping is used in a different context, but it represents the similar motion of the shedding of vortices in the shear layer of the separation bubble. The latter stability mode seems to agree with the acoustic feedback mechanism of Pirozzoli and Grasso (2006). Another LES simulation by Pasquariello et al. (2017) revealed three modes for a Mach 3 impinging SWTBLI: two low-frequency modes related to the breathing of the separation bubble and flapping of the reattachment line and one medium-frequency mode responsible for the corrugation of the reflection and reattachment shock wave. These modes are similar to those obtained by Nichols et al. (2017). Furthermore, the outcomes of Pasquariello et al. (2017) support the idea that Görtler-like vortices are a continuous forcing for the low-frequency unsteadiness in strong SWTBLI. Görtler vortices are pairs of counter-rotating vortices in concave boundary layer flow and are identified as a form of centrifugal instabilities (Saric, 1994). The finding of Görtler-like vortices is supported by, amongst others, Hu et al. (2022) and Fan et al. (2024). Zhuang et al. (2018) focussed its research on detecting the Görtler-like vortices for an oblique SWTBLI and succeeded by using ice-cluster-based planar laser scattering. They argue that the Görtler instability arises from the aerodynamic concave structure near the reattachment region.

To recapitulate, it has been reported by various studies that the SWTBLI low-frequency unsteadiness is generated by an upstream or downstream forcing mechanism. Researchers indicate that it could be due to the superstructures in the upstream boundary layer, and others due to centrifugal instability, acoustic feedback mechanism, or mass entrainment in the separated area. Some researchers argue that the mechanisms coexist and their dominance depends on the magnitude of the interaction. Considerable effort has been made to correlate these occurrences at different locations within the interaction, and it has not yet been proven to what extent certain mechanisms are dominant. While there is overall good agreement for weakly and well-separated SWTBLIs, the incipient case is still much under debate. There also remains debate about the ‘universality’ of the problem when the geometrical properties of the interaction change. Nevertheless, recent technological advancements (both experimental and numerical) allow researchers to obtain more conclusive results.

2.3. Flow Control of Shock Wave-Boundary Layer Interactions

This section discusses the general objective of flow control techniques for SWTBLIs in subsection 2.3.1 and the Shock Control Bump used in this research in subsection 2.3.2.

2.3.1. Objective of Flow Control

The phenomenon of SWTBLI occurs in various aeronautical applications such as transonic aerofoils, supersonic engine inlets, and the compressor blades of turbomachinery (Sabnis and Babinsky, 2023). The associated effects of flow separation and a significant increase in pressure across the shock wave can be detrimental to the aerodynamic performance. The effects can therefore be summarised in two types of drag: wave drag due to the strength of the shock system and frictional drag due to the thickening or flow separation of the boundary layer. Although most subsonic flow control techniques are employed as ’boundary layer improvement’ devices, control mechanisms in compressible aerodynamics have the additional possibility to act as ’shock wave improvement’ devices. Delery (1985) defined two major groups of control mechanisms depending on their location of utilisation. This can be upstream to improve the health of the incoming boundary layer or within the interaction region itself.

Its goal can either be obtained in an *active* or *passive* way. The difference is that active flow control requires an additional source of energy to add and/or subtract energy from the flow whereas this is not required for passive flow control (Jana and Kaushik, 2022). Control of the SWTBLI becomes even more challenging when considering the different flow regimes. Transonic aerodynamics has the extra challenge of buffeting, and hypersonic aerodynamics is often associated with significant (local) aerodynamic heating (Huang et al., 2020). Hence, each control mechanism has a specific purpose and it can be obtained in different ways.

An example of active flow control is the application of zero-net-mass jets. These are small orifices in which an alternating actuator can ingest or extract energy from the boundary layer through a set frequency. Vadillo et al. (2005) investigated this application for transonic aerofoil surfaces to improve aerodynamic performance and showed using Unsteady Reynolds-Averaged Navier-Stokes (URANS) simulations that these jets can modulate lift, drag and pitching moment. If used properly, it can also be used to suppress the unsteady effects of the SWTBLI (Glezer and Amitay, 2002). Another example is the use of flow suction and/or blowing using small orifices at the surface of the wall to improve the characteristics of the boundary layer. It does so by removing the low momentum and/or injecting high-velocity fluid in the boundary layer such that the velocity profile becomes fuller and more resistant to flow separation. The former effectively suppresses the boundary layer from flow retardation such that stronger shocks are needed to separate the flow. On the other hand, the latter is able to reduce the separation bubble size (Jana and Kaushik, 2022). There are several more active flow control techniques such as micro jets, air-jet vortex generators, and plasma jets (Jana and Kaushik, 2022).

2.3.2. The Shock Control Bump

Passive flow control techniques come in various forms such as micro vortex generators (Giepmann, 2016), porous cavities (Dores, 2024; Jana and Kaushik, 2022), and surface bumps. The surface bump, or Shock Control Bump (SCB), originates from the idea of ‘filling up’ the separation bubble of the SWBLI where there originally was a smooth surface (Bruce and Colliss, 2015). The SCBs are either two- or three-dimensional, and two examples of a three-dimensional SCB are given in Figure 2.12. This figure shows the wedge and rounded bump which have a width w, length l, height h, leading edge (LE), trailing edge (TE), and crest.

The original intent of the SCB, which can be traced back to the 1970s, was to improve the buffeting and drag-divergence Mach number characteristics of transonic aerofoil designs(Bruce and Colliss, 2015). This was done by placing a bump the size of the separation bubble at the impingement location of the incident shock wave (Bruce and Colliss, 2015). Nowadays, it has been shown that the idea can be extended to supersonic and hypersonic applications such as engine inlets. Depending on the geometry, the SCB can serve to improve the health of the boundary layer and/or reduce the strength of the shock system (Colliss et al., 2016). Since the SWTBLI is dependent on both boundary layer and shock wave properties, the aerodynamic performance of an SCB can vary quite extensively.

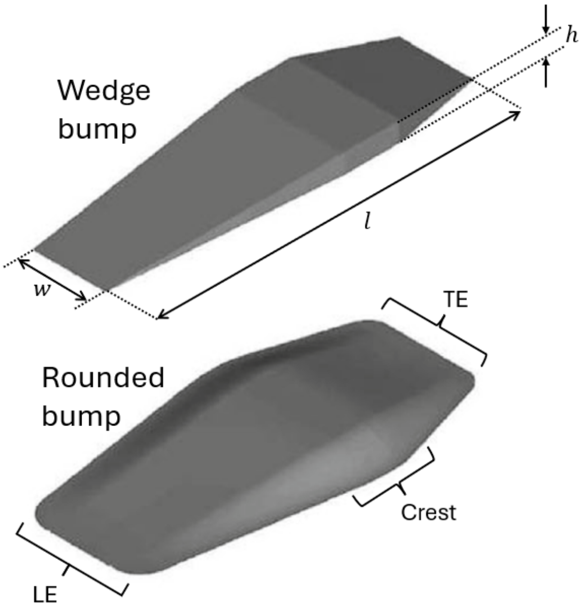

Figure 2.12: Two examples of the three-dimensional SCB (adapted from Bruce and Colliss (2015)). The lower figure includes the Leading Edge (LE), Trailing Edge (TE) and crest. The upper figure includes the width w, the length l and the height h.

Consider Figure 2.13 which shows the general flow structure of a normal SWBLI with and without a 2D-SCB on a flat surface. In Figure 2.13a, a general uncontrolled normal SWBLI is shown continued by a controlled SWBLI in Figure 2.13b. This case uses a streamwise symmetrical round SCB resulting in compression waves which coalesce in the normal shock wave. The coalescence into the normal shock for the controlled case takes place somewhat higher above the surface compared to the uncontrolled case. Therefore, the imposed adverse pressure gradient is more gradual such that the boundary layer flow retardation is lessened. The final figure, Figure 2.13c, shows a bump where the crest is positioned more downstream resulting in a lambda-shock structure with the front shock leg positioned at the leading edge and the rear shock leg near the bump crest. The triple point defines the point where the front shock, rear shock, and normal shock intersect. This shock structure is often called a λ-*shock* and has the advantage that the front shock leg is effectively anchored in the shock system (Bruce and Colliss, 2015). The pressure gradient due to this shock system near the surface is reduced relative to the uncontrolled case because two oblique shock waves replace the single normal shock wave and the compression waves. As a consequence, the boundary layer is subjected to a lower adverse pressure gradient compared to the normal shock and the total pressure recovery of the shock system is increased.

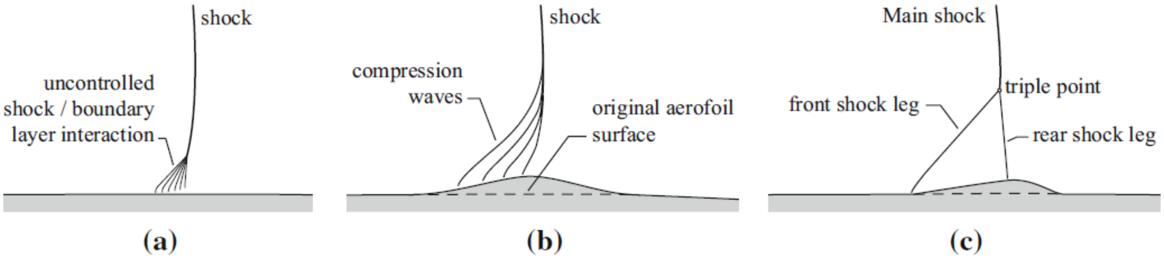

Figure 2.13: General flow structure of a normal SWTBLI for (a) an uncontrolled case, (b) a controlled case with a streamwise symmetrical bump, and (c) a controlled case with a more downstream crest in transonic flow (Ogawa et al., 2008).

Comparatively, the flow structure of a 3D-SCB is somewhat different from a 2D-SCB. This is because the flow is not only influenced by the streamwise length and smoothness of the bump but also its width and taper. To illustrate, see Figure 2.14 for a visualisation of the general flow structure of a three-dimensional rounded bump. The two-dimensional behaviour of the λ-shock structure is still present, but the structure reduces in size in the spanwise direction. Furthermore, a pair of counter-rotating streamwise vortices (A and B) are generated downstream of the bump close to the boundary layer edge. This adds momentum to the boundary layer flow and impedes flow separation. Hence, a variety of 3D-SCBs exist with their aerodynamic characteristics since the 3D-bump can both vary the shock and boundary layer properties.

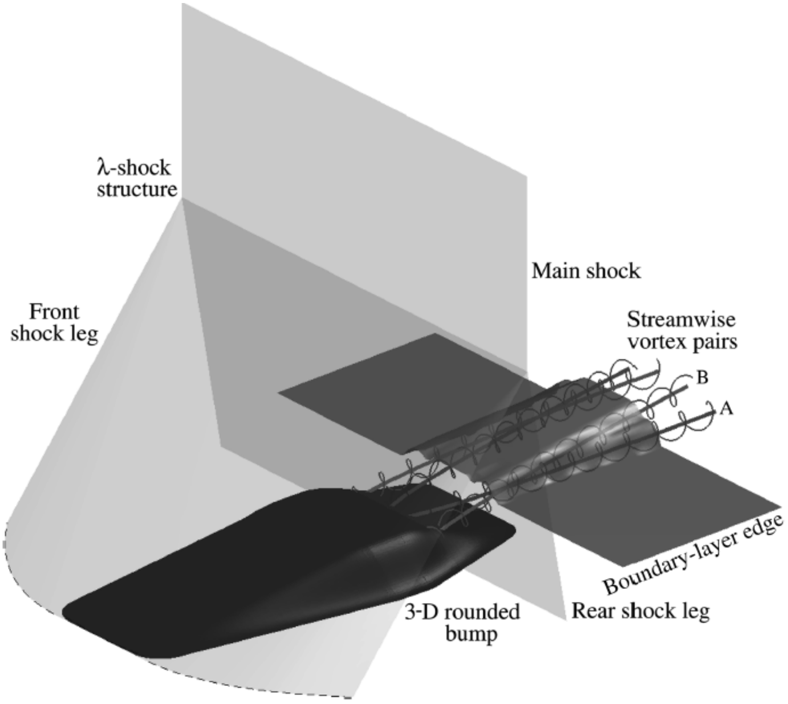

Figure 2.14: General flow structure of a three-dimensional SWTBLI with a rounded shock control bump at transonic conditions (Ogawa et al., 2008).

Because the general idea of the SCB is to ’fill up’ the separation bubble, the impingement location of the incident shock is important for its performance. Often, a distinction is made between the on-design and off-design location. Bruce and Colliss (2015) define on-design and off-design performance as the aerodynamic performance (lift and drag) of the bumps during the intended conditions (on-design) and deviating conditions (off-design). It can also be viewed as the extent to which the bump fills the generated separation bubble. For instance, Figure 2.13 shows a shock impingement location for an on-design case. Consider Figure 2.15 for the general flow structure of a normal SWBLI including the variance of impingement location. In Figure 2.15b, an on-design impingement location of the normal shock system is shown. Figure 2.15a shows the first off-design impingement location (upstream) where the rear λ-shock leg is on the ramp. This is followed by a re-expansion zone over the bump crest, due to the convex structure which re-accelerates the flow, with a secondary λ-shock structure near the tail of the bump. This secondary shock structure and supersonic region are often referred to as the *supersonic tongue* which increases the wave drag. For Figure 2.15c, the downstream impingement location can lead to unfavourable re-expansion at the crest LE which can lead to an additional λ-shock structure. This enhances boundary layer separation due to the stronger adverse pressure gradient and eventually a reduction in total pressure recovery (Ogawa et al., 2008).

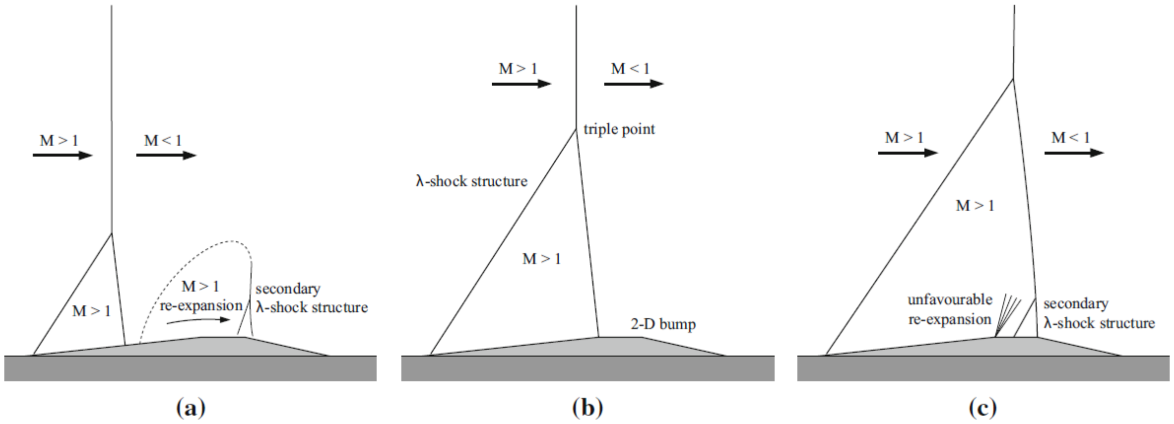

Figure 2.15: General flow structure of a 2D-SCB with varying impingement locations of the normal shock: a) upstream, b) on-design, and c) downstream impingement (Bruce and Colliss, 2015).

For the three-dimensional case, the flow structure becomes significantly more complex due to the spanwise variation of the geometry. Consider Figure 2.16 and 2.17 which show the flow structure for a variation in impingement location on a three-dimensional SCB in transonic conditions using Schlieren and oil flow visualisation, respectively. In Figure 2.16, the flow structure looks similar to the 2D-SCB whereas the oil flow shows a more complex structure. In Figure 2.17c, a local separation bubble is generated as the normal shock moves downstream. Please note that Schlieren images can be misleading since it seems that the flow structure is similar to the 2D bump case but it actually is different. This effect will be discussed in detail in section 2.4.

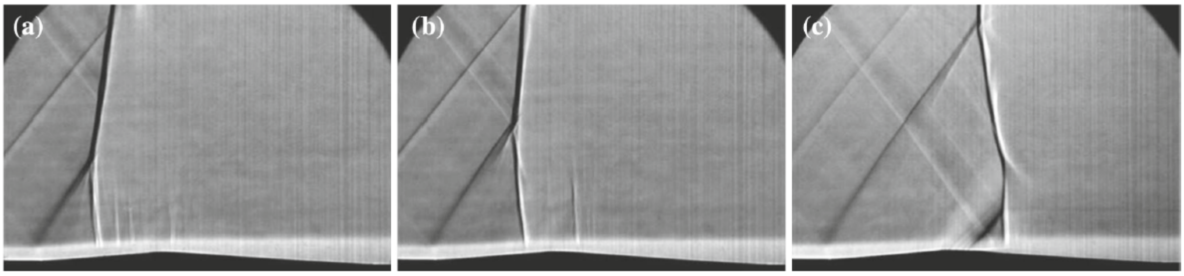

Figure 2.16: Schlieren visualisation of a normal SWTBLI with a 3D-SCB on a flat plate with varying impingement locations in transonic conditions: a) upstream, b) on design, and c) downstream impingement (Bruce and Colliss, 2015).

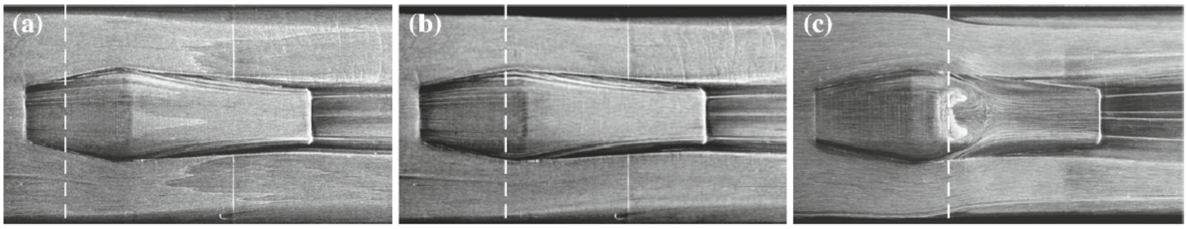

Figure 2.17: Corresponding oil flow visualisation of Figure 2.16: a) upstream, b) on design, and c) downstream impingement (Bruce and Colliss, 2015). The white dashed line indicates the location of the normal shock impingement.

Although performance is not of main importance for this research, it is helpful to understand the effect of the SCB shape on this aspect. Performance in this context depicts the ability of the SCB to reduce wave drag, viscous drag, and/or improve off-design performance. There have been various studies exploring this subject which include the variation of shape for normal SWTBLIs in transonic conditions (Colliss et al., 2012, 2014; Ogawa et al., 2008; Stanewsky et al., 2002), supersonic conditions (Ogawa and Babinsky, 2008), oblique SWTBLIs (Bulut et al., 2022, 2023, 2024; Missing et al., 2024), and more. In general, the performance of the SCB is a balance between the reduction of wave drag and viscous drag (Bruce and Colliss, 2015). Additionally, the bump height strongly depicts if the bump is used as a boundary layer control or shock system control device. This is because an increase in bump height tends to generate streamwise vortices as depicted in Figure 2.14 which would then be beneficial for the boundary layer while diminishing the positive consequences for the shock system. In this case, the bump would simply act as a vortex generator which is investigated by Bruce et al. (2014) and Colliss et al. (2016). For other applications such as transonic wings, the true potential of the bumps lies in situations where the Mach number is sufficiently high to generate a shock system. In other parts of flight, the uncontrolled case is preferred since the bump will only add viscous drag.

Another parameter of importance for bump design (or in general for control systems) is the *robustness*. Robustness depicts the ability of the bump to generate similar performance benefits between on- and off-design conditions (Bruce and Colliss, 2015). Studies often show that an on-design 2D-SCB outperforms the performance benefits compared to a 3D-SCB. On the other hand, 3D bumps show more favourable effects in off-design configurations while a 2D-SCB quickly leads to an increase in wave and/or viscous drag (Bruce and Colliss, 2015). An array of equally spaced 3D-SCB, however, shows similar performance benefits of a 2D-SCB since it will create a quasi-2D shock system (as seen in Figure 2.14) and results in similar performance benefits of a nominal 2D-SCB (Ogawa and Babinsky, 2008). The flow structure in this case will be more complex, so the shape of the SCB is important to retrieve the intended performance benefits.

One final aspect which has not yet been studied extensively is the effect of SCBs on SWTBLI unsteadiness. A recent study by Bulut et al. (2024) focussed on the assessment of an oblique SWTBLI at Mach 2 with 3D-SCBs in terms of understanding the interaction structure, unsteadiness, and effect impingement location. Through Schlieren, oil flow, and stereo-PIV, it was observed that the probability of flow separation on the bump ramp and crest in both on- and off-design situations was reduced compared to the uncontrolled case. In general, a deviation of the on-design impingement showed an increase in flow separation probability. This underlined the importance of the shock impingement location on the robustness of the SCB. In another study by the same authors (Bulut et al., 2023), different ramp angles were investigated using Schlieren, oil flow, and planar PIV. It showed that a lower ramp angle (i.e. the ramp becomes longer) resulted in lower interaction lengths and turbulence intensity levels. However, due to the shape of the 3D-SCB and the experimental techniques, no definite conclusion could be drawn about the alteration in unsteadiness when installing an SCB.

Missing et al. (2024) investigated a separation-bubble-shaped SCB to reduce separation and low-frequency unsteadiness of the interaction. The SCB is shown in Figure 2.18, and has the shape of the separation bubble as generated in the wind tunnel. Using Shadowgraphy, oil flow, and PIV, it was observed that the shock-induced separation was mostly eliminated. Furthermore, pre-multiplied PSDs of the separation shock showed that the observed Strouhal peak of $St_{L_{int}} \approx 0.03$ was reduced/eliminated in both the Shadowgraph and PIV measurements. The results of the PIV measurements are visualised in Figure 2.19 which show a streamwise contour plot of the pre-multiplied PSD in the extracted grid in terms of the interaction length-based and boundary layer-based Strouhal number. Also, flow separation probability distributions showed almost no flow reversal when the SCB was installed. This indicates that 2D/3D-SCBs have the ability to reduce low-frequency unsteadiness in oblique SWTBLIs.

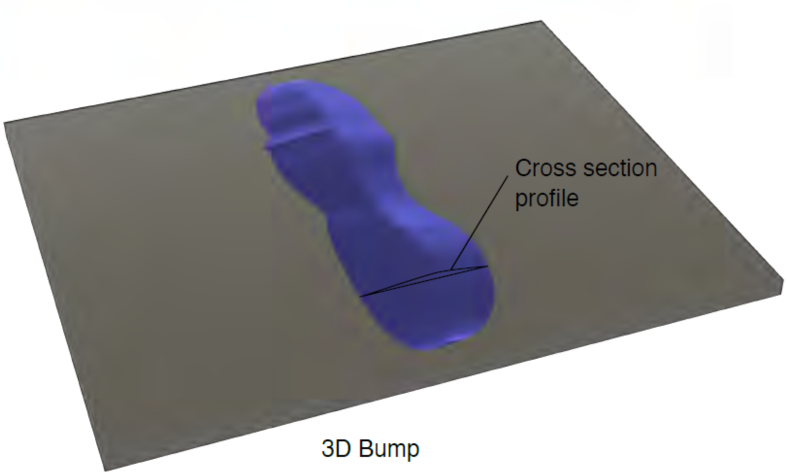

Figure 2.18: Visualisation of the separation-bubble-shaped SCB (Missing et al., 2024).

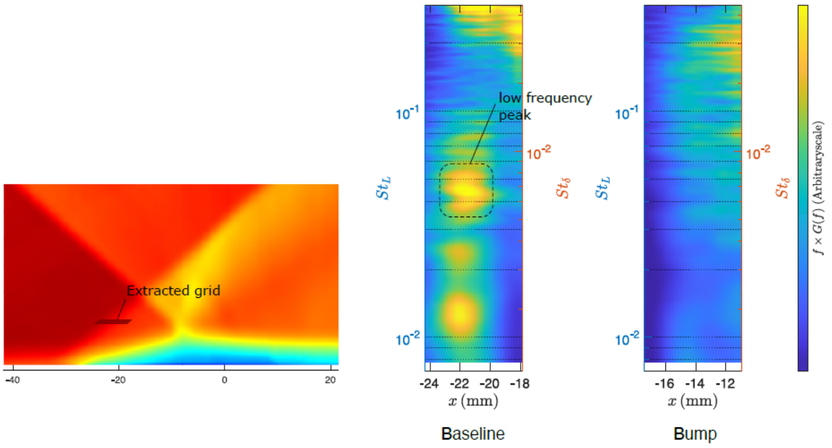

Figure 2.19: PIV visualisation (left) and pre-multiplied PSD (right) of the separation shock for an uncontrolled oblique SWTBLI (first PSD distribution) and installing the separation-bubble-shaped SCB(second PSD distribution). Results have been plotted using the uncontrolled interaction length and boundary layer-based Strouhal number in the streamwise direction. The PSDs were calculated using the data from the extracted skewed grid (Missing et al., 2024).

2.4. Experimental Techniques

In experimental aerodynamics, a range of techniques is available to obtain qualitative or quantitative information about the flow field. These techniques can generate data in terms of e.g. velocity or pressure. Two frequently used methods for investigating SWTBLIs are oil flow visualisation (subsection 2.4.1) and Schlieren (subsection 2.4.2). Both these methods will be utilised within this thesis.

2.4.1. Oil Flow Visualisation

Oil flow visualisation is a qualitative, intrusive method which can be used in a variety of flow regimes. This technique helps to give information about the status of the boundary layer, and it can indicate if the layer is attached, transitioning, or separating from the object. To explain the working principles of this technique, consider Figure 2.20 which shows a layer of oil (green) on a flat wall including the velocity profile in red. In the situation when the air velocity has a certain magnitude u_∞, a boundary layer will be generated and it will have a velocity U_0 at a distance h_0 from the wall. The oil layer is located in the region of the boundary layer flow where viscous forces dominate, i.e. the inner layer (White and Majdalani, 2022). The momentum balance at the oil-air interface then reduces to the balance between the viscous forces of the air and the oil such that $\tau_{oil} = \tau_{air}$ or $\mu_{oil}\frac{\partial u}{\partial y}|_{oil} = \mu_{air}\frac{\partial u}{\partial y}|_{air}$. Since the viscosity of air is smaller than the viscosity of the oil, the velocity gradient within the oil layer is much smaller than the gradient in the boundary layer. The velocity gradient within the layer can be determined by integrating the shear stress $\tau_w = \mu_{oil}\frac{\partial u}{\partial y}$ to obtain $U_0 = \tau_w h_0/\mu_{oil}$. As a result, the viscous forces of the air drive the viscous forces of the oil layer (D'Aguanno, 2023).

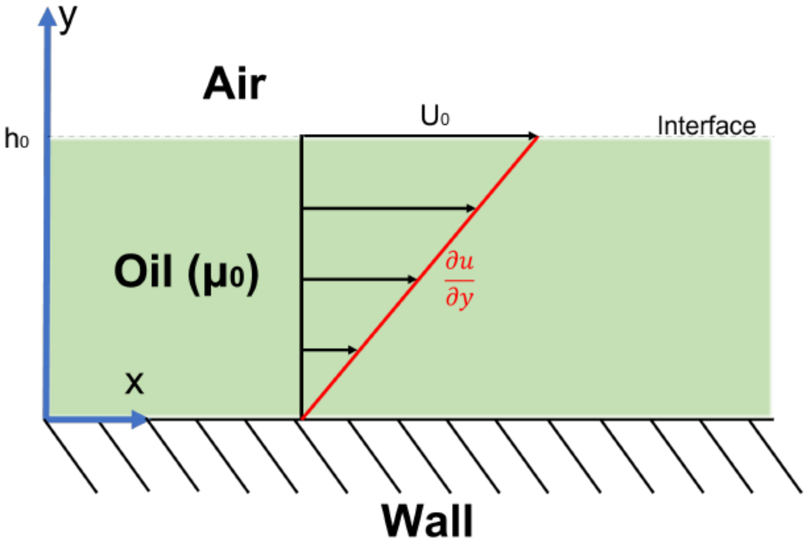

Figure 2.20: Visualisation of an oil layer and the velocity profile near the wall surface (D'Aguanno, 2023).

By this principle, attached and separated regions of the boundary layer can simply be identified. The attached flow regions show the smearing of the oil while separated flow regions show the accumulation of the oil. Furthermore, regions where flow re-attaches again show a depletion in oil. This reasoning only holds when the pressure gradients are sufficiently small with respect to the wall shear stress. When this is not the case (such as in flow separation) the oil flow technique cannot provide useful information. Further factors which play a role are the thickness of the oil layer on the object. Skin friction lines might not be visible when the layer is too thin, and excessive oil can accumulate and show a blur of friction lines. This is a trial-and-error process, and an application of this technique can be seen in Figure 2.17 in subsection 2.3.2.

A useful concept which can be applied using oil flow visualisation is critical point theory by Legendre (Babinsky and Harvey, 2011). This theory considers skin friction lines on an object (visualised by the oil) and examines the behaviour of these lines close to points where the skin friction vanishes. In this way, points can be identified as saddles, nodes, and foci, denoted by an S, N, and F, respectively. For instance, separation points within SWBLIs are a class of saddle points (S) whereas the recirculating flow within the separation bubble can be identified as a focus (F). Figure 2.21 shows an application of the critical point theory for a three-dimensional SWBLI duct flow including visualisation of the skin friction lines on the side walls. It can be seen that four foci are generated near the side walls, and two saddle points in the middle, S_1 and S_2, are created. Additionally, the separation and attachment lines, S and A respectively, are also shown.

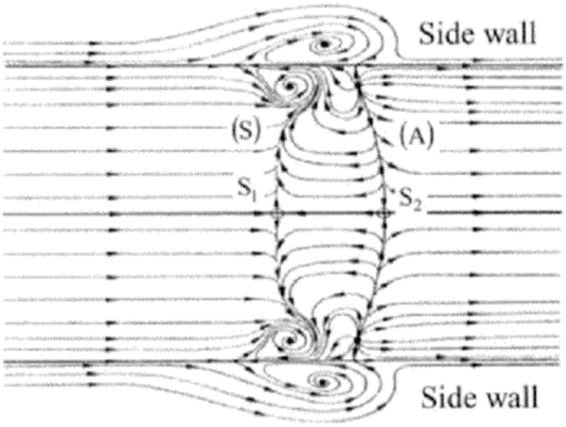

Figure 2.21: Visualisation of skin friction lines topology for a three-dimensional SWBLI duct flow including side walls using the critical point theory (Babinsky and Harvey, 2011).

2.4.2. Schlieren

The Schlieren technique, also known as the Toepler-Schlieren technique, is a non-intrusive, qualitative experimental technique. It uses the principle of refraction of light rays which travel through a medium based on the variation of density within this medium. Each medium has a certain refractive index n and varies depending on the density distribution within the considered medium. The variation of the refractive index and density for a gas is described by the Gladstone-Dale equation given in Equation 2.5 (Tropea et al., 2007)

$$n = K\rho + 1. \tag{2.5}$$

In this equation, K represents the Gladstone-Dale constant which depends on the medium and (to some extent) the wavelength of light. For air, the Gladstone-Dale constant $K_{air} = 2.26 \cdot 10^{-4}$ [m^3/kg]. When the air is considered an ideal gas, the variation of density is directly proportional to the Mach number such that the obtained flow results are a direct measure of the Mach number or velocity (Tropea et al., 2007). These variations are captured using an optical setup which is why it is often referred to as an optical flow visualisation technique.

The magnitude of the light ray deflection can be quantified using Ray's equation (Equation 2.6). In this equation, s is the path of the light ray and $\bar{x} = \{x, y, z\}$. Ray's equation depicts that a light ray travelling along a path ds will always deflect in the direction of increasing refractive index (∇n). Since the refractive index is linearly proportional to the density, the light rays will deflect in the direction of increasing density. This principle is useful as the deflection of these rays creates darker and brighter regions which give a direct indication of position and magnitude of the local variation in density. For this research, it can indicate shock and expansion waves.

$$\frac{\partial}{\partial s}\left(\frac{\partial \bar{x}}{\partial s}\right) = \nabla n. \tag{2.6}$$

The deflection of light rays can be visualised using Figure 2.22. When the light rays with intensity I_0 intersect a shock wave, they will deflect in the direction of increasing density. In the recorder plane, the local intensity of light is obtained as a combination of a dark and bright spot. The test object creates a shadow region, and undeflected rays are recorded with the undisturbed intensity. Therefore, shock waves will appear as dark/bright spots in the recorded image. In a more mathematical formulation, the second derivative of the density variation ($\nabla^2\rho$) is obtained. Figure 2.22 decribes the working principle of Shadowgraphy.

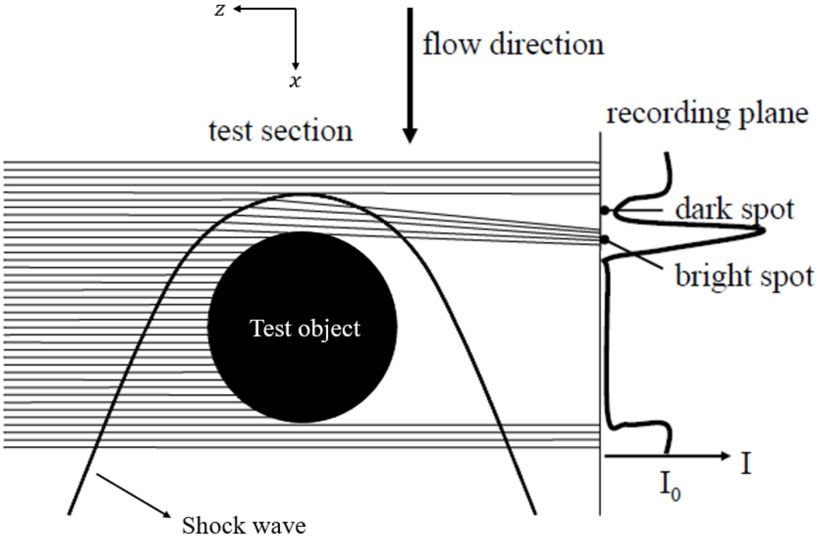

Figure 2.22: Sketch of the deflection of light rays in the presence of a shock wave including its effect on the intensity detection on the recorder plane.

The Schlieren technique uses a *knife-edge* or *Schlieren head* to ’filter’ the deflected light rays. In this way, the first derivative of the density variation is obtained ($\nabla\rho$), and the deflection of the rays is recorded as a bright or dark region only. The edge can be positioned horizontally or vertically, and an example of a vertical knife-edge is given in Figure 2.23. There, an example of an oblique SWTBLI Schlieren image, annotated regions (1-3), vertical knife-edge, light ray deflection angle, and position of the light rays are given. A deflection in the streamwise direction is considered positive. Region 1 is the free-stream flow and has a deflection angle $\epsilon_x = 0$ with an intensity I_0. For a region with increasing density (the shock wave in region 2), the rays deflect to the right ($\epsilon_x > 0$) creating a darker region. The opposite is true for region 3 for the expansion fan where the density decreases ($\epsilon_x < 0$) and the region becomes brighter. This shows the ’filtering’ principle of the knife edge.

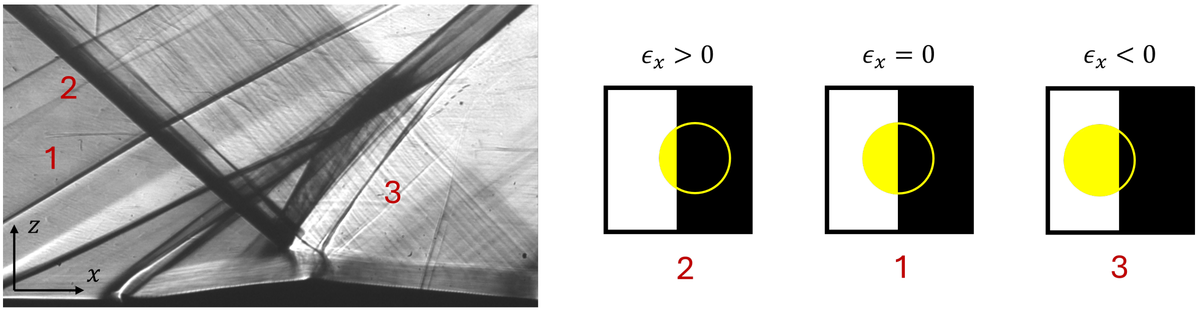

Figure 2.23: Vertical knife-edge configuration and the effect of light ray deflection on the ’filtering’ of light deflection.

A Z-type Schlieren configuration was utilised in this research which is illustrated in Figure 2.24. This figure shows the various numbered components, the wind tunnel (green), the light rays (dotted blue), and the test section. The setup starts with an incoherent light source (1) which is collimated and converged using two lenses (2-3). This concentrated light then goes through a pinhole (4) which controls the intensity of the light beam through the test section. The position of this pinhole must be in the focal point of the converging lens (3) and parabolic mirror (6). This is because a deviation from this position will block light from going through the section, and the light intensity through the test section will be harder to control. After this, the light is reflected using a normal (5) and a parabolic (6) mirror such that the beam is parallel to the window test section of the wind tunnel. When this light has traversed the section and is deflected due to density gradients, it is reflected once more through a parabolic (7) and normal (8) mirror to the knife edge (9). The knife edge is also positioned in the focal point to obtain the correct variance of the density gradients. The remaining light beams travel to a final converging lens (10) to focus the image on the camera sensor (11). The advantages of the Z-type Schlieren method are that an incoherent white light source can be used, and the setup is relatively simple. Furthermore, the object will be in focus (which is not the case with e.g. Shadowgraphy), and direct qualitative information can be obtained from the flow field. On the other hand, the images could experience a certain level of white noise originating from dust, contaminated lenses, and the digital camera (Nazari et al., 2020). Also, the deflection of light rays is integrated over the spanwise section of the wind tunnel. This means that both two- and three-dimensional effects are observed. Finally, the orientation of the knife-edge can alter the observation of compression and expansion regions in the test section.

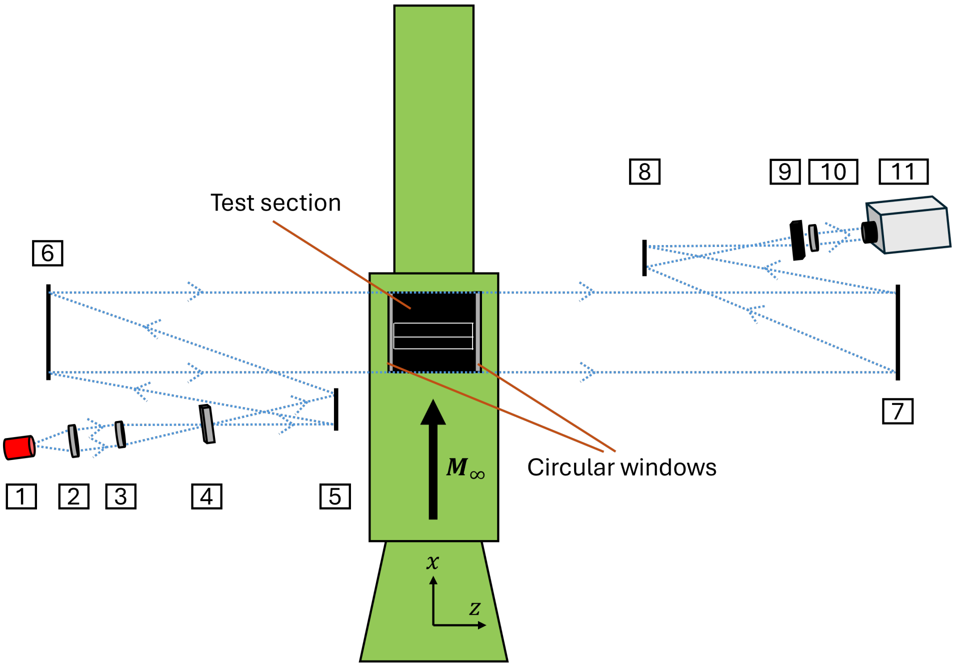

Figure 2.24: Schematic of the Z-type Schlieren setup used during experiments: 1) The LED light, 2) Collimating lens, 3) First converging lens, 4) Pinhole, 5) First normal mirror, 6) First parabolic mirror, 7) Second parabolic mirror, 8) Second normal mirror, 9) Knife edge, 10) Second converging lens, and 11) Camera.

3

Methodology

This chapter outlines the essential methods required to answer the research objectives. First, the wind tunnel setup will be discussed in section 3.1. Second, the design of the shock control bumps and experimental techniques will be discussed in section 3.2 and section 3.3, respectively. Finally, the data processing techniques will be discussed in section 3.4.

3.1. Wind Tunnel Setup

The research will be conducted in the supersonic wind tunnel of the TU Delft. The characteristics of the wind tunnel are discussed in subsection 3.1.1, and any external vibrations will be discussed in subsection 3.1.2.

3.1.1. General Wind Tunnel Characteristics

The wind tunnel used for the experimental investigation is the ST-15 supersonic wind tunnel at the High Speed Laboratory (HSL) at Delft University of Technology. This is a blowdown-type wind tunnel, and a schematic visualisation is given in Figure 3.1. An isometric view of the ST-15 is given in Figure 3.2.

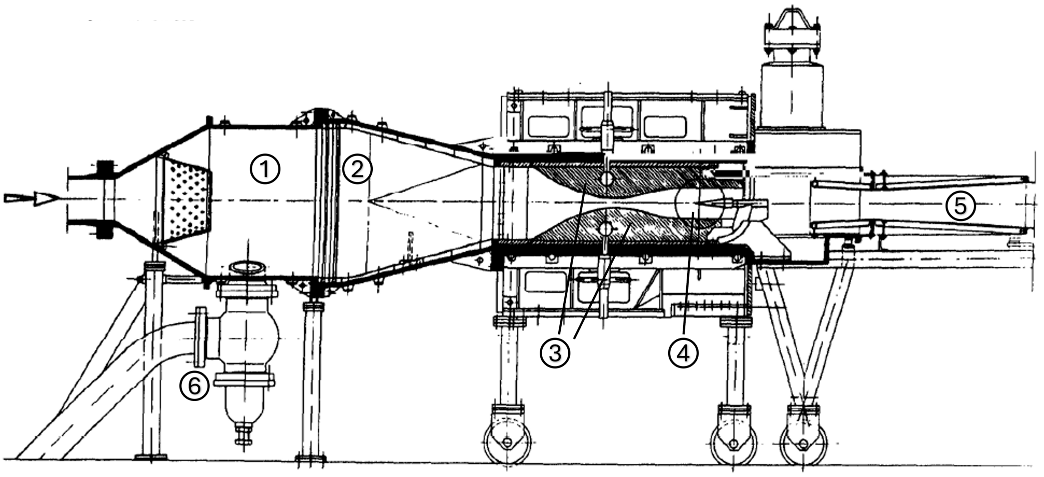

Figure 3.1: Schematic of the ST-15 supersonic wind tunnel: 1) Settling chamber, 2) Turbulence screens, 3) Mach blocks, 4) Test section, 5) Adjustable diffuser, and 6) Safety valve (adapted from Kingsbury (1990)).

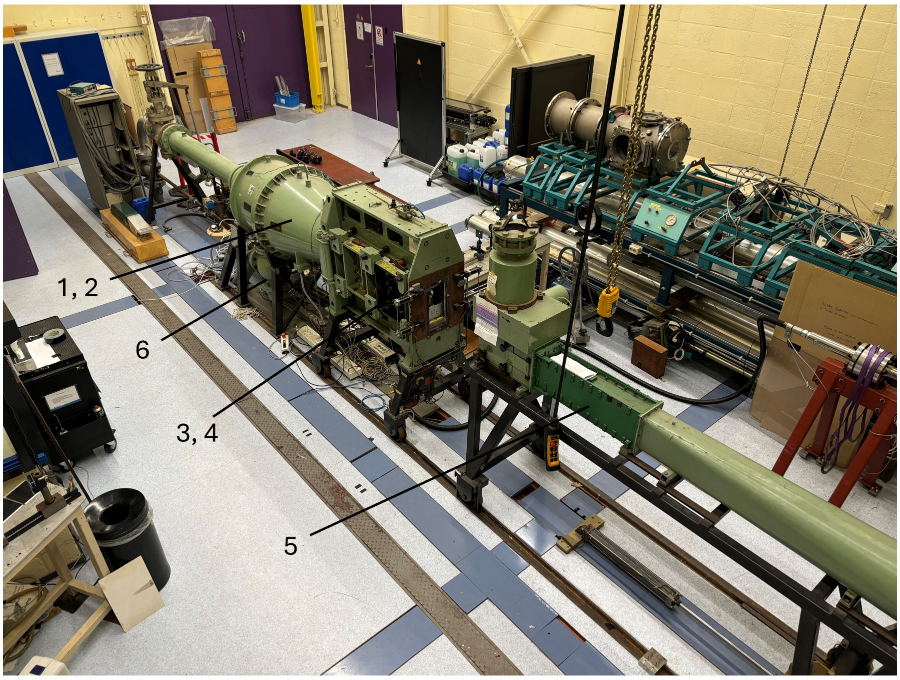

Figure 3.2: Isometric view of the ST-15. Components are indicates as given in Figure 3.1.

The ST-15 uses a pressurised vessel which can store up to 300 m^3 of dry air at a pressure of 40 bars. Considering Figure 3.1, the air then traverses to the settling chamber (1), a set of screens (2), and the Mach blocks (3) near the test section (4). Mach numbers of 1.5, 2.0, 2.5, and 3.0 can be obtained by installing the Mach block in (3). Furthermore, pressures can be initialised in the settling chamber to a maximum of $p_0 = 15$ (Kingsbury, 1990). The pressure and temperature in the settling chamber are considered as total flow conditions. The test section has dimensions of 150 x 150 x 250 millimetres consisting of a plate, two clamps, and a shock generator. The section is visualised in Figure 3.3, and it can be accessed optically by two circular windows ($d = 250$ [mm]) on each side of the section. A diffuser (5) downstream of the test section allows the wind tunnel to operate at lower total pressure ratios such that total pressure losses are minimised. Finally, the wind tunnel has a maximum run time of around 20 minutes before the vessel needs to be pressurised again (Kingsbury, 1990).

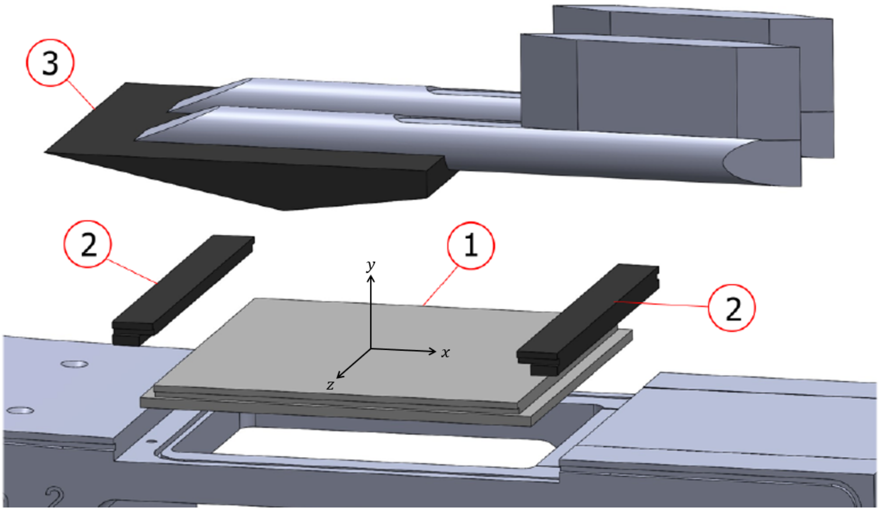

Figure 3.3: CAD model of the ST-15 test section including 1) the panel model, 2) the set of clamps, and 3) the shock generator with its support system (Allerhand, 2020). The model includes the axis system used in this research.

For this investigation, a Mach block of 2.0 was used giving a total pressure initialisation range of $2.0 \leq p_0 \leq 4.8$ bars. Giepmann (2016) investigated boundary layer properties of the same facility at a Mach number of 2.0 and a total pressure of $p_0 = 3.0$ bar. These properties are used for this thesis and are tabulated in Table 3.1.

Table 3.1: Undisturbed boundary layer properties in the ST-15 at $M_\infty = 2.0, p_0 = 3$ bar (Giepmann, 2016).

Parameter	Quantity	Unit	Parameter	Quantity	Unit
M_∞	2.0	[-]	θ_i^*	0.52	[mm]
u_∞	520	[m/s]	H_i	1.23	[-]
p_0	3.0	[bar]	u_τ	20.8	[m/s]
T_0	290	[K]	$c_{f,0}$	$1.9 \cdot 10^{-3}$	[-]
δ_0	5.2	[mm]	Re	$42.2 \cdot 10^6$	[1/m]
δ_i^*	0.63	[mm]	$Re_{\theta_i^*}$	$21.8 \cdot 10^3$	[-]

3.1.2. Wind Tunnel Induced Vibrations

It is vital to be aware of external vibrations which could influence the SWTBLI because frequency analysis is used for this thesis. Investigations conducted in the same wind tunnel by Radaelli (2024), Allerhand (2020) and Aditya (2022) on fluttering panels revealed that pressure waves generated within the wind tunnel propagate towards the cavity beneath the test section. These pressure waves induce spurious frequencies which can resonate with the wind tunnel plate. Consequently, the presence of an open cavity and/or the flexibility of the panel may contribute to unintended vibrations in the test section.

Allerhand (2020) performed accelerometer measurements of the Mach blocks and test section and argued that the shock generator, temperature of the wind tunnel, and panel flexibility influenced the observed dominant frequencies. Especially, a frequency of around 576 Hz was found in both the flow and panel measurements. Aditya (2022) confirmed this behaviour through simultaneous Schlieren and accelerometer measurements and concluded that this excitation originates from the lower Mach block at around 614-618 Hz. For the SWTBLI case with a rigid plate, however, this frequency was only observed in the displacement measurements of the plate and not in the velocity measurements. He argued that this frequency response was inevitable in the ST-15 and should be considered for all fluid-structure interaction investigations. This does not exclude the possibility for this displacement effect to influence the SWTBLI on the rigid plate, and no efforts have been made to confirm this possibility.

An attempt to quantify resonance motion due to pressure wave entering the cavity was performed by Radaelli (2024). He investigated frequency responses through high-speed Schlieren measurements for an open, ventilated, and closed cavity and found that pressure waves existed in the cavity which seemed to exhibit resonance with the plates. More importantly, he observed a decrease in energetic content in the dominant frequency of 750 Hz for a closed cavity. Hence, based on these observations, the cavity was closed using the same cavity closure method proposed by Radaelli (2024). Therefore the possibility is excluded as much as possible for the external vibrations to influence the dynamics of the flow. Figure 3.4 illustrates the closure, achieved by securing an aluminium plate with nine bolts to seal the ventilation holes. Additionally, six bolts ensure that the aluminium plate is firmly fastened to the wind tunnel test section.

Figure 3.4: Picture of the cavity close using an aluminium plate in the ST-15 wind tunnel.

3.2. Shock Control Bump Design

To achieve the objectives of this thesis, various shock control bumps were developed. First, a baseline bump will be designed in subsection 3.2.1 after which the spanwise length will be considered in subsection 3.2.2. This is part of experimental campaign A. The section is concluded by the design considerations for the alteration in SCB geometry in subsection 3.2.3 for experimental campaign B.

3.2.1. Baseline Bump Design

The objective of this thesis is to observe possible changes in the unsteady behaviour of the SWTBLI while utilising a form of the SCB. Even though there are various approaches to defining the shape of the bump, the emphasis will be on the fundamental understanding of these possible changes. One possibility is to use the inviscid flow model representation of the SWTBLI as discussed in subsection 2.1.3. This model is repeated here for convenience (Figure 3.5).

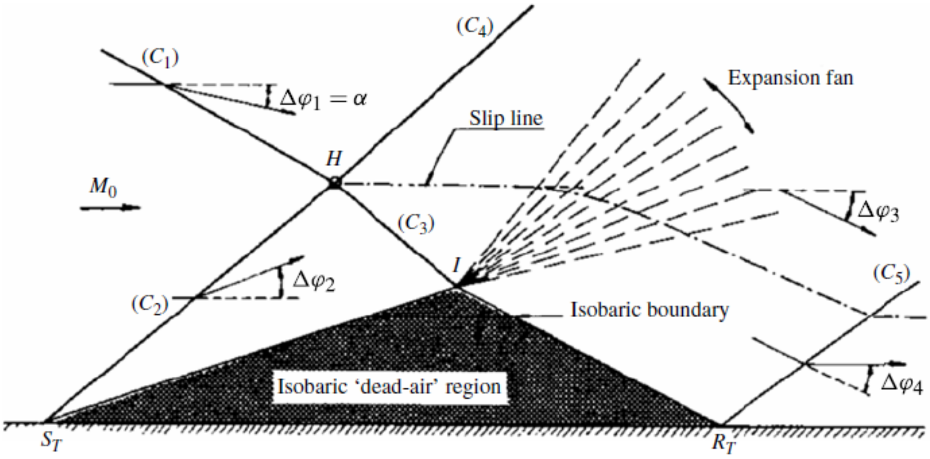

Figure 3.5: Inviscid flow model representation of an oblique shock wave-boundary layer interaction (Souverein et al., 2013).

Using the inviscid model, the downstream geometrical properties of the isobaric boundary (after point I) do not alter the pressure rise associated with the separation region. This offers a starting point for the SCB design since it allows for isolating bump geometry changes and the effect on the unsteadiness. The general SCB shape for this thesis will have the same shape as the isobaric region to 'fill up' the separation bubble. Three main parameters define the bump design:

- The initial flow deflection angle $\Delta\phi_2$ in degrees which is defined by the strength of the separation shock (C_2). For the bump, this will be referred to as the ramp angle θ_r;
- The final flow deflection angle $\Delta\phi_4$ in degrees which is defined by the flow deflection after the expansion fan. This will be referred to as the tail angle θ_t; and
- The height h between the wall and point I which represents the distance between the wall and the sonic line of the boundary layer.

With these parameters in mind, a baseline SCB geometry can be made which attempts to fill the separation bubble based on its equivalent inviscid representation. The parameters will be calculated using planar Particle Image Velocimetry (PIV) data of an uncontrolled oblique SWTBLI at $M_\infty = 2.0, p_0 = 3$ bar and $\phi_{SG} = 12°$ (Bulut et al., 2024) which is plotted in Figure 3.6.

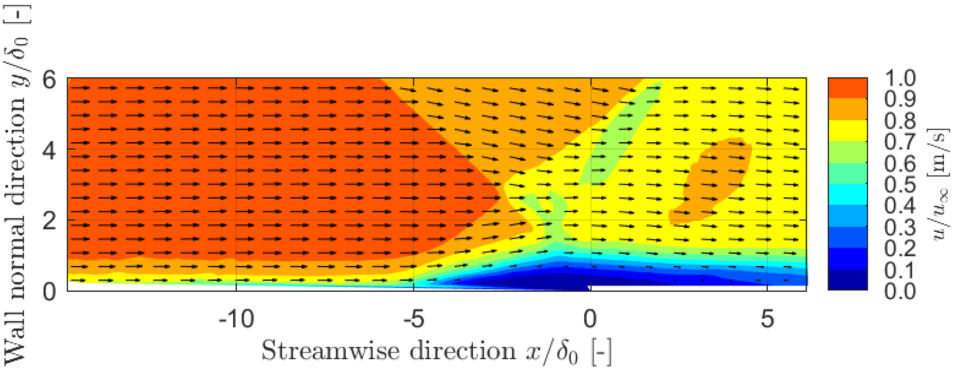

Figure 3.6: Mean streamwise velocity contour plot including direction of the flow for a Mach 2, $p_0 = 3$ bar, and $\phi = 12°$ uncontrolled oblique SWTBLI (Bulut et al., 2024).

Two boxes were defined in the region after the separation shock and the expansion fan to compute the ramp and tail angles for the baseline bump, respectively. Within these boxes, which can be seen in Figure 3.7, the angle between the individual u-, and v-velocity component was calculated and averaged. This resulted in $\Delta\phi_2 = 9.13°$ and $\Delta\phi_4 = -5.51°$, and the standard deviations for the ramp and tail were $\sigma_{\theta_r} = 0.65$ and $\sigma_{\theta_t} = 0.29$, respectively. Based on this, the baseline ramp and tail angles were determined as $\theta_r = 9.0°$ and $\theta_t = 5.5°$, correspondingly. The height was calculated using $L_{int} = 7\delta_0$ (Bulut et al., 2024) and $\beta_{\phi_{SG}} = 41.5°$ (Anderson, 2017) such that $h = 4.63$ mm. Note that the height of the bump is comparable to the turbulent boundary layer thickness $\delta_0 = 5.2$ mm. Literature states that SCBs with heights similar to the upstream boundary layer generate more favourable improvements compared to deviating heights (Bruce and Colliss, 2015). Here, 'favourable' implies that it decreases the strength of the shock system and/or decreases the downstream boundary layer thickness compared to an uncontrolled case. The baseline SCB is plotted in Figure 3.7. Lines to represent the incident and separation shock wave are included in this figure as well. When comparing the inviscid flow model in Figure 3.5 and the baseline SCB, similarities can be seen in the form of the angles of the isobaric region and the impingement of the incident shock on the bump crest.

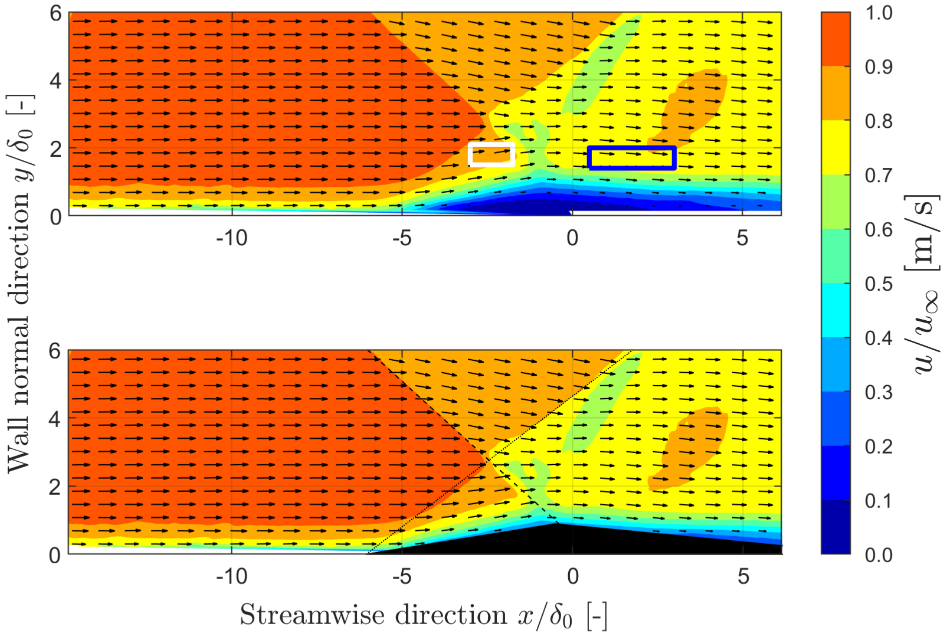

Figure 3.7: Mean streamwise velocity contour plot including direction of the flow for a Mach 2, $p_0 = 3$ bar, and $\phi = 12^\circ$ uncontrolled oblique SWTBLI (Bulut et al., 2024). The upper figure shows the white and blue boxes for $\Delta\phi_2$ and $\Delta\phi_4$, respectively. The lower figure shows the implementation of the baseline bump design.

3.2.2. Spanwise Design of the Shock Control Bumps

An important aspect of high-speed wind tunnel testing is the generation of *corner effects*. This is because these effects influence the interaction at the centre of the wind tunnel and generate complex, three-dimensional interactions in the corners. Corner effects occur in situations where flow traverses close to two perpendicular walls. When a shock is introduced, it can generate premature flow separation due to the superposition of two boundary layers (Sabnis and Babinsky, 2023). Since the flow momentum in these corners is lower compared to the centre section, the boundary layer is more sensitive to adverse pressure gradients and the flow can separate prematurely (Babinsky et al., 2013). The case of an oblique SWTBLI in a rectangular duct is considered in detail. This situation is visualised in Figure 3.8a and shows an oblique SWTBLI with corner effects for a single corner. As shown, a corner shock wave is generated because of the premature flow separation and it creates a region of corner separation. This interacts with the incident shock wave which can cause flow separation continuously downstream of the interaction.

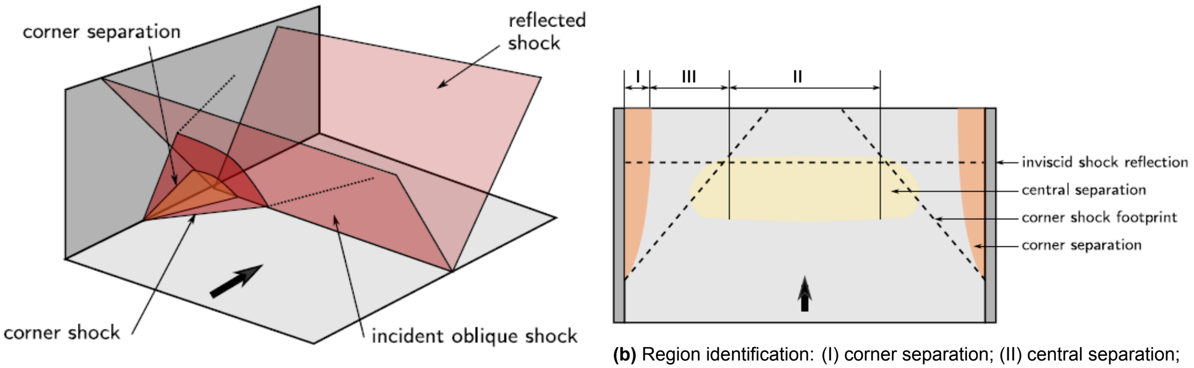

(a) General simplified flow field organisation.

(b) Region identification: (I) corner separation; (II) central separation; (III) intermediate region.

Figure 3.8: Schematic visualisation of corner effects in oblique SWTBLIs in a duct (Sabnis and Babinsky, 2023).

There are various factors which influence the magnitude of the corner effects, but the main parameters include the upstream Mach number, boundary layer properties, and the strength of the incident shock wave (Sabnis and Babinsky, 2023). Figure 3.8b shows a sketch of the flow field organisation on the lower wall of a duct flow with corner effects. Here, three regions are identified: (I) corner separation, (II) central separation, and (III) an intermediate region. In the first region, the corner flow originates the furthest upstream, and in the second region, the interaction is frequently almost two-dimensional. The third intermediate region is a region where the pressure waves emanating from the corner spread the pressure rise through the tunnel such that the flow remains attached (Sabnis and Babinsky, 2023). The extent of the centred-separation region and the influence of the corner effects have been investigated by Wang et al. (2015) and Xiang and Babinsky (2019). It was found that the separation behaviour in region (II) is mostly influenced by the imposed adverse pressure gradient of the corners. To illustrate this, Figure 3.9 shows a schematic of two interactions with different positions of the corner shocks and the effect on the centred interaction. It includes a sketch of the interaction at the duct centreline and an oil flow visualisation. The general trend is that the spanwise and streamwise extent of the centred interaction reduces as the corner effects occur further upstream (Xiang and Babinsky, 2019).

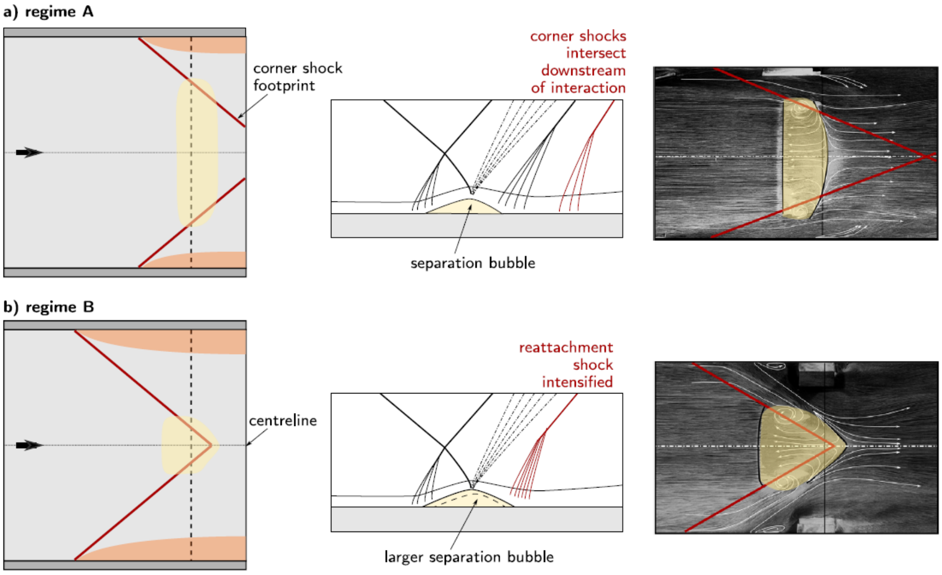

Figure 3.9: Schematic of the overall flow field organisation for a variation in corner effect position and the oblique SWTBLI in a duct. It includes a sketch for a downstream (regime A) and upstream (regime B) corner effect, a sketch at the duct centreline, and an oil flow visualisation (Sabnis and Babinsky, 2023).

Considering this effect in oblique SWTBLIs for duct flows, it is very important to consider the spanwise extent of the nominally two-dimensional interaction, i.e. region (II). Furthermore, the flow structure will be affected significantly while utilising SCBs. Hence, it is necessary to investigate different spanwise shapes of the baseline bump to see which SCB generates a flow structure with the most two-dimensional behaviour. For this, three bumps have been designed based on oil flow visualisation of an uncontrolled oblique SWTBLI in Figure 3.10.

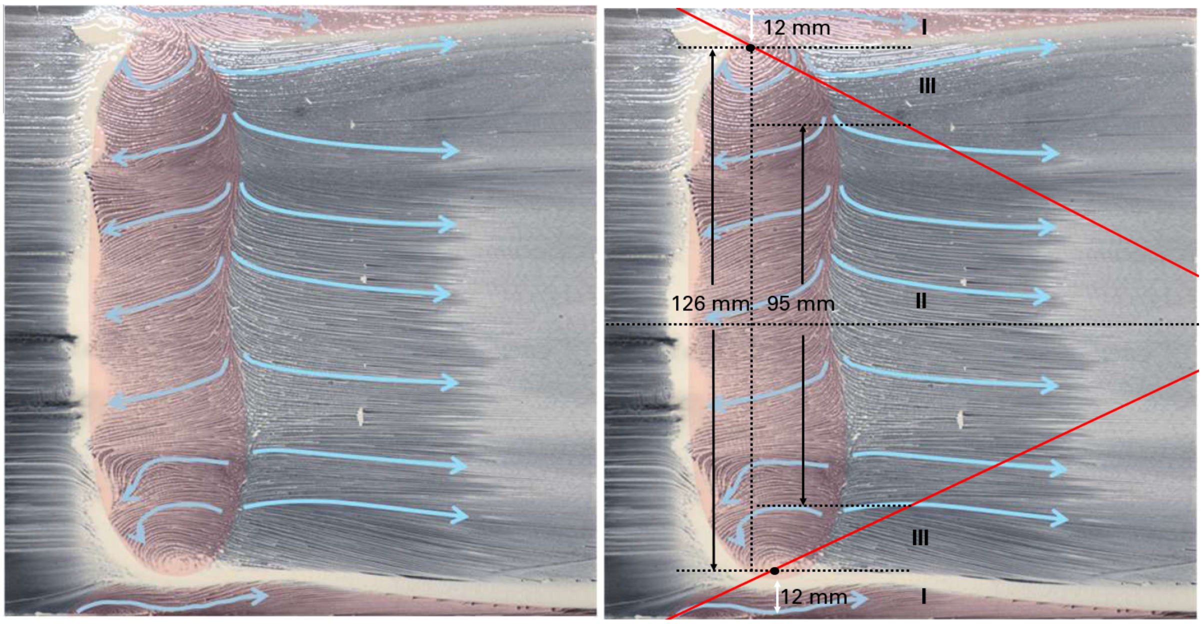

(a)

(b)

Figure 3.10: Oil flow visualisation of an uncontrolled oblique SWTBLI at $M_\infty = 2.0, p_0 = 2.5$ [bar] and $\phi_{SG} = 12°$ for a) the uncontrolled interaction (Radaelli, 2024) and b) the same interaction including annotations.

Figure 3.10a shows the oil flow visualisation at $M_\infty = 2.0, p_0 = 2.5$ bar and $\phi_{SG} = 12°$ where blue arrows indicate the direction of streamlines and red depicts regions of flow separation. This figure resembles the interaction sketched in Figure 2.21 with focal points near the corners of the duct and saddle points/lines along the separation/reattachment shock wave. Figure 3.10b shows the same interaction with dimensions of the interaction. By visual inspection, the centred interaction (region (II)) has a spanwise length of 95 mm and the corner separation (region (I)) is around 12 mm. The intermediate region (III) is around 15.5 mm on both sides. Based on this, two bumps with spanwise lengths of 150 and 95 mm will be investigated. These are referred to as the *baseline* and *short* bumps, respectively.

The design of the third bump originates from the possibility of vortex generation at the edges of the short bump. One can intuitively deduce that a dissimilarity in pressure will be generated when flow traverses over and sideways of the bump. This might introduce vortical structures which will affect the Schlieren images and therefore the quantification of unsteadiness by the edge-detection algorithm or spectral analysis. Thus, a third *smooth* bump will be designed based on the upstream curvature of the separation bubble in region (III). Its geometrical specifications are given in Figure 3.13. As a result, the bumps shown in Figure 3.11 were designed using AutoCAD2025. These were manufactured using the Bambulab X1E Series 3D printer, and the bumps were printed with black Polylactic Acid (PLA) filament. Due to the rapid prototyping technique, the bumps were sanded and installed on the wind tunnel test plates using double-sided tape. Finally, the geometrical definition of the bumps is given in Figure 3.12, and their specifications are tabulated in Table 3.2.

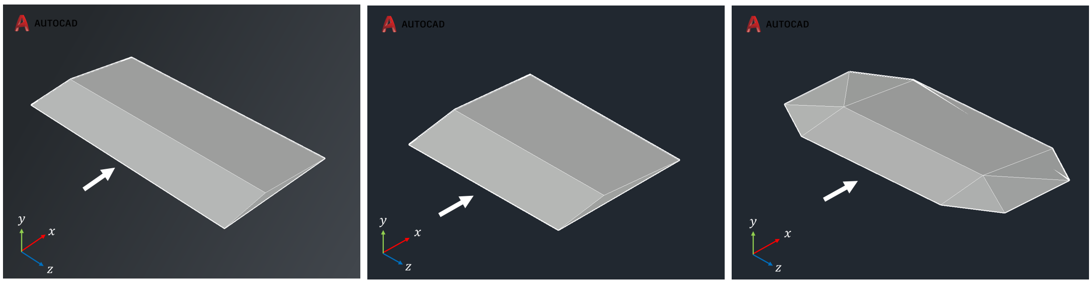

(a)

(b)

(c)

Figure 3.11: AutoCAD models of the a) baseline, b) short, and c) smooth bump. White arrows indicate the direction of flow.

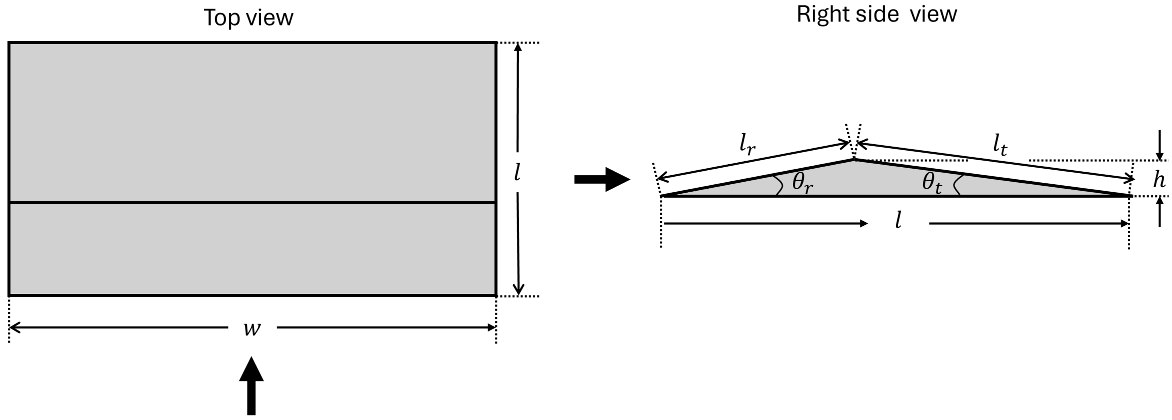

Figure 3.12: Geometrical definitions of the general shock control bump. Black arrows indicate the direction of flow.

Table 3.2: Geometrical specifications of the baseline, short, and smooth SCB.

Bump design	w [mm]	l [mm]	θ_r [degrees]	θ_t [degrees]	h [mm]	l_r [mm]	l_t [mm]
Baseline	150	77.4	9.0	5.5	4.63	29.6	48.3
Short	95	77.4	9.0	5.5	4.63	29.6	48.3
Smooth	150	77.4	9.0	5.5	4.63	29.6	48.3

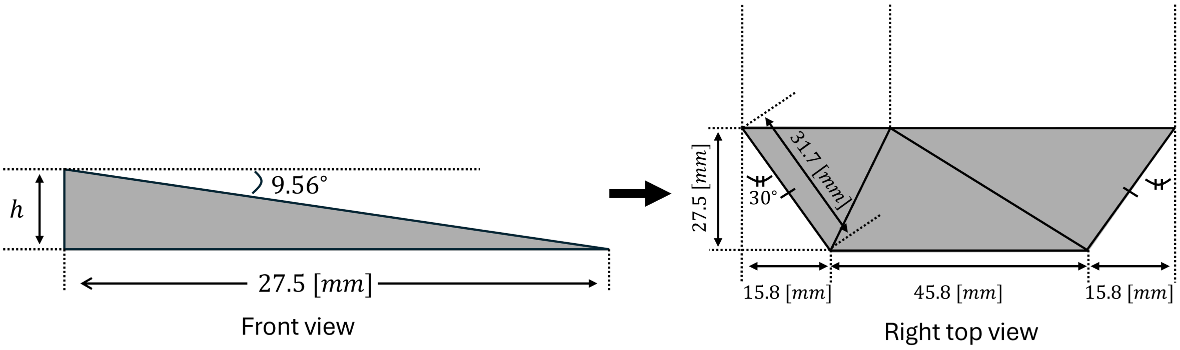

Figure 3.13: Specifications of geometrical properties of the smooth bump tapered edges based on the curvature of the separation bubble in region (III). The black arrow indicates the direction of the flow.

3.2.3. Variation in Shock Control Bump Ramp and Tail

When the three bumps were tested and assessed based on the Schlieren and oil flow visualisations, a decision was made for one of the three bump designs for campaign B. The objective, as discussed in chapter 1, is to assess the alteration in unsteadiness of an oblique SWTBLI using 2D bumps on a fundamental level, so the bump with the most two-dimensional interaction dynamics was sought. Based on the results in section 4.1, the baseline bump spanwise shape was chosen. The ramp and tail angles were then altered independently to observe the unsteadiness changes. Hence, three bumps with alterations in the ramp and four in the tail angle each were designed resulting in seven bumps. The specifications of these bumps are tabulated in Table 3.3. Step changes of two degrees were made to observe a possible trend. An 'extreme' case was included which has a ramp angle of eleven degrees. The bumps are abbreviated as SCB - $r\theta_r$ - $t\theta_t$.

Table 3.3: Geometrical specifications of the bumps with variation in ramp and tail angle.

Bump design	w [mm]	l [mm]	θ_r [°]	θ_t [°]	h [mm]	l_r [mm]	l_t [mm]
SCBr7t5.5	150	85.9	7.0	5.5	4.63	38.0	48.3
SCBr11t5.5	150	71.9	11.0	5.5	4.63	24.3	48.3
SCBr13t5.5	150	68.2	13.0	5.5	4.63	20.6	48.3
SCBr9t3.5	150	105.0	9.0	3.5	4.63	29.6	75.9
SCBr9t7.5	150	64.5	9.0	7.5	4.63	29.6	35.5
SCBr9t9.5	150	56.9	9.0	9.5	4.63	29.6	28.1
SCBr9t11	150	53.1	9.0	11.0	4.63	29.6	24.3

3.3. Experimental Setup

This section discusses the experimental setup used for the investigation. First, the oil flow visualisation is discussed in subsection 3.3.1 which is succeeded by the Schlieren setup in subsection 3.3.2. The test matrices used for the experimental campaign are given in Appendix C.

3.3.1. Oil Flow Visualisation

The oil flow used for the experiments is a mixture of hydraulic oil, titanium dioxide, and oleic acid. Additionally, oleic acid is used to smooth the surface of the test section, and the oil is applied using a smooth brush. Figure 3.14 shows an example of how the oil is applied in the test section during experiments.

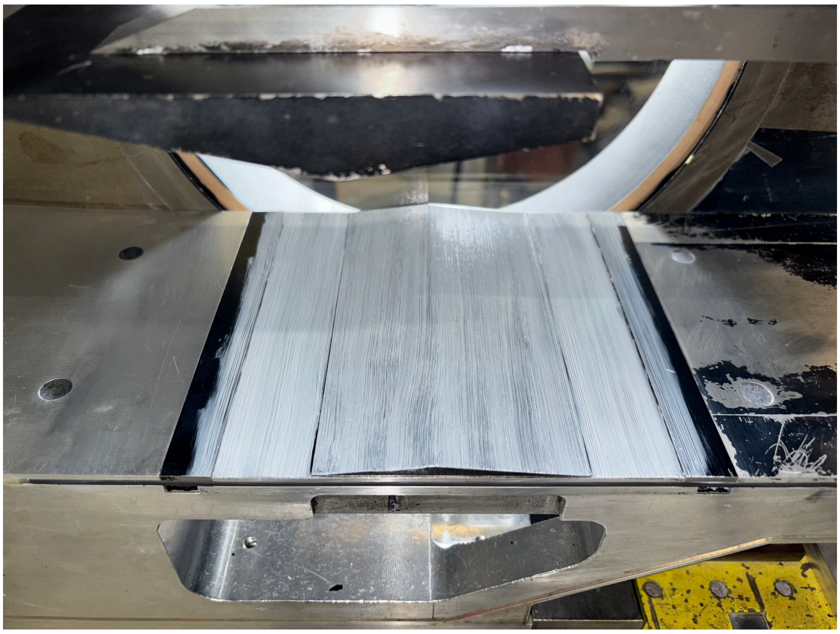

Figure 3.14: Application of oil in the ST-15 test section for oil flow visualisations (SCBr7t5.5). The flow goes from left to right.

During the start-up and shut-down of the wind tunnel, normal shocks traverse throughout the wind tunnel. When the oil is applied to the test section, these normal shocks can influence the flow pattern once it has not dried enough or has accumulated significantly in certain regions. To record and document these effects, a Nikon D7500 camera will be used in conjunction with two magnetic LED lights mounted on the wind tunnel test section frame. Figure 3.15 illustrates this set up. It enables detailed observation of the flow near the wind tunnel wall and facilitates the capture of oil flow images particularly when the pattern is affected by these shocks.

(a) The camera and LED light.

(b) The remaining LED light.

Figure 3.15: Oil flow visualisation test setup in the ST-15 with the camera and two magnetic LED lights.

3.3.2. Schlieren

As discussed in subsection 2.4.2, the Z-type Schlieren setup is used for this experimental investigation. Figure 3.16 and 3.17 shows the setup as used during the experiments, and the specifications of the individual parts are given in Table 3.4. The terminology is consistent with Figure 2.24, and two experimental campaigns were conducted. The first campaign, campaign A, consisted of the variation in spanwise design and impingement location. The second campaign, campaign B, consisted of the SCB geometry variation. The components used during both campaigns are tabulated in Table 3.4. Due to availability, two cameras were used and the specifications regarding acquisition rate, shutter speed, resolution, and test duration are tabulated in Table 3.5. This also includes the frequency range which can be captured in line with the Nyquist theorem. This theorem states that periodic signals must be sampled with a frequency twice the highest frequency of the signal itself in order to capture these signals accurately (Ziemer et al., 1998).

Figure 3.16: Complete Schlieren setup in the ST-15 wind tunnel including the associated numbers.

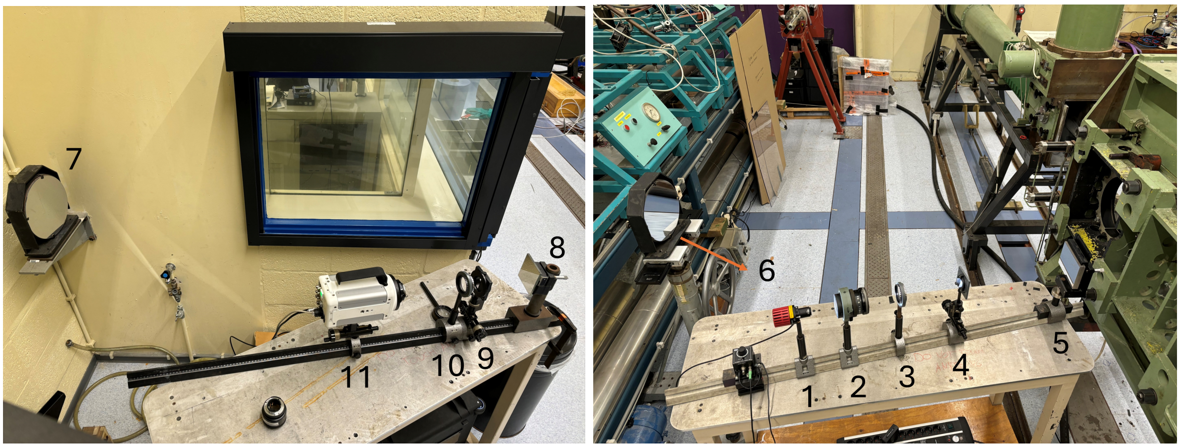

(a) Left side.

(b) Right side.

Figure 3.17: Schlieren setup used during the experiments with the associated numbers.

Table 3.4: Schlieren setup specifications per campaign and part number.

Part number	Campaign A	Campaign B
1	THORLABS MCWHLP1 White LED	
2	$F2.5$, f = 178 [mm]	
3	f = 200 [mm]	
6 & 7	f = 2,000 [mm]	
9	Vertical knife edge	
10	f = 400 [mm]	f = 300 [mm]
11	Photron FASTCAM SA1.1	Photron FASTCAM Nova S12

Table 3.5: Specifications of camera settings and obtained frames per experimental campaign.

	Campaign A	Campaign B
Acquisition rate (f_s) [kHz]	10	25
Nyquist frequency range [kHz]	5	12.5
Shutter speed [1/Hz]	1/12,000	1/40,000
Resolution [width x height]	768 x 768	1024 x 512
Test duration [s]	0.9701 (9701 frames)	1.745 (43642 frames)
Pixel size [width x height] [mm]	0.215 x 0.215	0.161 x 0.161

3.4. Data Processing Techniques

The obtained oil flow and Schlieren data are processed using different techniques which will be discussed in this section. In subsection 3.4.1 the shock detection method is discussed, and subsection 3.4.3 continues how the spectral analysis was performed. The section is concluded by the discussion on general statistical methods in subsection 3.4.4.

3.4.1. Shock Impingement and Separation Location Detection

For an inviscid shock reflection on a flat plate, the impingement location of the incident shock and reflection shock are collocated. However, in SWBLIs, the impingement and separation are at different positions. The difference between the locations represents the interaction length L_{int} and is indicative of the magnitude of the interaction. Also, the impingement and separation location through time can be used to obtain information about the fluctuating behaviour of the associated shock waves. Therefore, it is important to develop a method to calculate the impingement and separation location. There are various ways to approximate these locations, and this thesis uses a digital image processing technique to perform these calculations.

The pixel intensity given by the Schlieren images is the primary source for the shock detection method. To provide a guideline, consider Figure 3.18 which shows a flow diagram of the methods used to detect the impingement and separation shock location. This diagram has five processes and will be discussed individually:

1. Load the instantaneous Schlieren frame and subtract the background;
2. Apply edge-detection algorithm;
3. Define boxes;
4. Find points of the edges; and
5. Filter the outliers and perform linear regression.

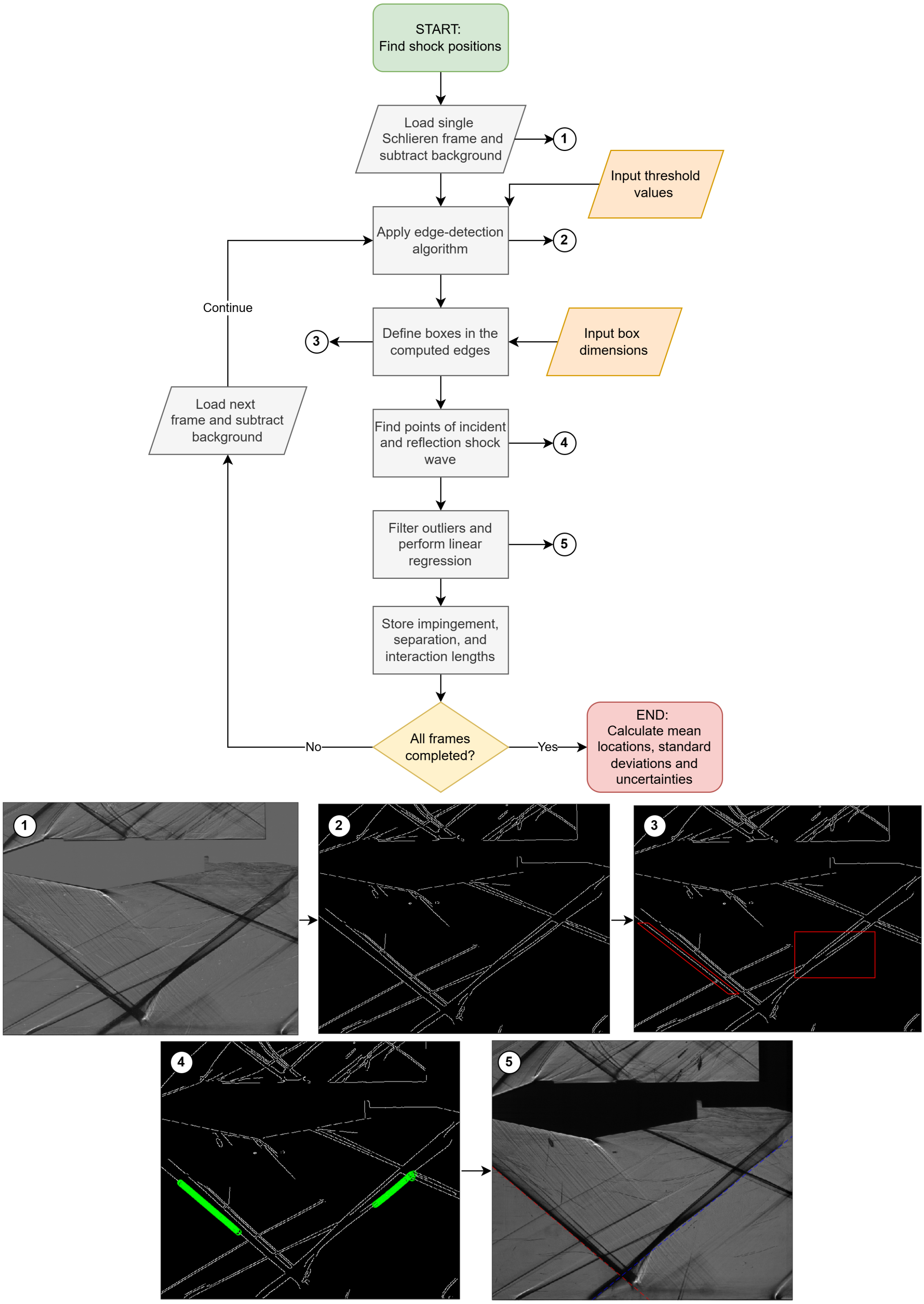

Figure 3.18: Flow diagram of shock detection method using the uncontrolled SWTBLI as an example.

Step 1: Load the instantaneous Schlieren frame and subtract the background.

The flow diagram starts at the top of Figure 3.18. For each flow case, the frames are analysed individually and have an associated resolution and pixel intensity. Often, Schlieren images contain a high level of random noise (i.e., 'salt-and-pepper' noise) which can originate from dusty lenses, photography surroundings, or digital cameras (Li et al., 2019; Nazari et al., 2020). The ways to mitigate random noise, for instance, are subtraction of the background image or the application of spatial Gaussian filtering. The subtraction of the background is advantageous since it removes imperfections in the optical windows of the wind tunnel (Li et al., 2019). Therefore, image subtraction is applied in the first step of the algorithm while Gaussian filtering is used by the edge-detection algorithm as described in subsection 3.4.2.

Step 2: Apply edge-detection algorithm[1].

The incident and reflection shock will be detected based on the variation in pixel intensity in the frame. When pixels are analysed in the streamwise direction, their intensity decreases progressively from the brighter upstream region to the darker region associated with the shock wave. This introduces a gradient in the pixel intensity, and there are different methods to identify an edge from this gradient. One possibility is to use image edge detection algorithms. Although there are multiple algorithms (e.g. Roberts and Sobel (Cui et al., 2013)), Estruch et al. (2008) and Li et al. (2019) argue that the Canny algorithm is a suitable method for digital image processing in high-speed Schlieren images. This is because the Canny algorithm uses Gaussian filtering to suppress noise and shrinks the edge to a thin line. Schlieren images often contain random noise, so the Canny algorithm has the potential to detect the edge correctly while not being fooled by the noise. The Canny edge-detection algorithm is explained in detail in subsection 3.4.2. The result of this algorithm is a $N \times M$ matrix corresponding to the frame resolution with zeros and ones where the ones indicate the edges in the Schlieren image (see (2) in the flow diagram).

Step 3: Define boxes.

As discussed in subsection 3.2.2, corner effects are present within the wind tunnel. These generate three-dimensional gradients in the density of the flow, and these can be observed by the Schlieren technique. Often, broad, low-intensity regions in the Schlieren image depict spanwise integration of three-dimensional gradients while concentrated, dark regions indicate nominal two-dimensional density gradients. Therefore, the impingement and separation location are influenced by the choice of the representative shock edge.

Consider (1) in the flow diagram. The impinging shock region shows multiple lines with the lowest line having the most distinctive character. The upper lines have a relatively lower intensity. Therefore, the lowest line is the most probable line of the impinging shock emanating from the shock generator. This edge was chosen for the calculation of the impingement location. The region of the reflection shock wave was used to calculate the separation location. This region is chosen since the unsteadiness in the separation shock is highly correlated with the fluctuating behaviour of the reflection shock (Clemens and Narayanaswamy, 2014). Therefore, the fluctuations observed in the separation shock are translated to the fluctuations of the reflection shock such that the edges in this region represent the fluctuations in the separation region. Depending on the edge intensity changes, the incident shock wave might require a different threshold range than the reflection shock wave. For this reason, before the complete set of images was analysed, a visual check was performed for an instantaneous Schlieren image to find a suitable threshold range for the incident and reflection shock edge. This resulted in two ranges, one for the incident edge and one for the reflected edge, which is kept constant for the entire set of frames. This also means that two separate edge detections were performed: one for the incident shock edge and one for the reflected shock edge. The utilised threshold ranges for the algorithm are tabulated in Table 3.6.

---

[1] The Canny edge detection was performed in MATLAB 2023a using the *edge* function of the Image Processing Toolbox.

Table 3.6: Thresholds used for the edge-detection analysis of the Schlieren frames. Values indicate [lowest threshold, highest threshold]. The maximum and minimum values of the threshold are 1 and 0, respectively.

	Uncontrolled	Basline	Short	Smooth	SCBr7t5.5	SCBr11t5.5	SCBr13t5.5	SCBr9t3.5	SCBr9t7.5	SCBr9t9.5	SCBr9t11
Incident edges	[0.1, 0.25]	[0.1, 0.3]			[0.2, 0.3]						[0.1, 0.2]
Reflection edges	[0.1, 0.3]	[0.1, 0.3]			[0.2, 0.3]						[0.1, 0.2]

After obtaining the sparse matrix, the incident and reflected shock points need to be retrieved. This is done by defining a box of suitable size at the expected location of the respective shock edges. An example of these boxes is given in red in (3) of the flow diagram. It is known that the variance of the incident shock is theoretically small. Hence, to exclude any spurious detections due to edges not associated with the incident shock, the incident shock box has a trapezoidal shape in the vicinity of this shock. The box of the reflection shock is rectangular since the fluctuating behaviour is unknown for the (un)controlled cases.

Step 4: Find the points of the edges.

For the next step, consider (4) in the flow diagram. This figure shows the points in green which have been detected as 'the correct edge' of the incident and reflection shock wave. To consider this process more closely, take the incident edge box with its zeros and ones. From the Schlieren images, the incident shock wave is probably located at the lowest edge in the incident box. Therefore, the incident box must be traversed in an upward direction for each column in the box to find the correct edge. When this is done for each column continued in the streamwise direction, the points shown in green are obtained. The same method is applied to the reflected shock edge only now in a row-wise manner rather than a column-wise manner.

Step 5: Filter the outliers and perform linear regression[2].

At this stage, all necessary information has been obtained to compute the location of the impingement and separation location. This will be done using linear regression of the obtained points, and outliers are filtered according to the 3σ-method discussed in subsection 3.4.4. The impingement and separation location are then extrapolated to the wind tunnel wall. This is visualised in (5) in the flow diagram where the red dashed line represents the incident shock wave and the blue dashed line the reflection shock wave. Finally, the impingement, separation, and interaction length are computed and stored. The five steps will be repeated for every Schlieren frame, and all the obtained data will be stored for further analyses when all the frames have been analysed.

3.4.2. Canny Edge-Detection Algorithm

As discussed in subsection 3.4.1, the Canny edge-detection algorithm is used as a digital image processing technique to detect the incident and reflection shock wave edges. The technique determines the edges according to the following steps (Cui et al., 2013; Forsyth and Ponce, 2011):

1. Smoothing the pixels by applying a Gaussian filter $G(x, y)$;
2. Compute the magnitude of the pixel intensity gradient $\|\nabla I(x, y)\|$;
3. Determine the orientation of the boundary $\hat{n}_{\nabla I}$;
4. Perform a non-maximum suppression or 'edge-thinning'; and
5. Apply hysteresis thresholding to detect connecting edges.

1. Smoothing of the image.

In general, every image has a certain level of noise which can influence the detection of 'true' edges. If an image has a high degree of noise, the algorithm can detect additional edges which might not represent the true edges. The Canny algorithm smoothens the image by assuming an Additive White Gaussian Noise (AWGN) model in the images with constant standard deviation. It applies a Gaussian filter as given in Equation 3.1

$$G\left(x, y\right) = \frac{1}{2\pi\sigma^2} e^{-\frac{x^2+y^2}{2\sigma^2}}, \tag{3.1}$$

---

[2] The linear regression was performed using the *polyfit* and *polyval* functions in MATLAB 2023a

where x, and y represent, in the case of the Schlieren images, the streamwise and wall-normal direction, respectively. The standard deviation σ influences the spread of the Gaussian distribution or how many pixels will be smoothened because of the filter. A low value suggests that a few surrounding pixels will be smoothened, and a higher value indicates that more surrounding pixels will be smoothened. The default MATLAB value of $\sqrt{2}$ is used here. Next, the gradient of the pixel intensity will be calculated by convolution of the pixel intensity with the gradient of the Gaussian filter in its respective direction (Equation 3.2 and 3.3)

$$I_x = \frac{\partial I}{\partial x} = \frac{\partial}{\partial x} I * G = I * G_x, \qquad I_y = \frac{\partial I}{\partial y} = \frac{\partial}{\partial y} I * G = I * G_y, \tag{3.2}$$

where

$$G_x = \frac{-x}{\sigma^2} G(x,y), \quad \text{and} \quad G_y = \frac{-y}{\sigma^2} G(x,y). \tag{3.3}$$

2. Magnitude of intensity gradient.

Step one results in a two-dimensional distribution of the gradient in the pixel intensity after applying a Gaussian filter. Based on the magnitude of the gradients, maxima and minima can be found which indicate the location of the edges. The magnitude of the pixel intensity gradient is calculated using Equation 3.4. The result is then a two-dimensional distribution containing the variation in gradient magnitude $\|\nabla I(x,y)\|$

$$\|\nabla I(x,y)\| = \sqrt{I_x^2 + I_y^2}. \tag{3.4}$$

3. Boundary orientation.

The next step is a preparatory step for the non-maximum suppression, and it determines the orientation of the gradient magnitude (or preliminary edges) of step two. The orientation is calculated in Equation 3.5 which is the unit normal vector

$$\hat{n}_{\nabla I} = \frac{\nabla I}{\|\nabla I(x,y)\|}. \tag{3.5}$$

4. Non-maximum suppression.

At this stage, a gradient distribution has been obtained together with the orientation of the local maxima in this distribution. It can be the case that the local maximum in a certain region is spread over multiple pixels, and in this case, a 'true' edge can not readily be determined. Consider Figure 3.19 where the left figure shows the grey-scale gradient magnitude distribution including pixel point q and point p and r along the direction of the gradient. The right shows the corresponding pixel grid including the aforementioned points and the orientation of pixel q. The goal is to find the local maximum value in the gradient along its direction and suppress those values which are lower than the maximum value. In this way, the edge is thinned to a single pixel instead of a region as shown in the left figure. The procedure is as follows. Take the gradient magnitude in q and compare this to the values in p and r. If the value in q is larger than in p and r, then q is an edge and will be given a '1'. If this is not the case, q will be given a '0' and the algorithm continues to the next pixel. The result is a $N \times M$ matrix corresponding to the frame resolution containing the determined edges. As seen on the right in Figure 3.19, it is possible for the points to not pass through a convenient pixel in the grid (p and r). In that case, a linear interpolation is applied to obtain the gradient magnitude. Suppose q is an edge, then the algorithm searches for the next point in the grid by following the perpendicular direction of the boundary orientation as shown by the red arrow. This is because the most likely position of the next edge point will be perpendicular to the previous edge point.

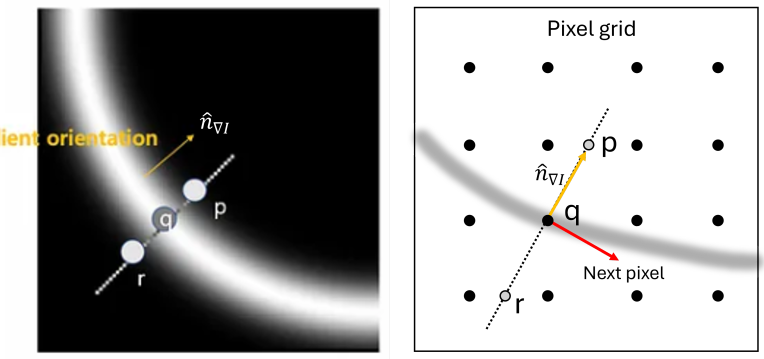

Figure 3.19: Visualisation of the non-maximum suppression in the Canny edge-detection algorithm. The left shows the gradient magnitude distribution (black/white), and the right shows the pixel grid.

5. Hysteresis thresholding.

The final step applies thresholding to distinguish connecting and non-connecting edges. Thresholding can be seen as a way to separate edges with low gradient magnitudes from those with high gradient magnitudes. Therefore, edges with a high magnitude correspond to higher threshold values and low magnitude edges with low thresholds. For the Canny algorithm, a maximum and minimum threshold can be initialised. This can be seen in the sketch given in Figure 3.20. The algorithm starts with the high gradient magnitude edges with the high threshold value (blurred in grey) and decreases the threshold to 'reveal' new edges (the layers underneath). If the new edge points are directly next to the edges with the high threshold, the new edge is considered part of the whole edge. If the new edge is located further from the original edge, it is not considered to be part of the whole edge but as a new edge. This procedure is applied until the lowest threshold value has been reached. At this stage, the Canny algorithm retrieved the black level and completed finding the edges. The advantage of this threshold handling is that it only connects edges to existing edges rather than showing all computed edges as the threshold reduces.

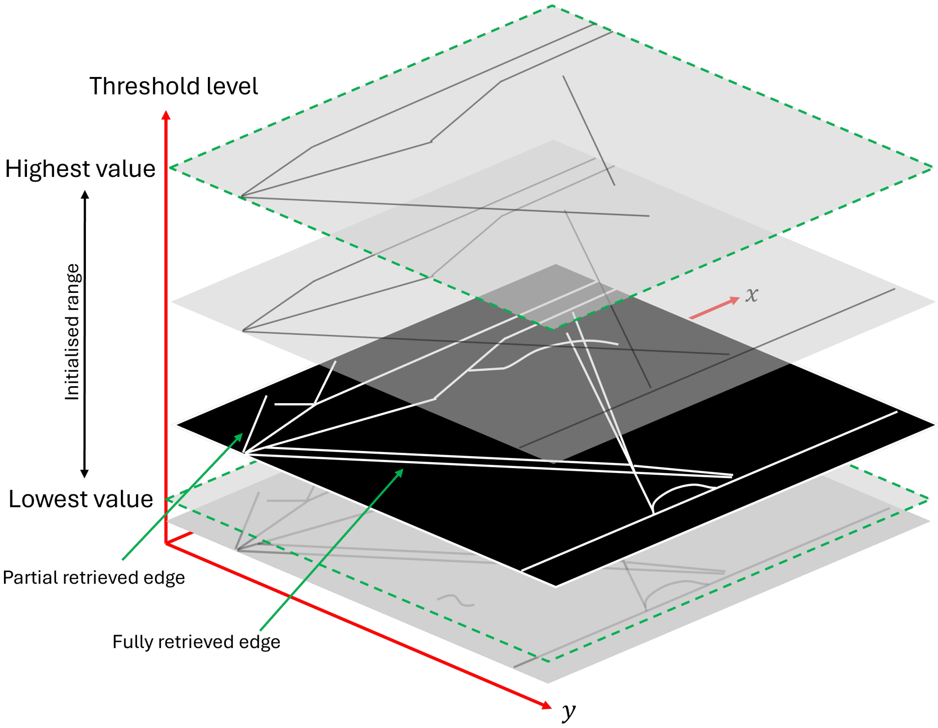

Figure 3.20: Sketch of the hysteresis thresholding within the Canny algorithm.

3.4.3. Frequency-Domain Analysis

Frequency-domain or spectral analysis is used to assess the unsteady behaviour of the oblique SWTBLI with SCBs. This analysis was based on the fluctuations of the pixel intensity obtained from the Schlieren images. Hence, when performing a spectral analysis, the fluctuation of the pixels through time was considered. Suppose there are N observations of the intensity of an individual pixel. Then, this time domain signal $x(t)$ can be transformed to a frequency domain signal $X(f)$ using the Fourier transform as shown in Equation 3.6 where f is the frequency and $i = \sqrt{-1}$

$$X(f) = \int_{-\infty}^{\infty} x(t)e^{-i2\pi ft}dt. \tag{3.6}$$

This equation is in its continuous form. Evidently, the signal is in a discrete form, so the Discrete Fourier Transform (DFT) is used as shown in Equation 3.7 (Ziemer et al., 1998)

$$X_k = \sum_{n=0}^{N-1} x_n e^{\frac{-i2\pi kn}{N}}, \tag{3.7}$$

where x_n is the observed value at the n-th sample, X_k is its DFT, and $k = 0 : N-1$. When the signal comprises pure sine- and cosine waves, the Fourier transform alone is a suitable method for spectral analysis. However, the signal in experimental observations often contains random fluctuations or noise. This gives a frequency-domain signal which is unsuitable for adequate spectral analysis, so a different method has to be used to perform an appropriate analysis. The method of Welch (1967) is such a method and calculates the Power Spectral Density (PSD) of modified periodograms. The *pwelch* function of MATLAB (2023a) Signal Processing Toolbox was used to perform these operations.

The general idea is to split the whole signal $x(t)$ into K segments or *windows* of length L to obtain K segments of $x_j(t), j = 0, ..., L$. When the PSD is computed for this segment, a significant amount of energy is associated with the strong non-stationarities at the edges of the signal. This causes artefacts or 'edge effects' in the Fourier transform which have to be omitted. Therefore, a windowing technique is used such that the time signal near the edges of the segments is reduced to zero. A frequently used window for the Welch method is the Hamming window which takes the form of a symmetrical cosine wave (Iwata et al., 2016). If a Hamming window of the same length as the segment length x_j is multiplied by this signal ($x_j(t)w_j(t)$), the amplitude near the edges will go to zero whereas the middle of the signal is retained. Additionally, an overlap of the segments is applied to retrieve the signal where its value was originally reduced to zero. Of this segment, a PSD is calculated which is referred to as a modified periodogram. The mathematical formulation of the PSD is given in Equation 3.8

$$P_j(f) = \frac{1}{N}\left|\sum_{j=0}^{L-1} x_j(t)w_j(t)e^{\frac{-i2\pi fj}{N}}\right|^2. \tag{3.8}$$

The modified periodograms will then be averaged to obtain the averaged PSD as defined in Equation 3.9. This PSD has 2^p points where $p = log_2(N/4.5)$ rounded off to the nearest integer. The frequency resolution in turn becomes $f_s/(2 \cdot 2^p)$ where f_s is the acquisition rate[3]. For the spectral analysis, it is more helpful to quantify the content in terms of a pre-multiplied PSD ($f \cdot P(f)$) such that every frequency has an associated energetic value instead of a density value

$$P(f) = \frac{1}{K}\sum_{j=1}^{K} P_j(f). \tag{3.9}$$

An advantage of the Welch method is that the noise is reduced in the spectral domain due to the averaging of K segments. Furthermore, the windowing technique ensures that edge effects are reduced

---

[3] See MATLAB *pwelch* documentation: https://nl.mathworks.com/help/signal/ref/pwelch.html.

and the power is correctly associated with its frequencies. A disadvantage is that, for increasing segments, spectral content is equalised and the frequency resolution is reduced. Therefore, the number of segments K must be chosen to obtain a balance between noise and spectral content. A window length of 512 frames is used for the measurements of campaign A, and the standard MATLAB setting of $K = 8$ segments is used for measurements of campaign B. All cases have an overlap of 50%.

The spectral analysis will be performed in so-called *spectral boxes* defined in Figure 3.21. The box has a trapezoidal shape to obtain pixel intensities parallel to the separation shock. The intensity of each pixel was obtained from the instantaneous Schlieren frame such that a time signal was retrieved (step 1). The box was then skewed to create a rectangular one (step 2), and the Welch method was performed in each pixel (step 3). All PSDs were then averaged to a single pixel height (step 4) to obtain an averaged PSD distribution of the separation shock wave. The box is positioned in the separation shock region because, as discussed in section 2.2, low-frequency unsteadiness of the shock system can be detected in the separation region of the interaction.

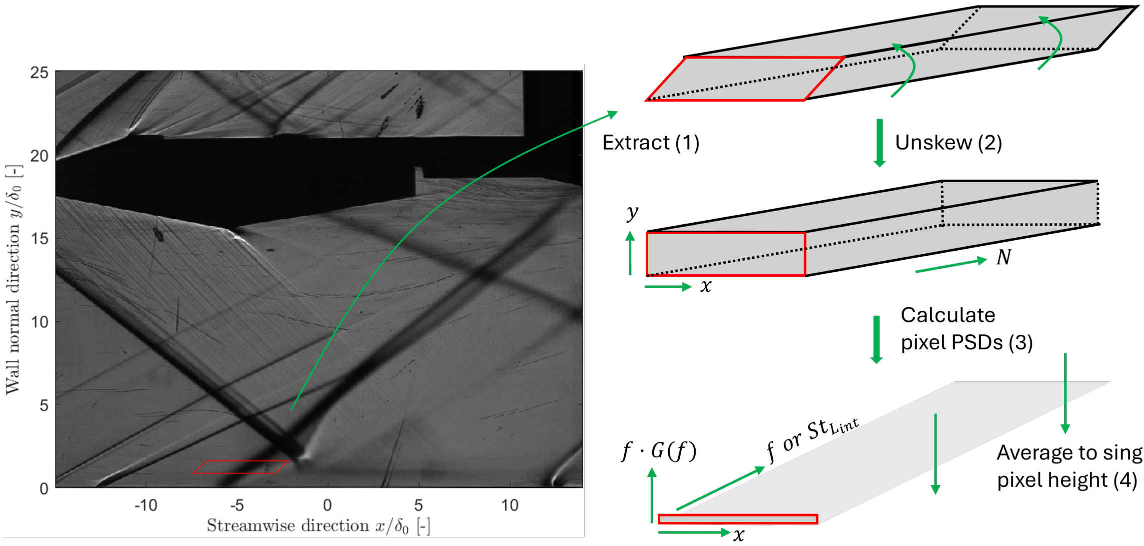

Figure 3.21: Process of extracting, skewing, and calculating the data needed to form a pre-multiplied PSD distribution of the separation shock region: step 1) extracting the data, 2) skew the box, 3) calculate PSD data, and step 4) average to single pixel height.

3.4.4. Statistical Methods

In any measurement or computational process, it is possible to obtain values that seem to be far from the mean value. This value can be classified as an 'outlier', and the 3σ-method is a frequently used heuristic for outlier detection. To explain this, consider the standard deviation in Equation 3.10. In this equation, y_i are the observed values and $\bar{y}$ is the mean of these values. The standard deviation can be seen as a measure for the variance of the observed values around its mean[4]

$$\sigma_y = \sqrt{\frac{\sum_{i=1}^{N} (y_i - \bar{y})^2}{N - 1}}. \tag{3.10}$$

Suppose, during a measurement, there is a set observation y_i with a mean $\bar{y}$. Then, the observations within the interval $y_i - 3\sigma \leq y_i \leq y_i + 3\sigma$ are retained, and values larger or smaller than 3σ are discarded as outliers. This method assumes that the data follows a normal or Gaussian distribution, and 99.7% of the observed values are within this confidence interval. This method is applied to the points for the linear regression in step 5 of subsection 3.4.1 and the calculation of the impingement and separation location.

---

[4] The mean and standard deviations were calculated using the *mean* and *std* functions in MATLAB 2023a.

While the 3σ-method identifies 'outliers' of the observed data, the standard deviation can also be used to quantify the *uncertainty* of the mean value. The mean value uncertainty is given by Equation 3.11 for the standard deviation σ_y and N observations. While this uncertainty is associated with the random process (i.e. if N increases, the uncertainty reduces), there might also be a systematic error due to, for instance, a change in environmental characteristics or measurement drift. The quantification of the uncertainty and error sources in the Schlieren technique is difficult due to the qualitative nature of the technique, so the quantification must be assessed with care

$$\epsilon_y = \frac{\sigma_y}{N}. \tag{3.11}$$

4

Results and Discussion

This chapter presents and discusses the results of the experimental campaigns. Campaign A is discussed in section 4.1 and campaign B is discussed in section 4.2. A discussion on the methods is given in section 4.3.

4.1. Results and Discussion of Campaign A

This section discusses the results of experimental campaign A. This campaign investigated the spanwise geometry (subsection 4.1.1) and the impinging shock location (subsection 4.1.2) on the bump.

4.1.1. Variance of Spanwise Geometry

This section discusses the results of the variance in bump spanwise shape. It is divided into the discussion of the Schlieren and oil flows, the impingement and separation location from the edge-detection algorithm, and the spectral analysis.

Schlieren and Oil Flow Visualisation

An explanation of the global elements of the uncontrolled oblique SWTBLI in the average Schlieren image is given in Figure 4.1. The grey-scale image is given in spatial coordinates nondimensionalised by the boundary layer thickness δ_0. Shock waves and expansion regions are expected to be darker and brighter, respectively, relative to the free-stream because of the orientation of the knife-edge. As such, the incident shock (red dashed line) and the reflection or separation shock (blue dashed line) can be identified. These lines are computed using the edge-detection algorithm, and the intersection of the red and blue dashed line with the $y = 0$-axis represents the extrapolated impingement and separation location, respectively. The extrapolated impingement location represents the origin of the streamwise axis. A recirculation region (i.e. separation bubble) downstream of the separation shock can be identified followed by a transmitted shock and expansion fan above this region. A weak reattachment shock can also be identified. The Mach waves and expansion fan emanating from the shock generator and the Mach waves from the wind tunnel wall are not considered to influence the main interaction. Small dents and stripes can be seen which are due to imperfections of the optical windows and PIV seeding of experiments previously performed in this wind tunnel. Finally, the grey-scale of the free-stream flow represents the flow without density gradients.

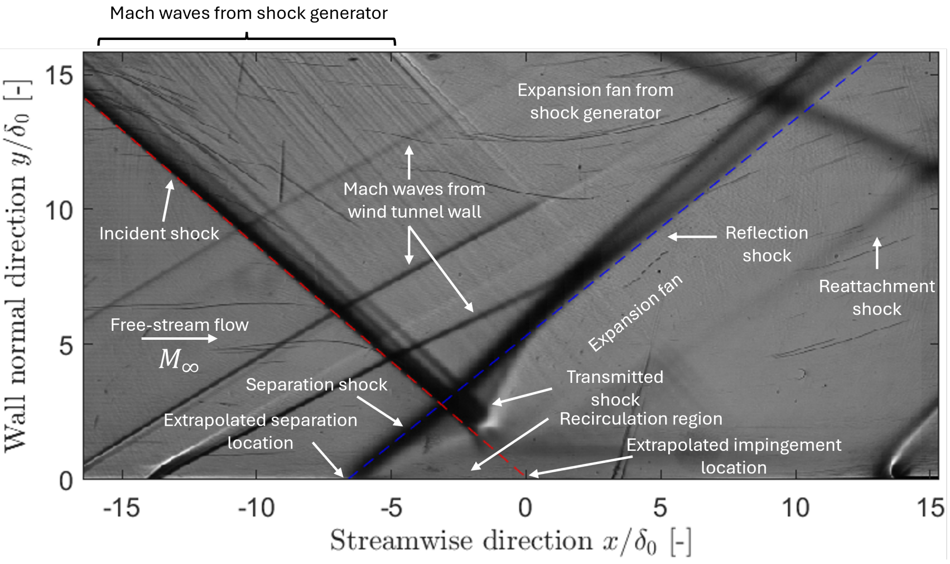

Figure 4.1: Explanation of the global elements in an average Schlieren image for the uncontrolled oblique SWTBLI.

The average Schlieren images with annotations for the spanwise variation in bump design are given in Figure 4.2. For comparison, the reflection shock line of the uncontrolled interaction is included as a grey dashed line in the bump interactions. Finally, the average Schlieren image for the baseline bump without impinging shock is given in Appendix A.

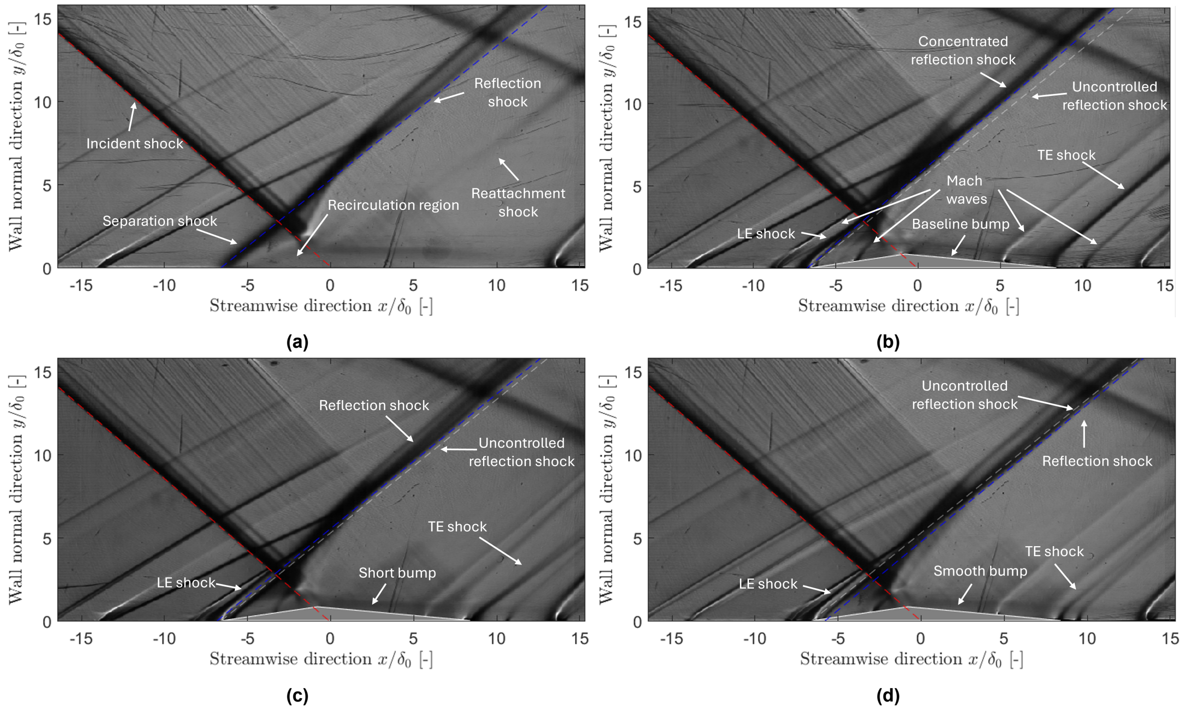

Figure 4.2: Average Schlieren images of the oblique SWTBLI for the a) uncontrolled, b) baseline, c) short, and d) smooth bump interaction. Figures include the impingement (red), reflection (blue), and the reflection shock line of the uncontrolled interaction (grey). Spatial coordinates are nondimensionalised by δ_0 and the bumps are shown in grey.

In Figure 4.2a, the typical features of an uncontrolled oblique SWTBLI can be observed. Figure 4.2b shows the same interaction but with the baseline bump installed. The separation shock appears to be replaced by a Leading Edge (LE) compression ramp shock, and the reattachment shock seems to be removed. Now, a Trailing Edge (TE) shock is generated near the bump trailing edge. Also, Mach waves are seen near the bump leading and trailing edge due to thin pieces of tape to smoothen the transition between plate and bump. The Mach waves are considered to have minimal effect on the interaction. Considering Figure 4.2c and 4.2d, only slight differences are observed at the reflection shock wave where the region seems to be more concentrated in the smooth bump case relative to the short bump case.

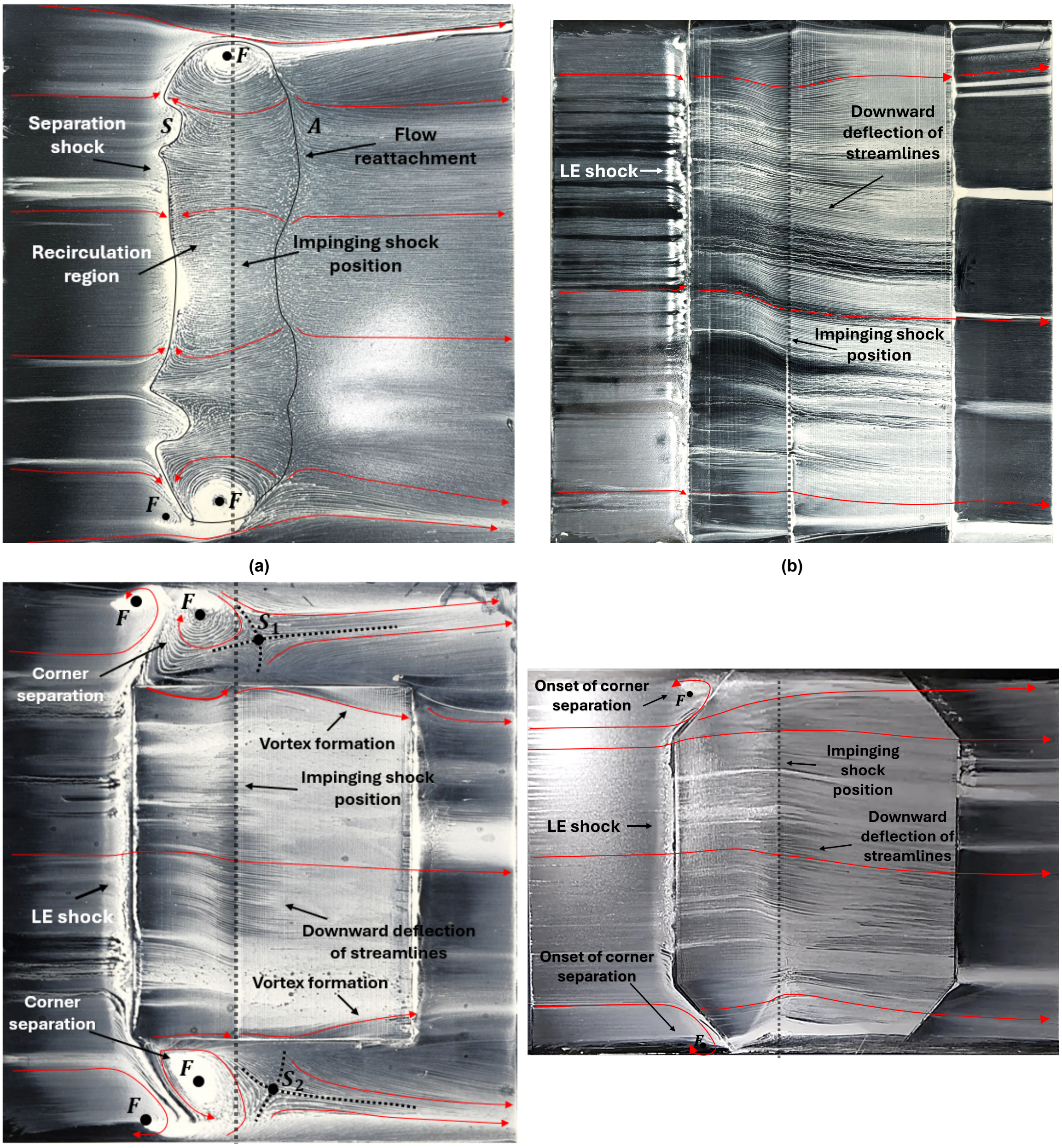

(a)

(b)

(c)

(d)

Figure 4.3: Oil flow visualisation including annotations for the a) uncontrolled, b) baseline, c) short, and d) smooth bump interaction. Red indicates the direction of the streamlines, and annotations for critical point theory is included.

The oil flows of the spanwise variance in geometry are given in Figure 4.3. The pieces of tape generating the Mach waves in the Schlieren images were removed for the oil flow experiments to improve the flow of the oil on the bump. The images include annotations for the streamlines (red) and the critical point theory (black). In Figure 4.3a, an upstream, recirculating, and downstream region is observed. The separated region is annotated by a black line, the separation line by (S), and the re-attachment line by (A). Additionally, three focal points are seen near the wind tunnel walls, and irregularities at equidistant locations from the wind tunnel side walls are seen in the separation line. Although these are considered to not affect the primary interaction, it is suspected that it results from the Mach block imperfections shown in Figure 4.4 which have a dimple shape. Dimples are known to generate local pairs of streamwise vortices (Mahmood et al., 2000) and add momentum to the boundary layer flow. This local addition could excite a downstream movement of the separation shock since Beresh et al. (2002) argued that positive velocity fluctuations in the upstream boundary layer cause a downstream movement of the separation shock (see also Figure 2.9 in subsection 2.2.2). It seems that it only affects the separation and not the reattachment of the flow.

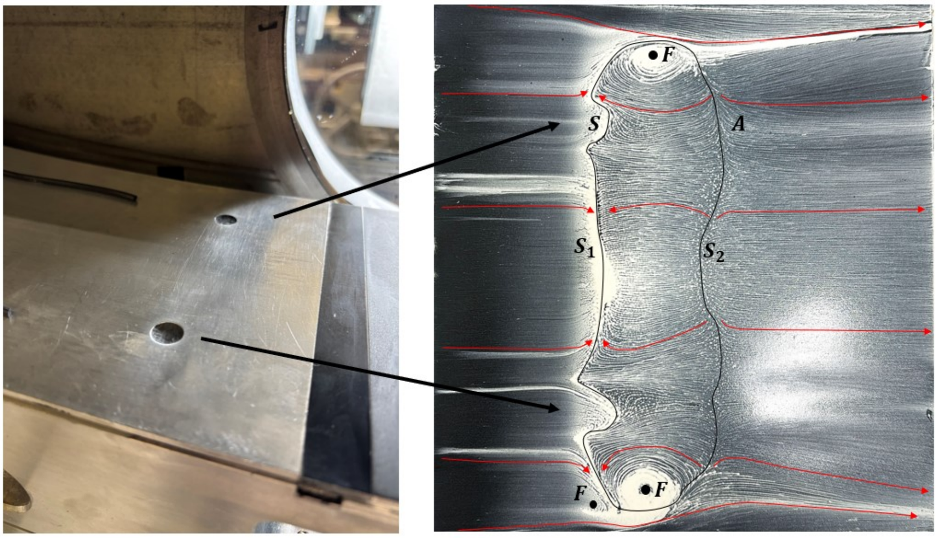

Figure 4.4: Upstream dimples of the Mach block in the wind tunnel and the effect on the interaction in the oil flow visualisation.

For the baseline bump interaction in Figure 4.3b, it appears that flow remains attached to the bump. Furthermore, the uncontrolled separation shock seems to be replaced by a compression ramp shock from the bump LE; the interaction is mainly two-dimensional. However, streamlines deflect to the lower wind tunnel wall when approaching the bump crest. Small irregularities in the oil flow depict PIV seeding of previous experiments. The short bump interaction in Figure 4.3c shows a more symmetrical, three-dimensional behaviour: four focal and two saddle points near the wind tunnel walls and vortex formation at the tail part of the bump edges. The same deflection of the lines is seen at the centreline of the bump. Also, it seems that the compression ramp shock is bent in the spanwise direction between the bump edges and the wind tunnel walls. This is also observed in experimental investigations of three-dimensional bumps by Ogawa and Babinsky (2008) and Ogawa et al. (2008) (see Figure 2.14), and it contributes to the low-intensity region observed in the short bump reflection shock wave. This is an important observation since it can influence the computation of the edge-detection algorithm. Finally, Figure 4.3d shows the smooth bump interaction with two focal points close to the wind tunnel walls and the bump leading edge. The flow remains attached to the bump.

Asymmetry in the interaction is mainly observed for the uncontrolled interaction and the downward deflection of the streamlines on all bumps. This asymmetry can originate from upstream influences in the wind tunnel (artificial roughness), step changes between the wind tunnel Mach block and clamps, roughness on the shock generator, or misalignment of this generator. The last effect is believed to generate asymmetry because a visual inspection revealed a deviation between the shock generator and the support system of the generator. The exact deviation was not documented, but it is in the order of 2-5 mm between the shock generator and the support system over a distance of around 150 mm. This would give a deviation between the streamwise axis and the shock generator of approximately 0.8° - 2.0° resulting in a spanwise velocity component of 7 m/s - 17 m/s ($0.01u_\infty - 0.03u_\infty$) which is considered sufficiently small such that it does not influence the streamwise interaction. This misalignment was revealed during campaign B, and only the oil flow of the uncontrolled interaction was repeated after aligning the shock generator. This improved version is given in Figure 4.3a.

Impingement and Separation Locations of the Edge-Detection Algorithm

The following histograms, given in Figure 4.5, show the results of the edge-detection algorithm. The extrapolated impingement and separation location are presented in the nondimensional streamwise direction and number of occurrences. Again, the origin for all histograms is taken as the inviscid impingement location of the uncontrolled interaction. The black squares indicate the bump leading edge.

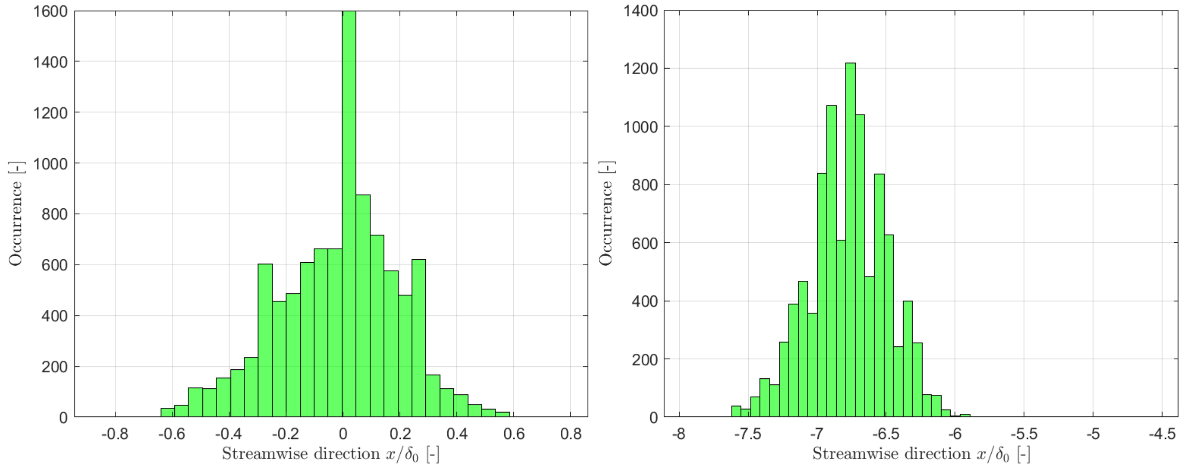

(a) Impingement location.

(b) Separation location.

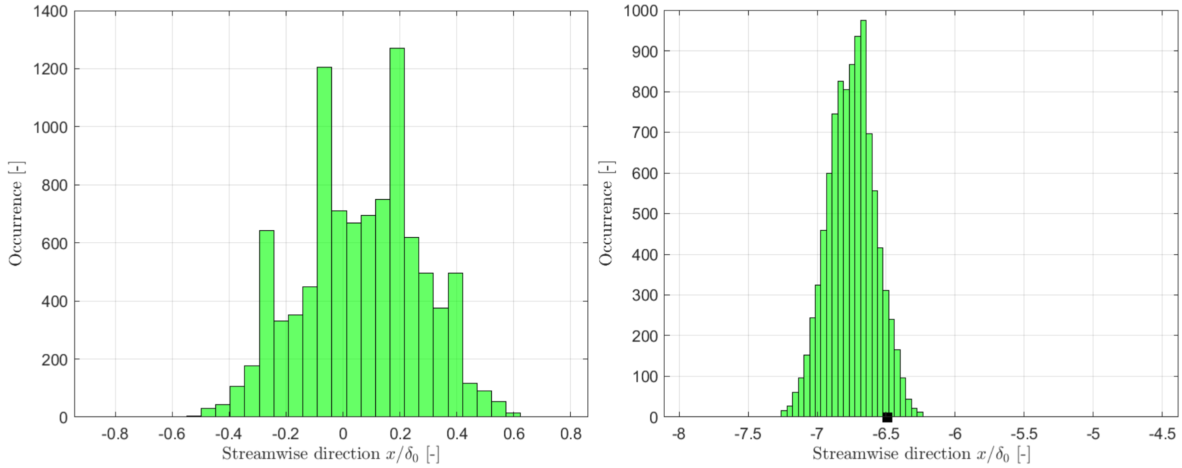

(c) Impingement location.

(d) Separation location.

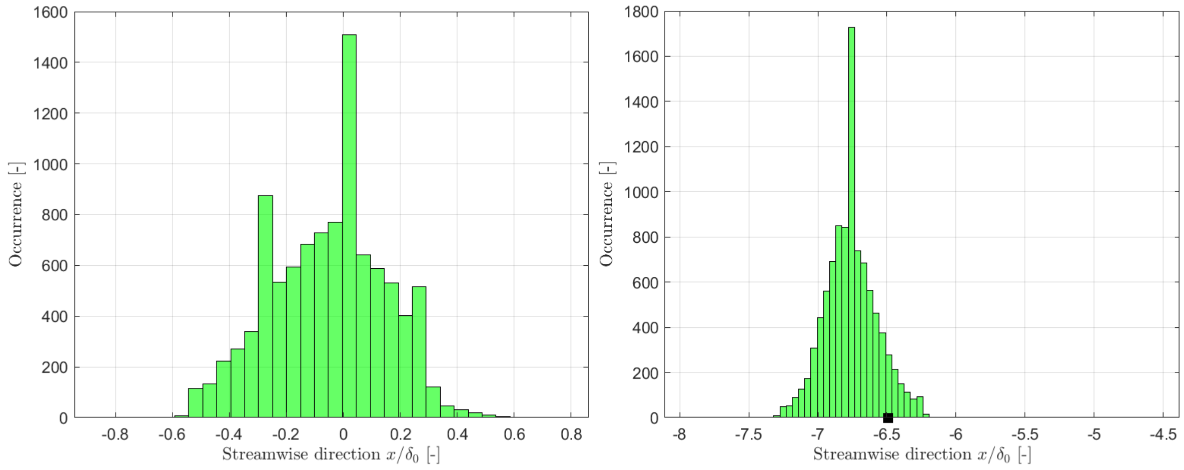

(e) Impingement location. **(f)** Separation location.

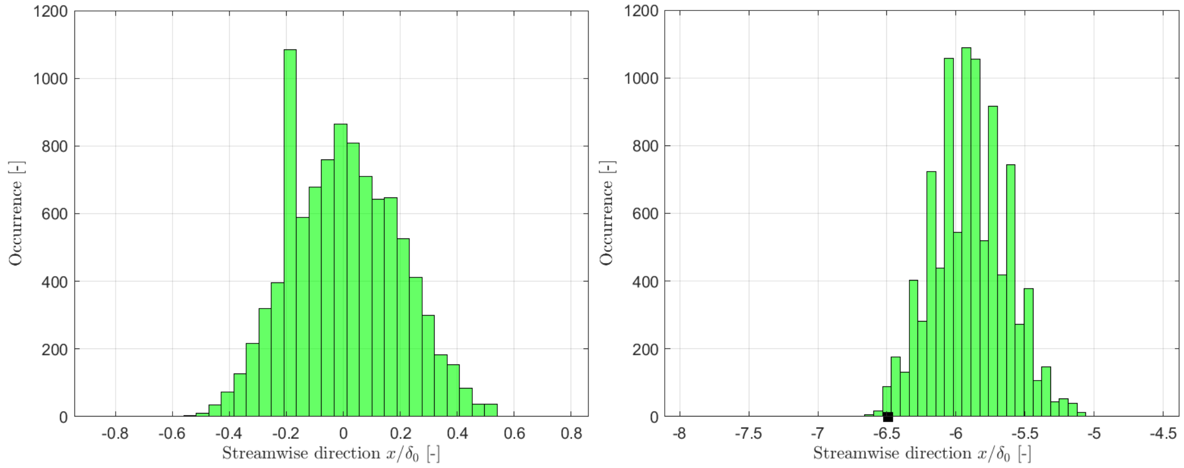

(g) Impingement location. **(h)** Separation location.

Figure 4.5: Histogram data of the impingement and separation location using the edge-detection algorithm for the uncontrolled (a-b), baseline (c-d), short (e-f), and smooth (g-h) bump interaction (bins = 25, 3σ-method applied). Black squares indicate the bump leading edge.

Considering Figure 4.5a, it shows a normal distribution-like behaviour centred around $x/\delta_0 \approx 0.0$. Similar findings are observed for the other impingement location histograms. The separation shock histogram in Figure 4.5b seems to be centred around $x/\delta_0 \approx -6.75$. The separation shock histograms for the baseline (Figure 4.5d) and short bump (Figure 4.5f) appear to be relatively more concentrated upstream of the bump leading edge. These are centred at a similar location as the uncontrolled interaction. The smooth bump separation shock in Figure 4.5h, however, has a larger spread downstream of the bump leading edge. A more quantitative summarisation of the histograms is given in Table 4.1. This table includes the mean value of the impingement and separation location $\bar{x}/\delta_0$, its associated standard deviation σ/δ_0, the mean interaction length $\bar{L}_{int}/\delta_0$, and the associated uncertainties ϵ of the mean impingement and separation locations. The standard deviation of the baseline and short bump interaction decreases relative to the uncontrolled interaction, and the standard deviation of the incident shocks largely remains around $\sigma_{inc}/\delta_0 = 0.2$.

Table 4.1: Quantification of the mean impingement and separation location $(\bar{x}/\delta_0)$ per interaction case including its standard deviation σ/δ_0, interaction length $\bar{L}_{int}/\delta_0$ and uncertainties ϵ.

Cases	$(\bar{x}/\delta_0)_{sep}$ [-]	$(\bar{x}/\delta_0)_{inc}$ [-]	σ_{sep}/δ_0 [-]	σ_{inc}/δ_0 [-]	$\bar{L}_{int}/\delta_0$ [-]	ϵ_{sep} [m]	ϵ_{inc} [m]
Uncontrolled	-6.77	-0.013	0.280	0.208	6.76	$1.48 \cdot 10^{-4}$	$1.10 \cdot 10^{-4}$
Baseline	-6.74	0.062	0.171	0.208	6.80	$9.01 \cdot 10^{-5}$	$1.10 \cdot 10^{-5}$
Short	-6.76	-0.052	0.187	0.198	6.71	$9.85 \cdot 10^{-5}$	$1.05 \cdot 10^{-5}$
Smooth	-5.89	0.004	0.268	0.189	5.89	$1.42 \cdot 10^{-5}$	$9.99 \cdot 10^{-5}$

The average uncontrolled interaction length computed by the edge-detection algorithm agrees with experiments by, among others, Bulut et al. (2024). The fluctuating behaviour of the separation location is suppressed when installing a bump indicating that the bumps remove the fluctuating behaviour of the separation shock. The reduction in interaction length for the smooth bump interaction can originate from the integration effect of the Schlieren technique. Near the wind tunnel side walls, the bump leading edges are tapered. This leads to a compression ramp shock being generated at a downstream location compared to the bump leading edge of the centred interaction. Combining this with the focal point formation near these tapered edges, the reflection shock in the Schlieren images appears to be at a more downstream location resulting in a decrease in a downstream separation location and reduction in mean interaction length.

The standard deviation of the impinging shock remains around $\sigma/\delta_0 = 0.2$. Furthermore, the separation standard deviations of the baseline and short bump interaction are smaller than the impinging shock deviation. Therefore, the impinging shock has some fluctuating behaviour which is not expected. This also questions the validity of the separation location results. It could originate from shock generator roughness or turbulence levels in the wind tunnel, but it seems that it results from noise levels in the images. Despite the effort of the Canny-based algorithm to mitigate noise by Gaussian filtering the pixels, the noise still affects the results. Hence, the results of the edge-detection algorithm must be treated with caution. Its effect can also be seen as the measurement uncertainty of the Schlieren technique. Finally, the uncertainties associated with the mean impingement and separation location are of the order of $\mathcal{O}(10^{-4}) - \mathcal{O}(10^{-5})$ showing that the uncertainty is smaller than the pixel size of $2.15 \cdot 10^{-4}$. Hence, the calculation errors are probably not influenced by the random error between measurements but rather by systematic errors from a different source.

It appears that the algorithm results are inconclusive for the unsteadiness of the shock system. It can be questioned if the motion of the separation shock through time can be used to draw conclusions about the unsteadiness of the shock system. In this case, the information provided by the algorithm can still be used. The separation shock location through time of the uncontrolled interaction is given in Figure 4.6a in normalised coordinates. A corresponding spectral analysis of this signal is provided in Figure 4.6b ($f_s = 10$ kHz, $K = 8$ segments). This figure shows the pre-multiplied variance-normalised PSD of this signal in terms of the interaction length-base Strouhal number. The variance represents the integrated PSD over all frequencies. Literature frequently reports the Strouhal number of $St_{L_{int}} \approx 0.03$ as characteristic low-frequency of the uncontrolled separation shock (e.g. Touber and Sandham (2009)), but the results do not show any of these characteristic frequencies. Hence, it seems that the results of the edge-detection algorithm are inconclusive for the unsteady dynamics. The performance of the edge-detection algorithm regarding noise filtering and the calculation of edges is explored further in subsection 4.3.2.

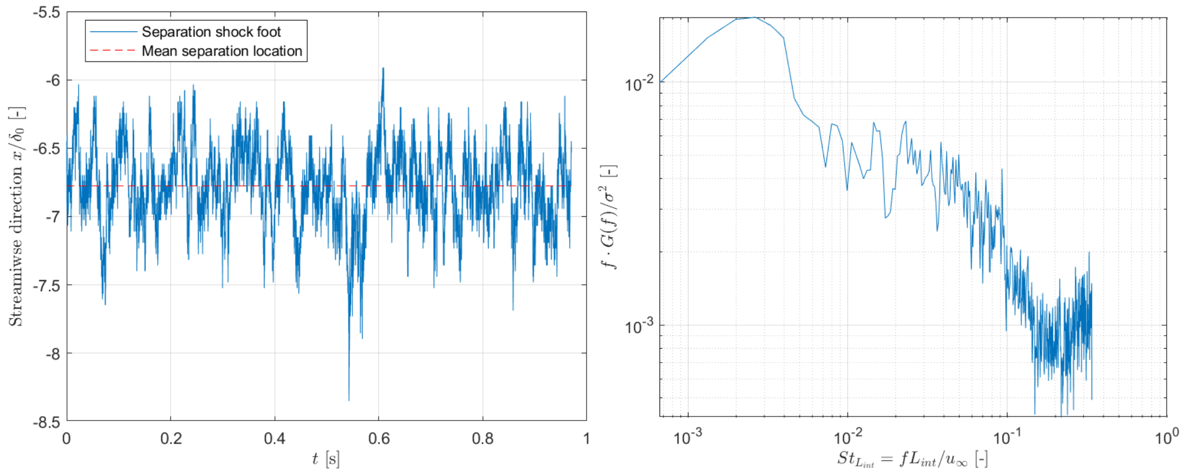

(a) (b)

Figure 4.6: Left: uncontrolled separation location (blue) through time from the edge-detection algorithm including the mean position (red). Right: corresponding pre-multiplied variance-normalised PSD using Welch's method ($f_s = 10$ kHz, $K = 8$ segments) and the interaction length-based Strouhal number.

Standard Deviation Distribution

Standard deviation distributions of the interactions are given in this section to understand the interaction fluctuating dynamics. The definition of the region in which the standard deviation was computed is given in Figure 4.7 which shows the average Schlieren image of the uncontrolled interaction and the region in red. It also includes its spatial standard deviation distribution and annotations of the flow field. The standard deviation is presented in terms of the variation in pixel intensity σ_I, and the spatial coordinates are nondimensionalised by δ_0.

The standard deviation distribution shows the global elements of the oblique SWTBLI in line with the Schlieren images. Multiple lines are observed near the incident, separation, and reflection shock showing that the Schlieren technique captures the corner effects through spanwise integration. This underlines the decision for the incident and reflection shock in the edge-detection algorithm that these are the likely locations of these shocks.

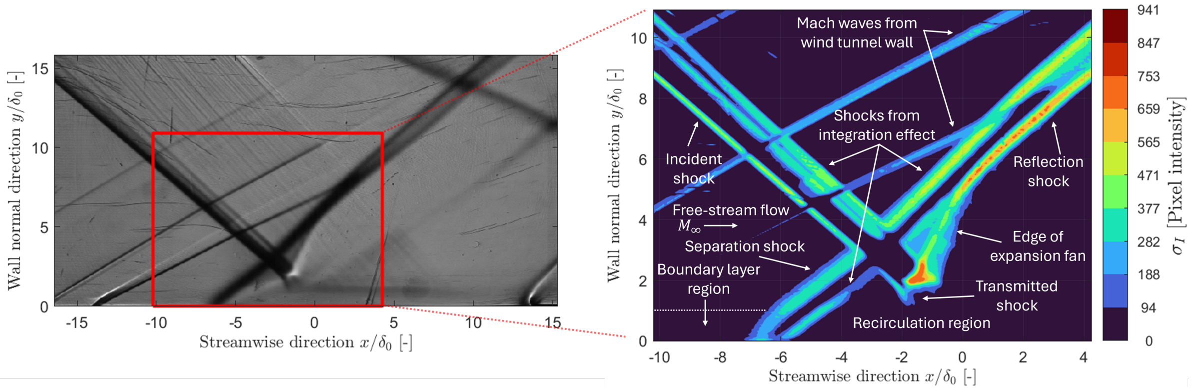

Figure 4.7: Average Schlieren image of the uncontrolled interaction and the used flow field in red for the spatial standard deviation distribution (left), and the distribution including annotations (right).

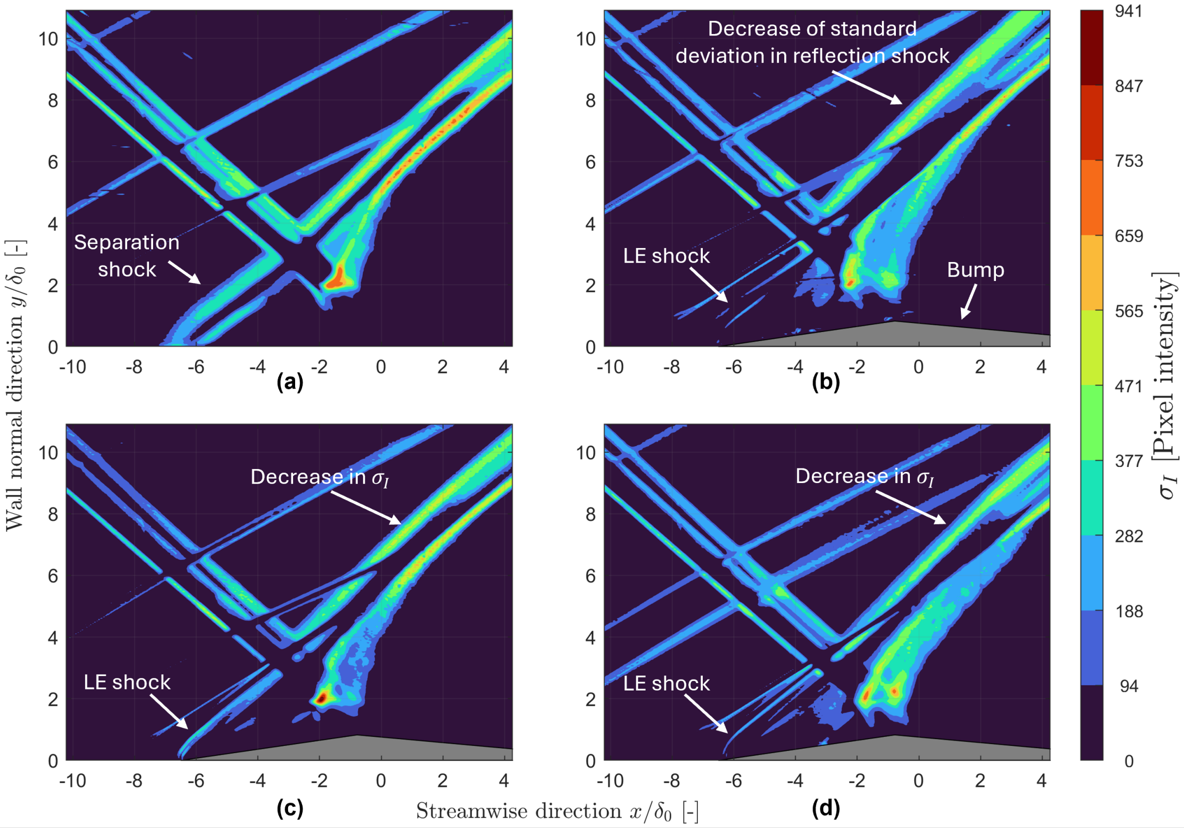

Figure 4.8: Spatial distribution of the standard deviation σ_I for the a) uncontrolled, b) baseline, c) short, and d) smooth bump interaction. Spatial coordinates are normalised by δ_0.

The general features of the oblique SWTBLI can be seen for all interactions in Figure 4.8. The uncontrolled separation shock in Figure 4.8a shows an increase in standard deviation compared to the free-stream flow. Considering Figure 4.8b, it shows that the values in the same region have reduced where the separation shock is replaced by a LE shock. This finding is comparable for the short (Figure 4.8c) and smooth (4.8d) bump in the same region.

In all interactions, there is an appreciable increase in standard deviation in the incident shock. This aligns with the calculations of the edge-detection algorithm which computed an impinging shock standard deviation of $\sigma_{inc}/\delta_0 \approx 0.2$. It differs from expectations since the impinging shock should be steady (i.e. relatively low values of σ_I). Thus, it seems that a form of noise, as established in the previous section, affects the images. Dust on lenses or the camera sensor, environmental contributions, or digital cameras influence the image noise (Nazari et al., 2020), and the latter can be a probable cause. Noise in digital cameras can originate from both illumination-dependent and independent sources (Irie et al., 2009), and the main contributors include:

1. The exposure time or ISO sensitivity (illumination dependent). In general, when the exposure time reduces the signal-to-noise ratio (SNR) of the image signal reduces (Lim, 2006). The SNR is the ratio between the signal power and the noise power in that signal, and a value close to one indicates that a noise signal with a similar power is superimposed on the main signal;
2. Pixel density or resolution (illumination independent). For a higher pixel density on the sensor, the individual pixel captures less light translating to an increase in SNR of the signal (Lim, 2006). This is similar to reduced exposure times; and
3. Temperature (illumination independent). General Complementary Metal-Oxide Semiconductor (CMOS) sensors show an increase in signal noise as the temperature increases (Irie et al., 2009). The cameras during the experimental campaigns have a CMOS sensor (Photron, n.d.-a, n.d.-b).

The size of a pixel in terms of boundary layers is $\Delta x_{pixel} = 0.21$ mm $= 0.04\delta_0$. Comparing this to the standard deviation of the impinging shock, it is probable that the noise does not originate from the pixel density since the fluctuation is five times larger than the pixel size. The temperature in the laboratory did not change considerably, so this seems an unlikely contribution to the noise. It could be, however, that the heat from the camera itself induced a temperature increase since the camera was activated for significant periods during the experiments. Thus, ISO sensitivity is an important factor for the noise in the images.

Temporal correlation distributions of the Schlieren images can aid in identifying the source of the noise. When two Schlieren frames are considered, each a certain time step Δt apart, they will have differing pixel intensity distributions. The two frames can be correlated through time by defining the temporal correlation function. This function, given in Equation 4.1, depends on the spatial location in the image and the considered time step between instantaneous frames. In this equation, I' is the fluctuating pixel intensity and σ_I^2 is the variance of the pixel intensity of the Schlieren frames between time t and $t + \Delta t$. This distribution allows for the characterisation of temporal dynamics in the interaction in terms of time scales of the flow.

$$R(x_{i,j}, t) = \frac{\overline{I'(x_{i,j}, t) I'(x_{i,j}, t + \Delta t)}}{\sigma_I^2}. \tag{4.1}$$

Souverein et al. (2009) and van Oudheusden et al. (2011) applied this technique to PIV data which can also be applied to the Schlieren frames using the pixel intensity fluctuations rather than the velocity fluctuations. Souverein et al. (2009) performed the temporal correlation for a relatively short time step of an uncontrolled oblique SWTBLI and observed high correlation values in the incident shock of the interaction. They identified it as noise or the measurement uncertainty of the PIV technique. A similar analysis was performed for the Schlieren images during this experiment. Consider Figure 4.9 which shows the temporal correlation distribution for the uncontrolled interaction at $\Delta t = 100\mu s, 400\mu s$, and $900\mu s$. The correlation is close to zero everywhere in the flow field for a time step of $\Delta t = 100\mu s$. This indicates that no regions in the flow field have an appreciable correlating time scale. This process was repeated for all interactions, but it produced similar results. In other words, the Schlieren images are attributed to significant noise levels and the correlation through time of the pixel intensities might not be a suitable method using Schlieren data.

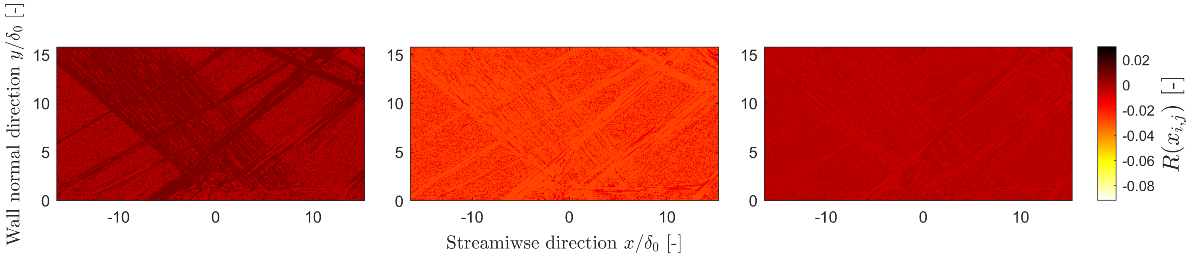

Figure 4.9: Temporal correlation distribution based on the Schlieren frames of the uncontrolled interaction. Correlations are for time steps of: left) $100\mu s$, middle) $400\mu s$, and right) $900\mu s$ ($f_s = 10$ kHz). Coordinates are normalised by δ_0.

To investigate the noise, different settings of resolution or exposure time can be applied. The edge-detection can also be improved by applying different noise mitigation methods discussed in subsection 4.3.2. The algorithm assumes that the noise is distributed as Additive White Gaussian Noise (AWGN) and applies Gaussian filtering during the edge-detection. This assumption is not valid since images by digital cameras have an anisotropic noise distribution (Lim, 2006). The effect of Gaussian filtering on the edge-detection results is explored in subsection 4.3.2. Other methods can also be deployed as developed by Bulut et al. (2022) where the location of the shock is based on the unfiltered pixel intensity while applying thresholding to mitigate noise. A final option could be to revert to a different experimental technique and investigate the performance of the edge-detection algorithm.

Spectral Analysis

The results of the spectral analysis are plotted in Figure 4.10. Each interaction consists of the defined spectral box in the average Schlieren image and the pre-multiplied variance-normalised PSD distribution. The PSDs are plotted in the normalised streamwise direction for the frequency and Strouhal number. The free-stream velocity from subsection 3.1.1 and the mean interaction length of the uncontrolled interaction in Table 4.1 are used to compute the Strouhal number.

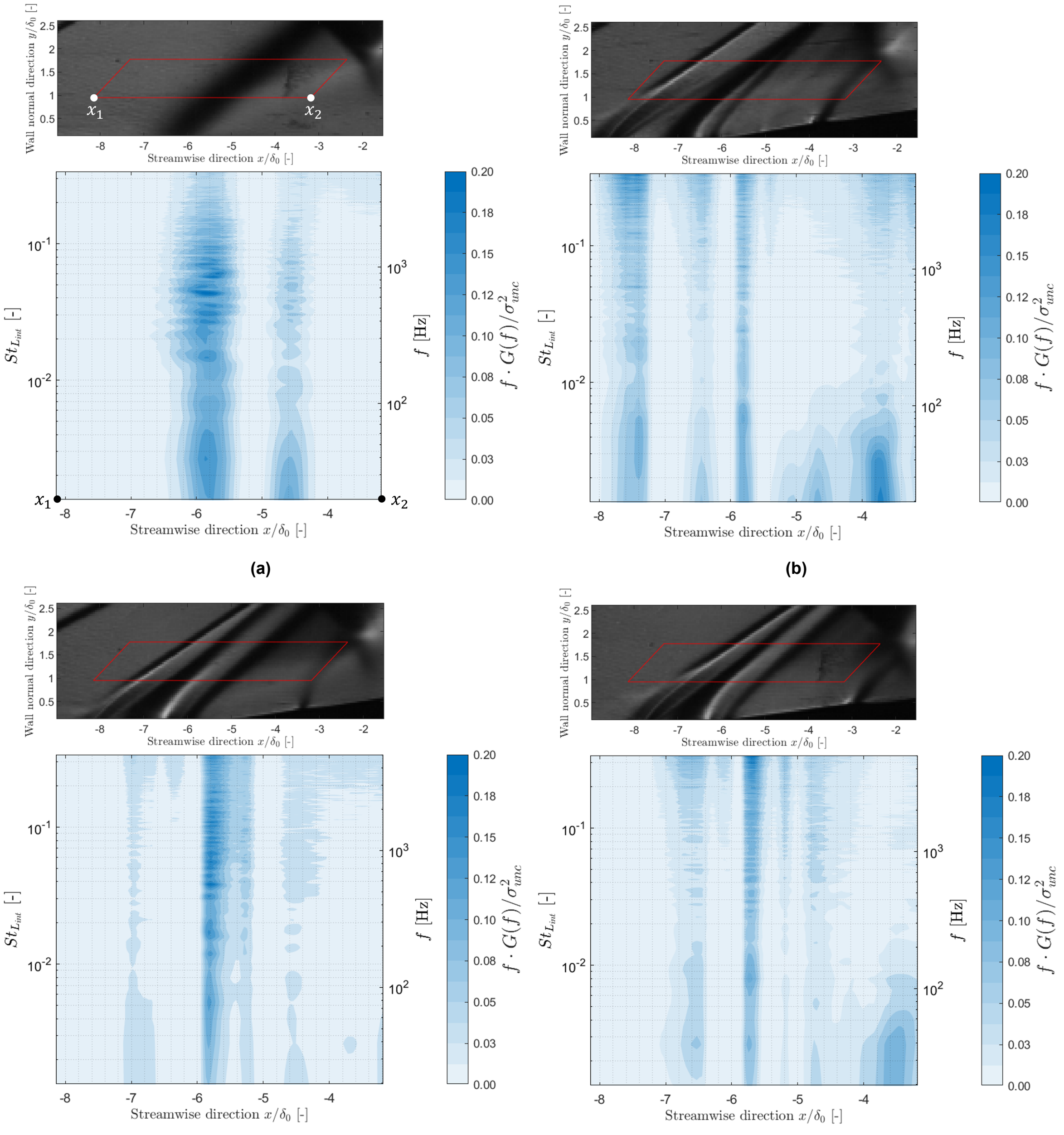

(a) (b)

(c) (d)

Figure 4.10: Pre-multiplied variance-normalised PSD (arbitrary scale, $L = 512$, $f_s = 10$ kHz) distribution of the associated spectral boxes for the a) uncontrolled, b) baseline, c) short, and d) smooth bump interaction. The distribution is plotted in the normalised (δ_0) streamwise direction against the frequency and Strouhal number $St_{L_{int}}$.

The variance is computed using Equation 4.2 in which $P(f)$ is the PSD calculated by Welch's method and x_1 and x_2 are the lower left and lower right streamwise coordinate of the spectral box, respectively. These coordinates are visualised in Figure 4.10a. The variance can be seen as the total power of the PSD in the spectral box. As such, the pre-multiplied PSD distribution in terms of power is nondimensionalised by the total power. The distribution then represents the degree of total power associated with the spatial location.

$$\sigma^2 = \int_{x_1}^{x_2} \int_0^f P(f) df dx. \tag{4.2}$$

The uncontrolled interaction in Figure 4.10a shows peaks of spectral content in the range of $St_{L_{int}} = 0.02 - 0.09$ as well as very low frequency content around $St_{L_{int}} = 0.002 - 0.003$ ($f \approx 50$ Hz). Furthermore, two regions of spectral content are observed rather than one, and the spatial excursion of the content around $x/\delta_0 = -6.0$ is of the order of δ_0. It is suspected that the downstream content around $x/\delta_0 = -4.6$ is the result of spanwise integration of corner effects by the Schlieren technique. The spectral contributions for the baseline interaction in Figure 4.10b appears largely removed for the shock emanating from the bump leading edge around $x/\delta_0 = -6.5$. This also holds for the short and smooth bump interaction in Figure 4.10d and Figure 4.10c, respectively. Additionally, concentrated regions with broadband frequencies are observed in all bump interactions at locations not associated with the leading edge shock. For instance, the short bump spectral analysis shows contributions around $x/\delta_0 = -7.0$ associated with the Mach wave emanating from the tape, and the content between $-6.0 \leq x/\delta_0 \leq -5.0$ can be a result of the corner effects.

The source of the range of spectral content for the uncontrolled interaction is unknown, but it is close the the Strouhal number of $St_{L_{int}} = 0.03$ reported in literature (e.g. Pasquariello et al., 2017; Touber and Sandham, 2009) It is suspected that the spanwise integration effect of the Schlieren technique contributes to this range such that frequencies are captured which are not associated with the centred interaction. This is also hypothesised by Missing et al. (2024) while performing similar experiments. The very low-frequency content observed in almost all interactions is unknown, but this is suspected to be from the Dutch power grid which provides AC electricity at approximately 50 Hz.

On the other hand, a recent study by Laguarda et al. (2024) found similar broadband frequencies of the uncontrolled interaction for a separation length-based Strouhal number of $0.01 \leq St_{L_{sep}} \leq 0.1$. They analysed an impinging SWTBLI using LES for a Mach 2 flow while varying the Reynolds number. They analysed a case for $Re_{\delta_0} = 331.0 \cdot 10^3$ (relatively close to $Re_{\delta_0} = 219.4 \cdot 10^3$ for this experiment), and a spatial variation of the separation shock of approximately δ_0 was observed comparable to the spatial variation obtained here. Furthermore, Laguarda et al. (2024) stated that the broadband frequency could be associated with the expansion and contraction of the recirculation region and the flapping motion of the shear layer. This could provide a possible reason for the range and origin of the low-frequency content in these results.

4.1.2. Variance of Impingement Location

The sensitivity of the 2D-SCB to the changes in impingement location (i.e. robustness) has been investigated, and the results are presented in this section. Measurements were performed for the baseline bump and an upstream and downstream impingement compared to the on-design location (i.e. on the bump crest) of the incident shock.

Schlieren and Oil Flow Visualisation

The average Schlieren images are visualised in Figure 4.11 with Figure 4.11a the $x = -\delta_0$ upstream impingement and Figure 4.11b the $x = \delta_0$ downstream impingement. The downstream impingement is comparable to the Schlieren of the on-design baseline interaction while the upstream impingement shows a region of low-intensity upstream of the bump leading edge. Furthermore, it seems that a shadow region is generated near the boundary layer edge. It suggests that light from the Schlieren setup traverses the test section at an angle rather than fully parallel, and it influences how the density gradients are captured by the camera. It can, therefore, affect the edge-detection results. These measurements were performed at a later stage during campaign A, so an alteration in the experimental setup could cause this effect. An attempt was made to remedy this by altering the Schlieren setup, but it could not be resolved. Nevertheless, the effect on the shock regions is considered small such that it will not affect the edge-detection calculations.

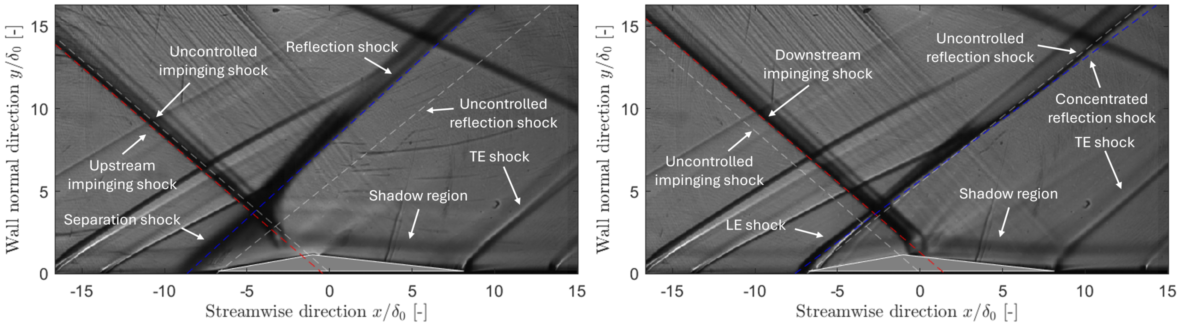

(a) (b)

Figure 4.11: Average Schlieren images of the a) upstream and b) downstream impingement of the incident shock. Bumps are visualised in grey, and the incident (red), reflection (blue), and uncontrolled incident and reflection shock (grey) are included as dashed lines.

For the upstream impingement oil flow in Figure 4.12a, separating and recirculation flow is seen upstream of the bump which terminates at the leading edge. This corroborates with the Schlieren image and confirms separation shock formation. The streamlines seem to deflect towards the lower wind tunnel wall on the bump ramp which can be the result of the shock generator misalignment as discussed in subsection 4.1.1. The upstream dimple effect can be seen again and is not considered to influence the main interaction. For the downstream impingement in Figure 4.12b, recirculation regions are generated downstream of the bump crest near the wind tunnel side walls rather than the centred interaction. Similar recirculating behaviour was observed by Bulut et al. (2022) for a supersonic flow with a 3D-SCB. Furthermore, Ogawa and Babinsky (2008) and Ogawa et al. (2008) tested 3D-SCBs during transonic and supersonic conditions for normal shock waves and also found recirculating flow downstream of the bump crest when the shock impinges downstream compared to the on-design case. These investigations, however, did not argue on the unsteadiness related to the shock system. Note that these findings are for different bump shapes, flow conditions, and shock geometries, but they show a general trend.

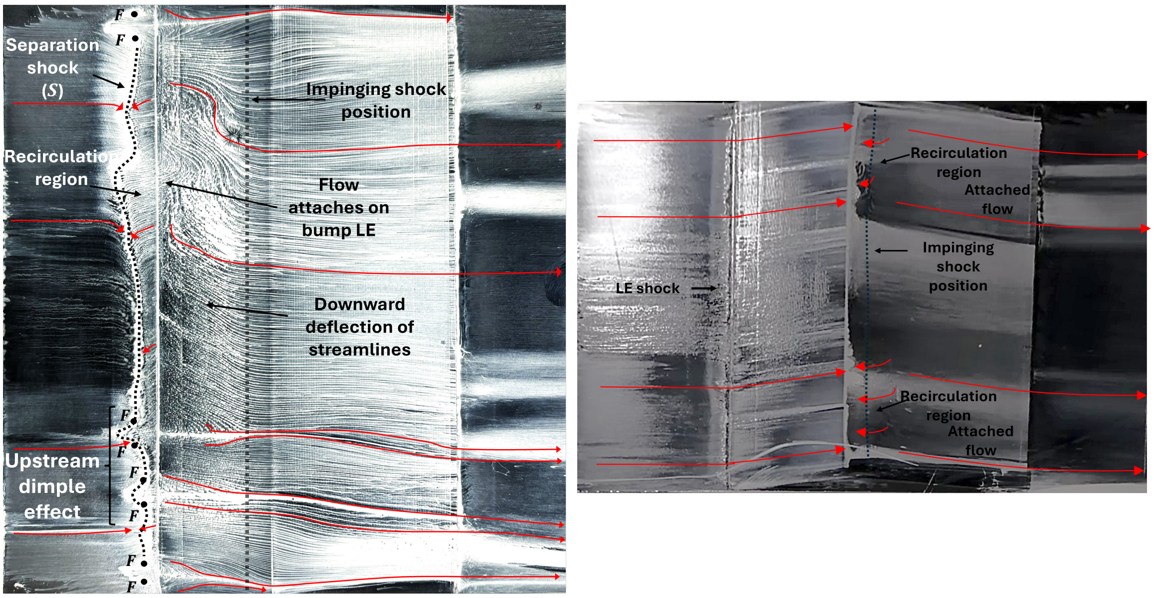

(a) (b)

Figure 4.12: Oil flow visualisation of the a) upstream and b) downstream impingement case. Streamlines are shown in red with critical point theory and annotations. Focal points (***F***) are simplified as black dots.

Impingement and Separation Locations of the Edge-Detection Algorithm

The histograms of the edge-detection algorithm are presented in Figure 4.13. These histograms are given in the nondimensional streamwise direction and the number of occurrences. The black square indicates the bump leading edge. The upstream impingement is centred around $x/\delta_0 \approx -0.2$ whereas the downstream impingement is around $x/\delta_0 \approx 1.68$. This does not coincide with the intended impingement of $-\delta_0$ and δ_0, respectively. This can also be seen visually in the average Schlieren images. An alteration in the Schlieren setup likely caused a shift in the origin of the axis system of approximately $0.7\delta_0$. The alteration in setup was also observed by the creation of a shadow region in the Schlieren images. This shift would only affect the edge-detection results by shifting the results with $\approx +0.7\delta_0$ and not the variation of the results.

The separation histograms show that the downstream impingement in Figure 4.13d has a comparatively larger spread around the mean of $x/\delta_0 \approx -7.0$. The upstream separation location seems relatively concentrated. This behaviour contradicts the observed interaction dynamics of the Schlieren and oil flow visualisations. It again shows the deviation between the Schlieren and oil flows and the calculations of the edge-detection algorithm. Finally, a quantification of the histograms is given in Table 4.2 including the uncontrolled and baseline interaction.

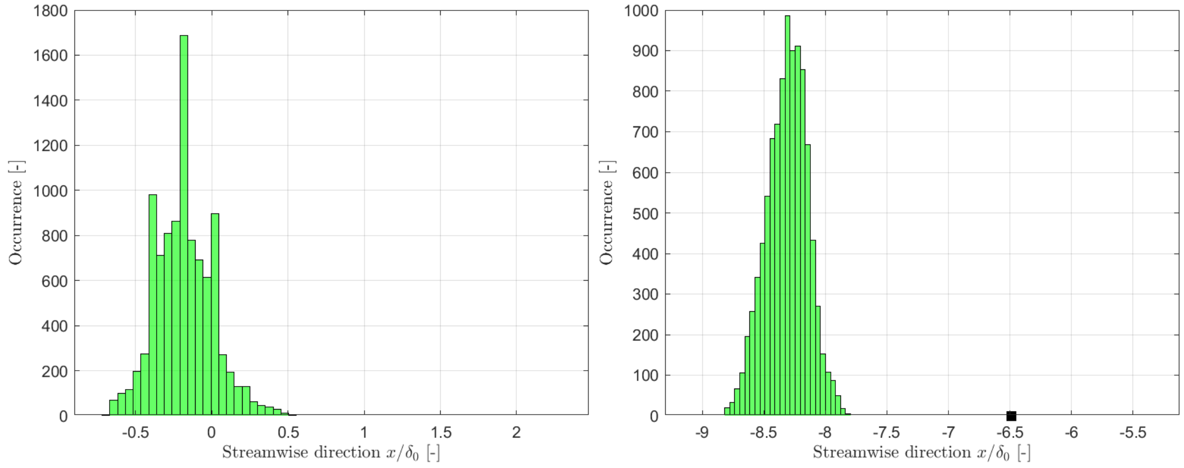

(a) Impingement location.

(b) Separation location.

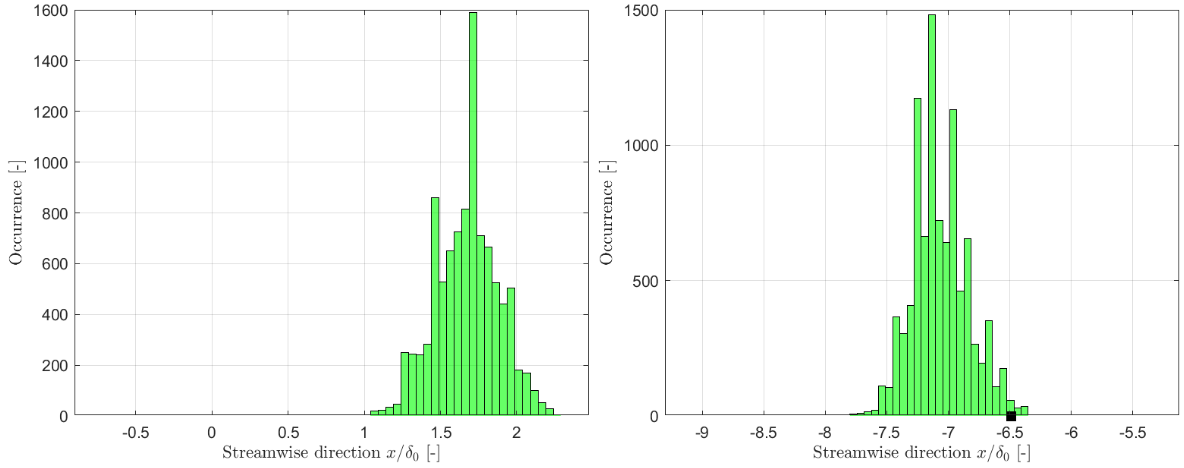

(c) Impingement location.

(d) Separation location.

Figure 4.13: Histogram data of the impingement and separation shock wave using the shock detection algorithm for an upstream (a-b) and downstream (c-d) impingement on the baseline bump (bins = 25, 3σ-method applied). Black squares indicate the bump leading edge.

Table 4.2: Quantification of the mean impingement and separation location $(\bar{x}/\delta_0)$ [-] per interaction case (upstream/downstream) including the leading edge of the bumps, the standard deviation σ/δ_0 [-], mean interaction length $\bar{L}_{int}/\delta_0$ [-] and uncertainties ϵ [m]. The uncontrolled and baseline interactions are included for comparison.

Cases	$(\bar{x}/\delta_0)_{sep}$	$(\bar{x}/\delta_0)_{LE,bump}$	$(\bar{x}/\delta_0)_{inc}$	σ_{sep}/δ_0	σ_{inc}/δ_0	$\bar{L}_{int}$	ϵ_{sep}	ϵ_{inc}
Uncontrolled	-6.77	-	-0.013	0.28	0.21	6.76	$1.48 \cdot 10^{-4}$	$1.10 \cdot 10^{-4}$
Baseline	-6.74	-6.49	0.062	0.17	0.21	6.80	$9.01 \cdot 10^{-5}$	$1.10 \cdot 10^{-5}$
Upstream	-8.31	-6.49	-0.18	0.17	0.19	8.13	$8.91 \cdot 10^{-5}$	$9.92 \cdot 10^{-5}$
Downstream	-7.06	-6.49	1.68	0.24	0.20	8.69	$1.27 \cdot 10^{-4}$	$1.07 \cdot 10^{-4}$

Standard Deviation Distribution and Spectral Analysis

The standard deviation distributions for the upstream and downstream impingement are given in Figure 4.14. The distributions are given in nondimensional spatial coordinates and the standard deviation is σ_I. The same annotations apply here as given in Figure 4.7. The downstream case shows no appreciable increase in σ_I of the bump LE shock. This is not the case for the upstream impingement where a relatively large region shows increased deviation values. This supports the findings that a separation shock with recirculating flow is generated in this region. Finally, multiple lines near the shocks again show the integration of the corner effects, and the incident shock contains a relative increase in deviation values. This highlights the noise levels in the Schlieren images as discussed in subsection 4.1.1.

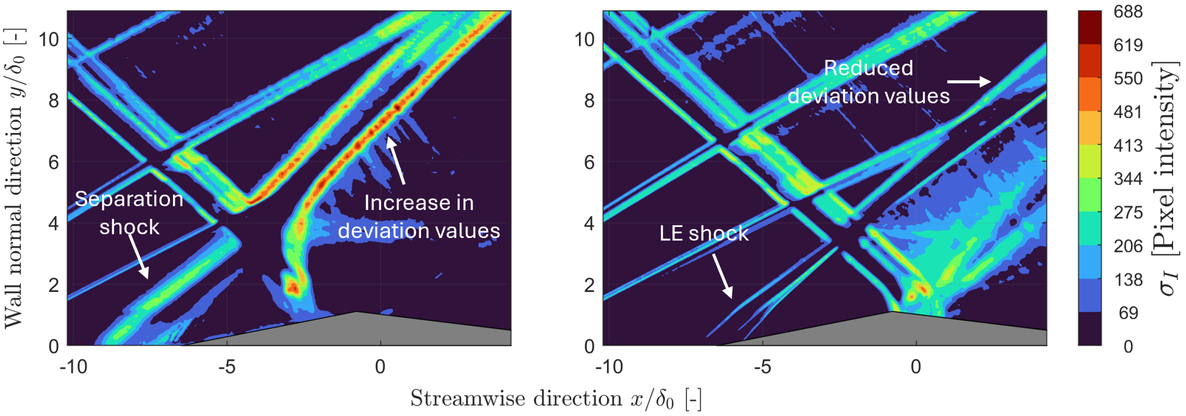

Figure 4.14: Spatial standard deviation distribution for a) upstream and b) downstream impingement location. The spatial coordinates are normalised by δ_0 and the standard deviation is given as pixel intensity variation σ_I.

The spectral analysis for the upstream and downstream impingement is given in Figure 4.15. It shows the pre-multiplied variance-normalised PSD distribution of the spectral box in the spanwise direction in terms of Strouhal number and frequency. The characteristic low-frequency content of the uncontrolled interaction ($0.02 \leq St_{L_{int}} \leq 0.09$) seems to be removed for the downstream impingement. The upstream impingement shows an increase in the content similar to the uncontrolled separation shock in Figure 4.10a. The spatial excursion of around δ_0 is also similar to the findings of the uncontrolled interaction.

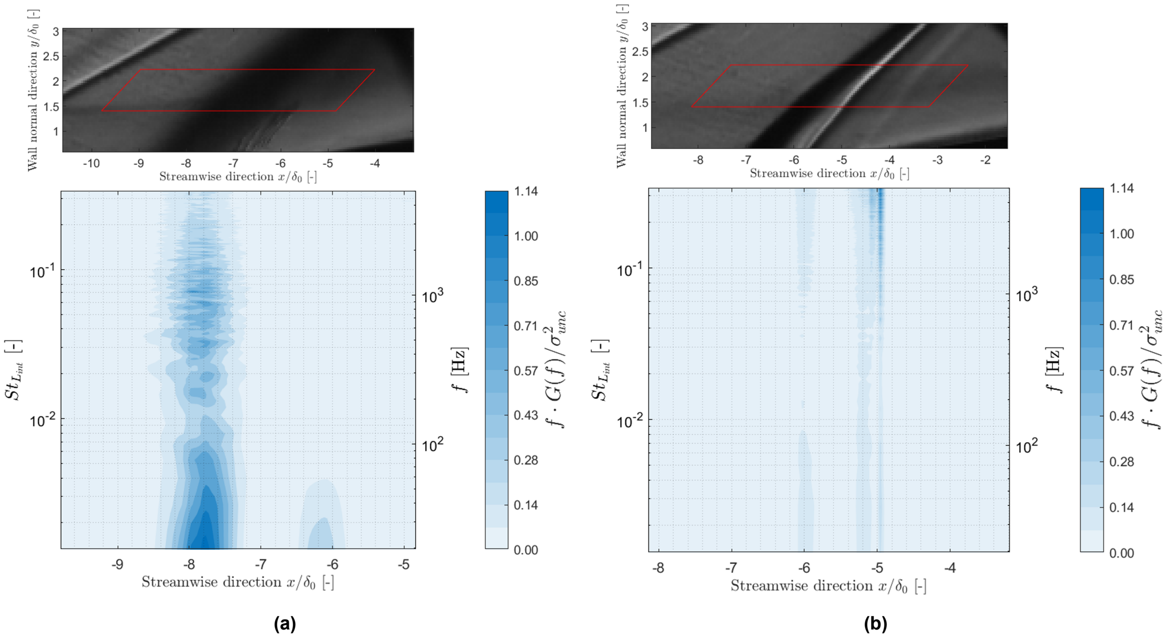

Figure 4.15: Pre-multiplied variance-normalised PSD distribution (arbitrary scale, $L = 512, f_s = 10$ kHz) for a) upstream and b) downstream impingement location on the baseline bump. The distributions are given in terms of the normalised streamwise direction, Strouhal number, and frequency. The spectral boxes from the Schlieren images are included as visual references.

In view of unsteadiness, the downstream impingement of the incident shock did not show any alteration compared to the baseline on-design interaction. The uncontrolled separation shock is replaced by a steady compression ramp shock originating from the bump leading edge. The small recirculating flow regions downstream of the bump crest did not seem to influence the behaviour of this compression ramp shock. The upstream impingement showed more unsteady behaviour trending towards the unsteadiness of the uncontrolled interaction.

A physical explanation for this behaviour is given in Figure 4.16. It shows a simplified sketch of the wall-pressure distribution associated with the uncontrolled SWTBLI and the shift of this distribution for an upstream and downstream impingement. It also includes a spatial visualisation of this effect on the bump dynamics. First, consider the pressure distribution of the uncontrolled interaction. The baseline bump was designed such that the bump leading edge is at the spatial location of the separation shock; a compression ramp shock replaces the separation shock. Analysis of the results of campaign A showed no signs of a separation bubble for the baseline interaction. As soon as the impinging shock is shifted in the upstream direction (see arrow 1), the associated pressure distribution is shifted accordingly such that the interaction origin becomes $x = x_0 - \delta_0$. This allows for the boundary layer to separate, generate a separation shock, and form a separation bubble (see the orange region annotated by a 1). This bubble is constrained by the presence of the bump leading edge such that, presumably, the separation bubble mechanism cannot excite the characteristic separation behaviour. This trend seems to be confirmed when comparing the uncontrolled, baseline bump, and upstream impingement interaction spectral analysis. It is expected that the separation behaviour becomes increasingly comparable to the uncontrolled interaction when the shock is shifted further upstream. On the other hand, a downstream impingement (see arrow 2) shifts the interaction origin to $x = x_0 + \delta_0$. Now, a compression ramp shock will be generated with recirculating flow (see the orange region annotated by a 2). Hence, no low-frequency unsteadiness comparable to the uncontrolled interaction will be generated in this region. A further downstream impingement could locally generate a local unsteady SWTBLI on the bump crest, but this needs to be investigated further.

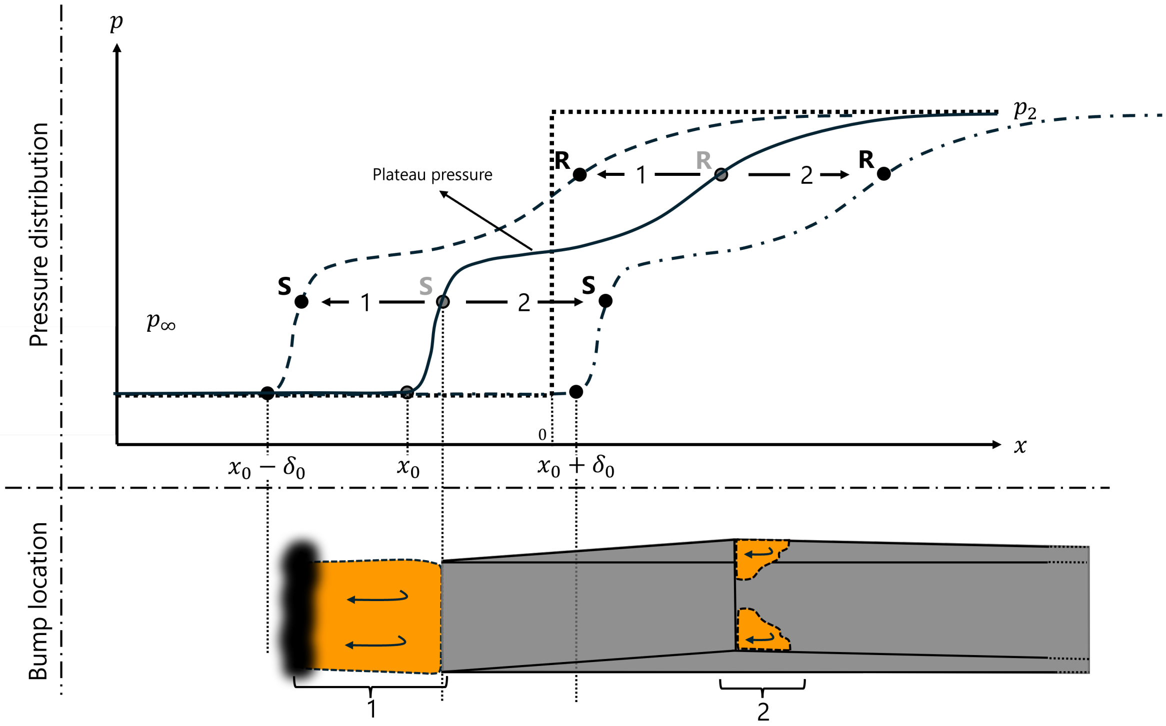

Figure 4.16: Sketch of the (p, x) wall distribution shift for an upstream (1) and downstream (2) impingement on the shock control bump (in grey, not to scale). Pressure distributions include the interaction origins x_0, separation (**S**) and reattachment **R** locations, and the plateau pressures. Lines represent: (··) inviscid solution, (——): upstream, (—) on-design, and (—·) downstream impingement.

To recall, the objective of this research is to investigate the unsteady behaviour of the oblique SWTBLI using 2D-SCBs. Two-dimensional bumps were chosen to obtain a more fundamental understanding of the interaction dynamics. Based on the results of campaign A, the baseline bump with on-design impingement will be used in further experiments to fulfil the research objective. This bump showed the most nominal two-dimensional interaction dynamics of the three designs.

4.2. Results and Discussion of Campaign B

This section discusses the results of experimental campaign B. The campaign investigated the alteration in the ramp and tail angle of the baseline bump. The ramp variation is discussed in subsection 4.2.1, and the tail variation is discussed in subsection 4.2.2.

4.2.1. Variation in Ramp Angle

This section discusses the results of the variance in the ramp angle of the baseline bump. It is divided into the discussion of the Schlieren and oil flows, the impingement and separation location from the edge-detection algorithm, and the spectral analysis.

Schlieren and Oil Flow

The average Schlieren images for the bumps with ramp angle variation are presented in Figure 4.17. These plots include annotations and are given in nondimensional distances, the bumps in grey, the impingement (red dashed line), and the reflection (blue dashed line) shock line. Furthermore, it includes the uncontrolled reflection shock (grey dashed line) for comparison. The origin again represents the inviscid impingement location of the uncontrolled incident shock. The bumps without shock generator are given in Appendix A.

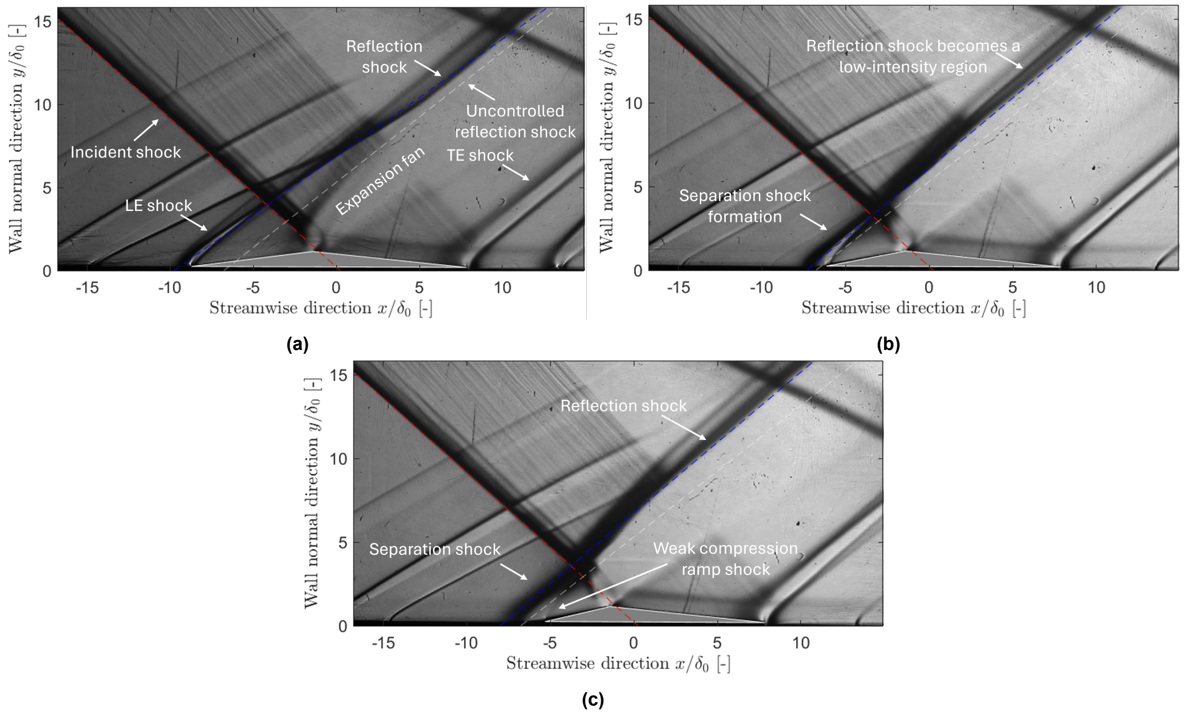

(a)

(b)

(c)

Figure 4.17: Average Schlieren images of bump ramp angle variation for: a) SCBr7t5.5, b) SCBr11t5.5, and c) SCBr13t5.5. Images include dashed lines for the incident (red), reflection (blue), and uncontrolled reflection (grey) shock.

The average Schlieren images show the typical structure of the SWTBLI. No tape was used during campaign B to smoothen the transition between the flat plate and the bumps. The expansion fan on the crest changes shape as the angle increases, and the tail part appears to remain unaltered. As the ramp angle increases, the distinct shock from the bump leading edge for SCBr7t5.5 (Figure 4.17a) changes to a broader region of low-intensity for SCBr13t5.5 (Figure 4.17c). A weak shock from the bump leading edge is also present in this case. The oil flows in Figure 4.18 corroborate these observations. The flow largely remains attached to the bumps, and as the ramp angle increases, a recirculation region is generated upstream of the bump leading edge. The flow shows spanwise symmetrical behaviour on each bump indicating that the shock generator misalignment caused the downward deflection of the skin friction lines on the bumps (see section 4.1). Finally, the effect of the upstream dimples as discussed in subsection 4.1.1 is observed which is considered to have minimal influence on the main interaction.

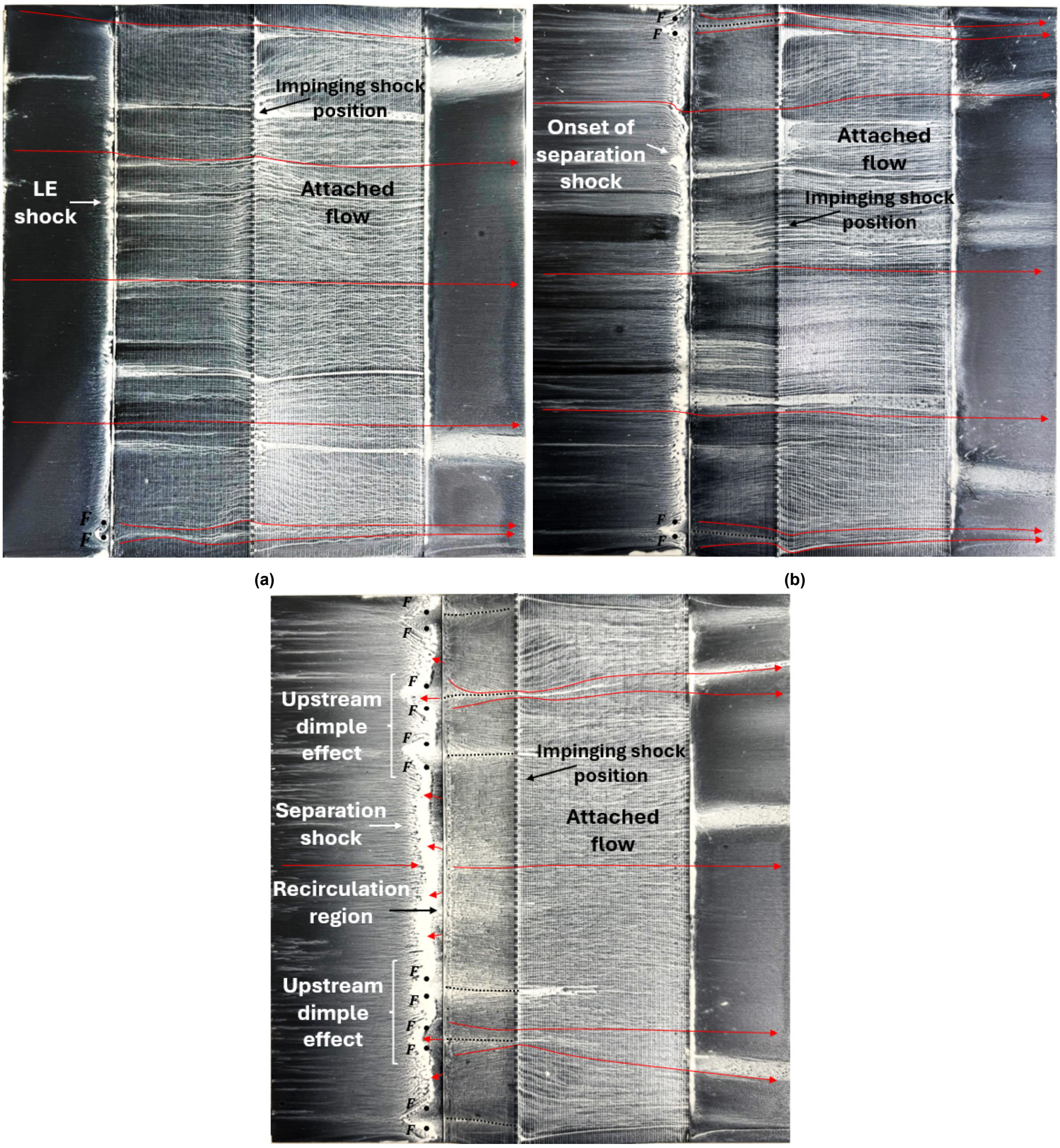

(a)

(b)

(c)

Figure 4.18: Oil flow for bump ramp angle variation for: a) SCBr7t5.5, b) SCBr11t5.5, and c) SCBr13t5.5. Images include annotations, streamlines (red) and critical point theory (black). The streamlines associated with the focal points are simplified as dots (***F***).

Impingement and Separation Locations from Edge-Detection Algorithm

The results of the edge-detection algorithm are tabulated in Table 4.3. For comparison, the data of the uncontrolled and baseline interactions are repeated. As discussed in section 4.1, the Schlieren images were subjected to noise levels that supposedly influenced the impingement and separation location calculations. Despite the efforts to mitigate this noise, the results were inconclusive regarding the unsteady behaviour of the reflection shock or separation location. Improving the noise mitigation method would be beneficial, or a different method needs to be applied to calculate the locations. Finally, the performance of the edge-detection algorithm is explored in subsection 4.3.2.

Table 4.3: Quantification of impingement and separation location $(\bar{x}/\delta_0)$ [-] per interaction case (ramp variation) including the leading edge of the bumps, the standard deviation σ/δ_0 [-], mean interaction length $\bar{L}_{int}/\delta_0$ [-] and uncertainties ϵ [m]. The uncontrolled and baseline interactions are included for comparison.

Cases	$(\bar{x}/\delta_0)_{sep}$	$(\bar{x}/\delta_0)_{LE,bump}$	$(\bar{x}/\delta_0)_{inc}$	σ_{sep}/δ_0	σ_{inc}/δ_0	$\bar{L}_{int}$	ϵ_{sep}	ϵ_{inc}
Uncontrolled	-6.77	-	-0.013	0.28	0.21	6.76	1.48$\cdot 10^{-4}$	1.10$\cdot 10^{-4}$
SCBr7t5.5	-9.22	-8.70	-0.172	0.13	0.21	9.05	3.41$\cdot 10^{-5}$	5.15$\cdot 10^{-5}$
Baseline (SCBr9t5.5)	-6.74	-6.49	0.062	0.17	0.21	6.80	9.01$\cdot 10^{-5}$	1.10$\cdot 10^{-5}$
SCBr11t5.5	-7.12	-6.13	0.029	0.23	0.21	7.15	5.62$\cdot 10^{-5}$	5.24$\cdot 10^{-5}$
SCBr13t5.5	-7.74	-5.30	-0.046	0.20	0.21	7.69	4.93$\cdot 10^{-5}$	5.14$\cdot 10^{-5}$

Standard Deviation Distribution and Spectral Analysis

Spatial standard deviation distributions of the bump ramp angle variation are given in Figure 4.19. This is presented in terms of σ_I, and the spatial dimensions are normalised by δ_0. Notably, the standard deviation values increase from the SCBr7t5.5 case to the SCBr13t5.5 case in the separation and reflection shock regions. This supports the separation shock formation in the Schlieren and oil flows. The increase in values of the reflection shock was also seen in the uncontrolled standard deviation distribution.

The standard deviation values of the impingement location tabulated in Table 4.3 are similar to the deviation values in section 4.1. This indicates that the unexpected variation originates from the calculation methods within the algorithm since different cameras were used for campaigns A and B. However, the spatial standard deviation distributions still show increased values in the incident shock region even though the values have reduced significantly compared to the values of the same region in section 4.1. This combination shows that, despite a camera change and reduction in deviation values, identical fluctuations are obtained by the algorithm. Hence, the imposed noise by the camera and the mitigation method by the algorithm most likely influence the edge-detection results.

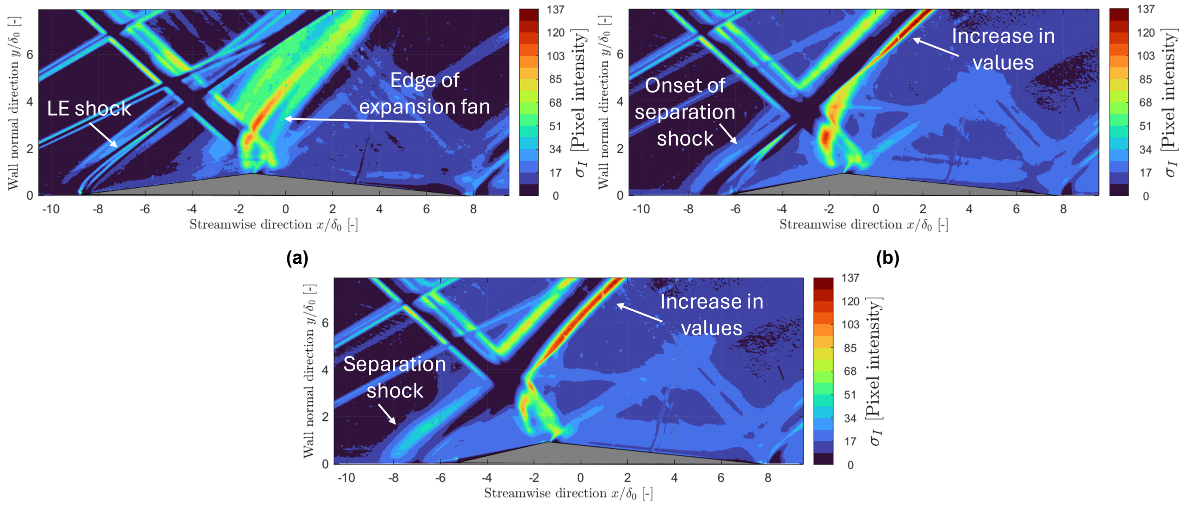

(a)

(b)

(c)

Figure 4.19: Spatial standard deviation distributions for the bump ramp angle variation for: a) SCBr7t5.5, b) SCBr11t5.5, and c) SCBr13t5.5. Spatial coordinates are nondimensionalised by δ_0, and the standard deviation is in terms of pixel intensity.

The spectral analysis for the bump ramp angle variation is given in Figure 4.20 including the baseline and uncontrolled interaction. The plot contains Schlieren images of the spectral boxes used to compute the pre-multiplied variance-normalised PSDs. A section within the box is selected by the red dashed lines and is displayed in the spectral distribution. The same plot in terms of frequency is given in Appendix B. The uncontrolled interaction shows the range of Strouhal numbers between $0.02 \leq St_{L_{int}} \leq 0.09$. Considering the ramp variation, it appears that this spectral content has largely been removed. However, significant contributions are obtained at Strouhal numbers below 0.01 for the SCBr13t5.5 case and only slight contributions in the aforementioned Strouhal region. The low values are suspected to result from the alternating current provided to the light source from the Dutch power grid which is approximately 50 Hz. The spatial excursion of the peaks is of the order of δ_0 which is comparable to the uncontrolled interaction and findings by Laguarda et al. (2024).

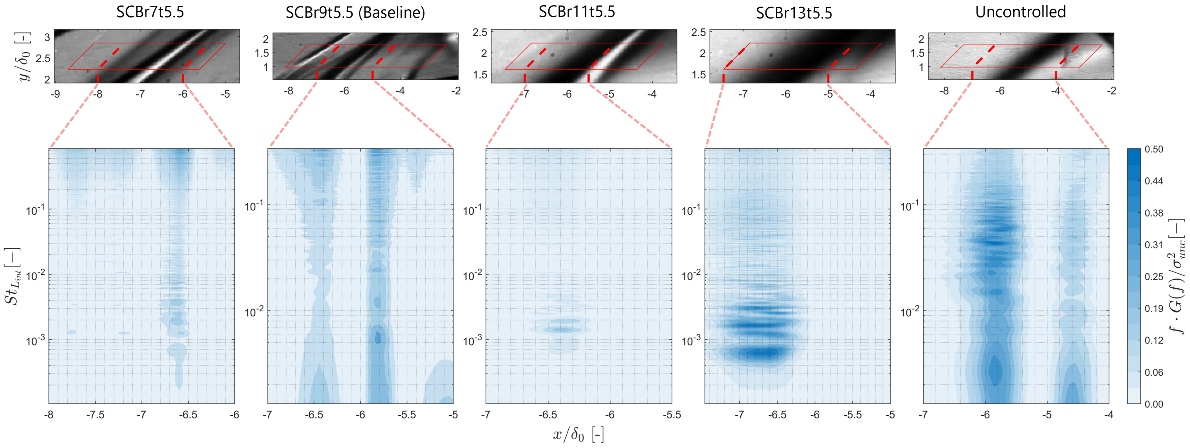

Figure 4.20: Pre-multiplied variance-normalised PSD distribution ($K = 8$ segments, $f_s = 25$ kHz) of the bumps with ramp angle variation including the definition of the spectral boxes. The baseline and uncontrolled interaction are included as reference ($f_s = 10$ kHz, $L = 512$). Distributions are in terms of the nondimensional frequency $St_{L_{int}}$ and x/δ_0.

A general trend is observed for an increase in ramp angle where the unsteady behaviour of the shock near the bump leading edge seems to amplify. For the SCBr13t5.5 case, a distinct recirculation region is generated upstream of the leading edge which seems to stabilise when the flow traverses on the ramp again. The spatial standard deviation distribution supports this behaviour in terms of increased deviation values near the bump leading edge. However, the spectral analysis shows that none of the characteristic frequencies of the uncontrolled separation shock are obtained.

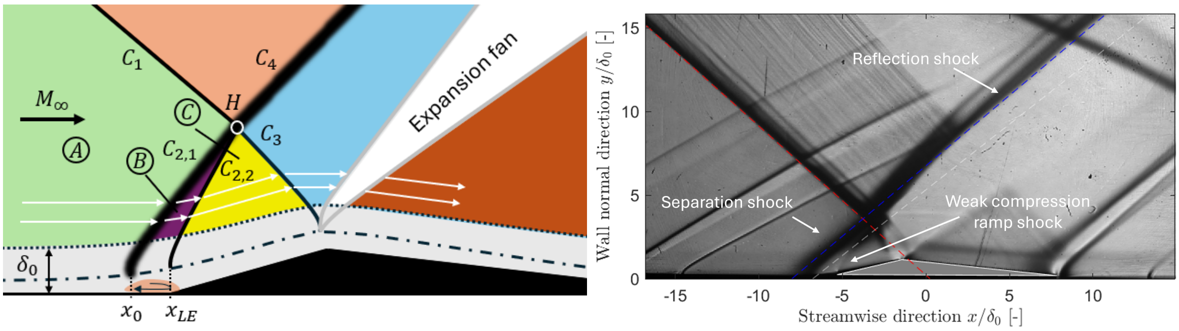

(a) (b)

Figure 4.21: Left: a simplified sketch of the 2D flow dynamics for the SCBr13t5.5 including the boundary layer (··), recirculation region (orange, $- \cdot -$), streamlines (white), annotated flow region, and shock waves. Right: Average Schlieren image of the SCBr13t5.5 including annotations, incident (red), reflection (blue), and uncontrolled reflection (grey) dashed lines. Coordinates are normalised by δ_0.

The dynamics due to an increase in ramp angle can be thought of in the following way. Consider Figure 4.21a which shows a simplified sketch of the SCBr13t5.5 interaction in Figure 4.21b. Various regions are distinguished by colour, and shock waves and regions are annotated by a letter. First, the pressure gradient of the incident shock (C_1) induces flow separation on the boundary layer in region (A). When the streamlines in region (A) traverse to region (B) through the separation shock ($C_{2,1}$), they are deflected by an angle $\phi_B \approx 9.0°$ (as determined in subsection 3.2.1). The separated boundary layer generates a separation bubble starting near the interaction origin x_0. The flow then approaches the bump leading edge x_{LE} from which a compression ramp shock ($C_{2,2}$) emanates. It is speculated that a compression ramp shock is generated here since there is a difference in the angle between the bump ramp and the flow direction in region (B). This is confirmed by the Schlieren image of the SCBr13t5.5.

Based on the oil flow, the separation bubble is terminated at the bump leading edge. The streamlines continue with $\phi_C \approx 13°$ in region (C) to the transmitted shock (C_3). Hence, the separation bubble is restricted by the bump leading edge. If it is assumed that separation bubble breathing is at the origin of low-frequency unsteadiness, then it can be hypothesised that breathing and flapping of the shear layer cannot develop to its true potential due to the constraining of the separation bubble size.

It can also be hypothesised that a local SWTBLI is generated near the bump leading edge in addition to the 'global' SWTBLI. However, the average Schlieren image of the same bump without an impinging shock in Appendix A shows no similar low-intensity region near the bump leading edge. A spectral analysis is performed of the SCBr13t5.5 without shock generator and is given in Figure 4.22. This figure shows the spectral box in the average Schlieren image and the pre-multiplied variance-normalised PSD distribution in terms of Strouhal number, frequency, and normalised spatial coordinates. Two primary regions are observed: one between $-6.0 \leq x/\delta_0 \leq -5.5$ and the other around $x/\delta_0 = -4.75$. Hence, it appears that a shock is generated upstream of the bump leading edge and a weak shock is generated at this leading edge. This could depict the generation of an incipient SWTBLI. The spectral analysis shows that the weak LE shock only has relatively high Strouhal number contributions and the other shock has a broader range of Strouhal numbers. It does not have the characteristic low-frequency contributions of the uncontrolled separation shock, so drawing a conclusion based on these results is challenging. Comparing this to the spectral analysis of the SCBr13t5.5 with the shock generator, it seems that the impinging shock has a more dominant role in inducing the unsteadiness than the local compression ramp interaction. Further investigation by an oil flow visualisation or other experimental techniques would be beneficial to draw better conclusions.

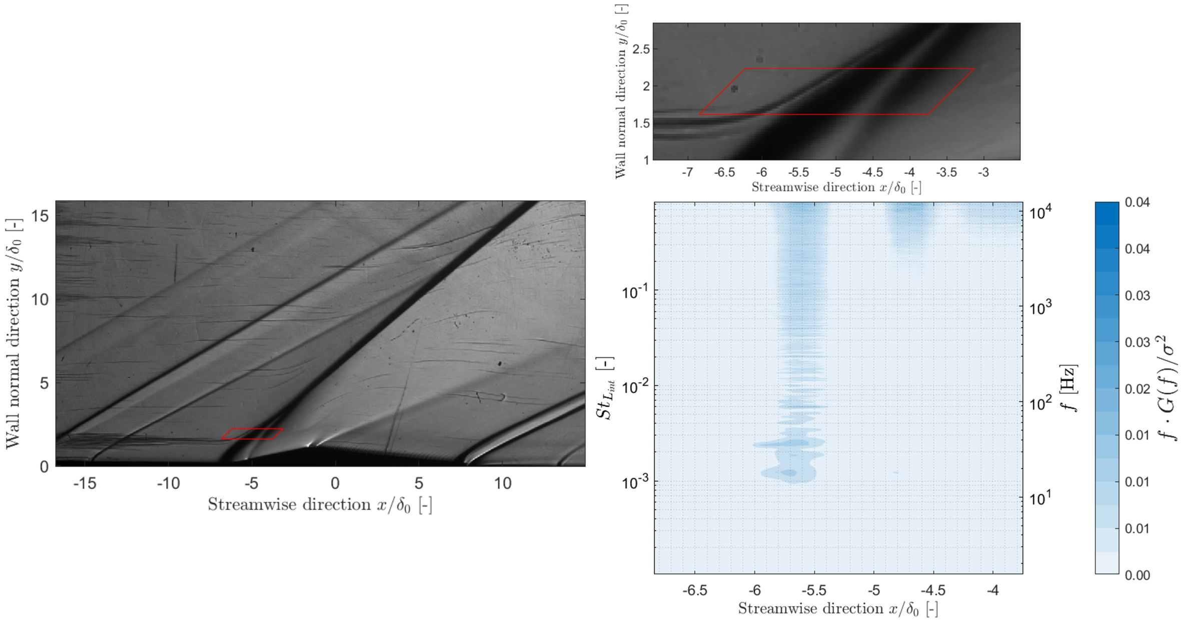

(a) **(b)**

Figure 4.22: Left: average Schlieren image of the SCBr13t5.5 with no SG and the spectral box. Right: the pre-multiplied variance-normalised PSD distribution (arbitrary scale) of the spectral box with the Strouhal number, frequency, and the normalised streamwise direction ($f_s = 25$ kHz, $K = 8$ segments).

4.2.2. Variation in Tail Angle

This section discusses the results of the variance in the tail angle of the baseline bump. It is divided into the discussion of the Schlieren and oil flows, the impingement and separation location from the edge-detection algorithm, and the spectral analysis.

Schlieren and Oil Flow

The average Schlieren images of the tail angle alteration are shown in Figure 4.23. The same Schlieren images without shock generator are given in Appendix A. Consistent observations are made for the ramp part for increasing tail angles; a LE shock is generated similar to the flow dynamics of the baseline bump. Furthermore, the expansion fan appears to be more distinctive for an increase in tail angle. Compression waves are generated at the tail part as the angle increases and these coalesce in a shock. Small variations between the reflection shock line (blue) and the uncontrolled reflection shock line (grey) can be due to the manual misplacement of the bumps on the flat plate. These are considered to have a negligible effect on the comparison between interactions.

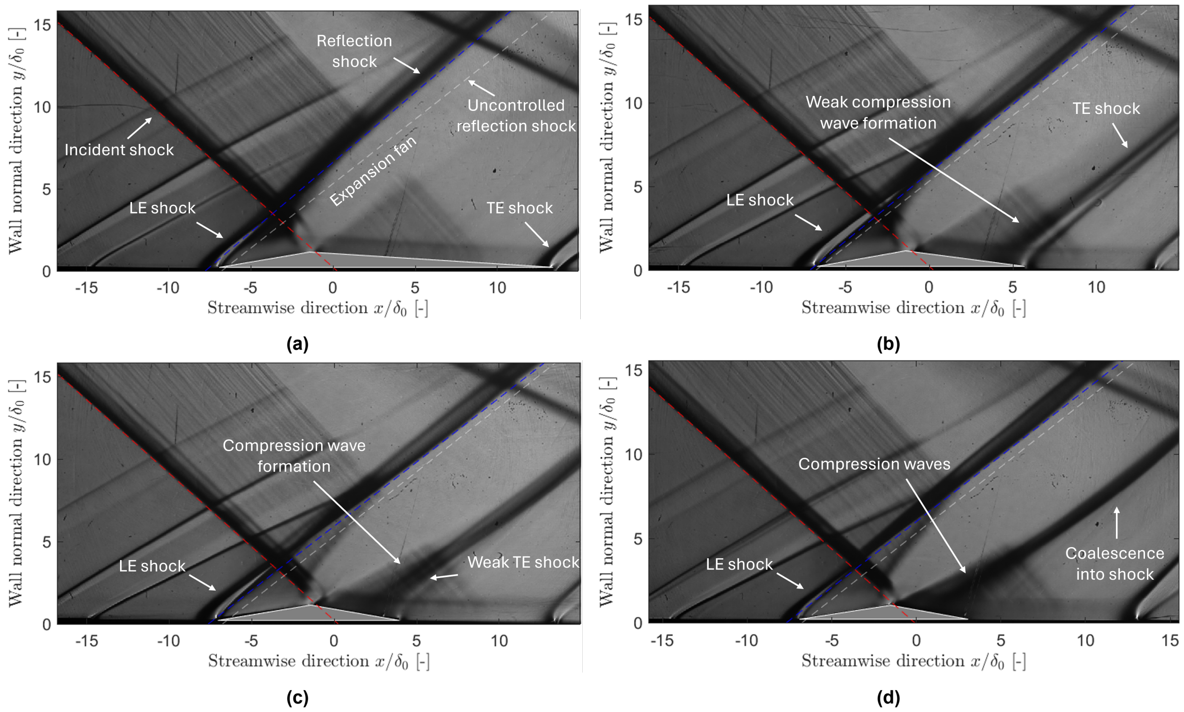

(a) (b) (c) (d)

Figure 4.23: Average Schlieren images of bump tail angle variation for: a) SCBr9t3.5, b) SCBr9t7.5, c) SCBr9t9.5, and d) SCBr9t11. Images include dashed lines for the incident (red), reflection (blue) and uncontrolled reflection shock (grey).

For the oil flows in Figure 4.24, the ramp part of the bump is similar to the oil flow of the baseline bump. In all cases, the flow remains attached to the ramp part of the bump, and the tail part shows a progressive increase of recirculating flow in the corner regions. Recordings of the oil flow show that this recirculation is very slow for the SCB in Figure 4.24c and gets stronger for the SCB in Figure 4.24d. The flow appears to be symmetric in the spanwise direction, and local recirculating flow is observed for the SCBr9t11 downstream of the bump crest. This is suspected to result from the upstream dimples in the Mach block as discussed in subsection 4.1.1.

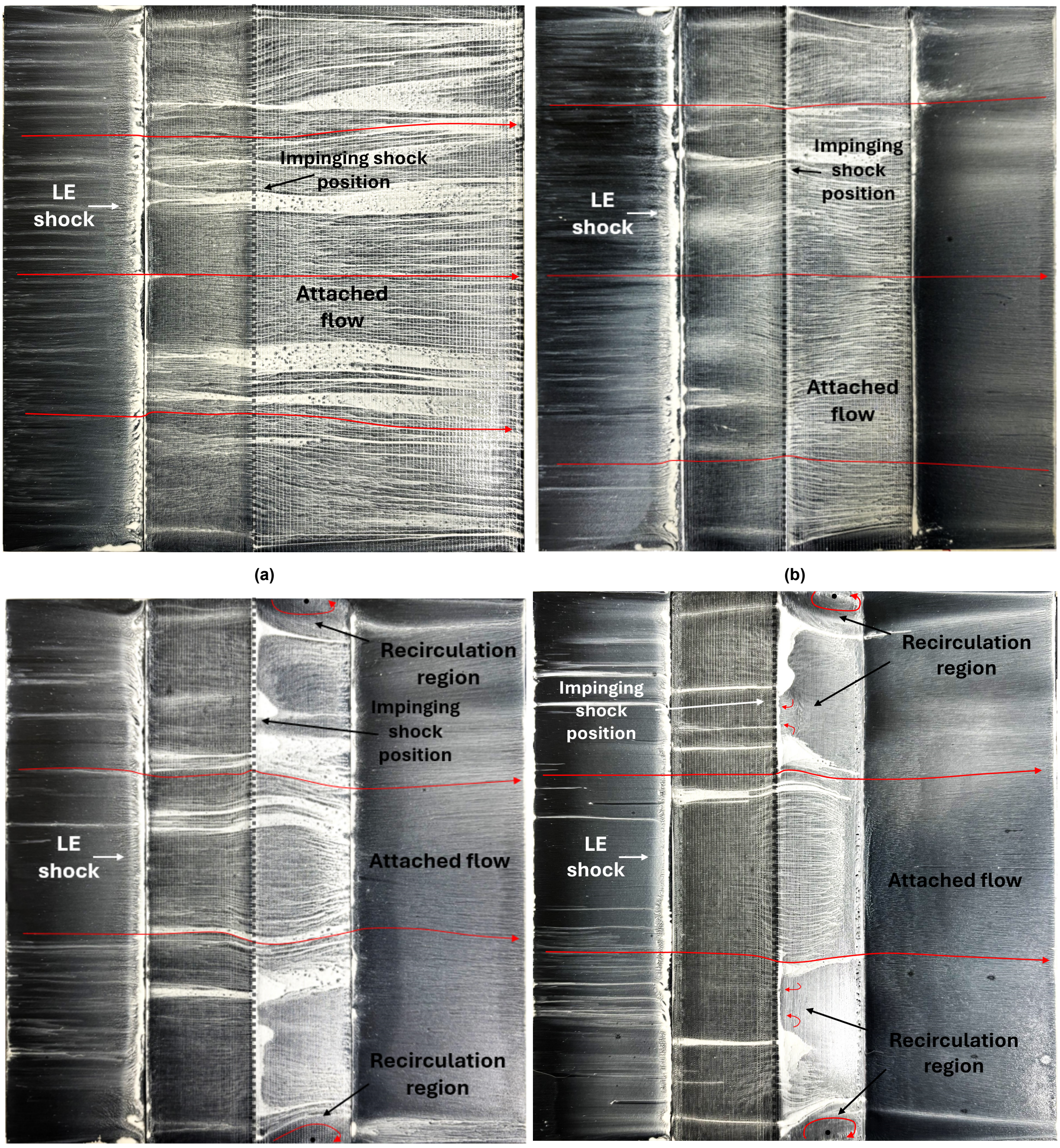

(a) (b) (c) (d)

Figure 4.24: Oil flow of bump tail angle variation for: a) SCBr9t3.5, b) SCBr9t7.5, c) SCBr9t9.5, and d) SCBr9t11. Images include annotations for the streamlines (red) and critical point theory (black). The streamlines associated with the focal points are simplified as dots (***F***) for clarity.

Impingement and Separation Locations of the Edge-Detection Algorithm

In this section, the results of the edge-detection algorithm are presented. These are tabulated in Table 4.4 for the bumps with tail angle variation. For comparison, the data of the uncontrolled and baseline interactions are repeated. The algorithm produces similar outcomes compared to the ramp variation and campaign A which are inconclusive.

Table 4.4: Quantification of the mean impingement and separation location $(\bar{x}/\delta_0)$ [-] per interaction case (tail variation) including the leading edge of the bumps, the standard deviation σ/δ_0 [-], mean interaction length $\bar{L}_{int}/\delta_0$ [-] and uncertainties ϵ [m]. The uncontrolled and baseline interactions are included for comparison.

Cases	$(\bar{x}/\delta_0)_{sep}$	$(\bar{x}/\delta_0)_{LE,bump}$	$(\bar{x}/\delta_0)_{inc}$	σ_{sep}/δ_0	σ_{inc}/δ_0	$\bar{L}_{int}$	ϵ_{sep}	ϵ_{inc}
Uncontrolled	-6.77	-	-0.013	0.28	0.21	6.76	$1.48\cdot10^{-4}$	$1.10\cdot10^{-4}$
SCBr9t3.5	-7.44	-6.91	-0.026	0.27	0.20	7.43	$6.60\cdot10^{-5}$	$4.98\cdot10^{-5}$
Baseline (SCBr9t5.5)	-6.74	-6.49	0.062	0.17	0.21	6.80	$9.01\cdot10^{-5}$	$1.10\cdot10^{-5}$
SCBr9t7.5	-6.79	-6.69	-0.014	0.25	0.20	6.78	$6.22\cdot10^{-5}$	$5.03\cdot10^{-5}$
SCBr9t9.5	-7.29	-7.03	0.095	0.22	0.21	7.39	$5.46\cdot10^{-5}$	$5.23\cdot10^{-5}$
SCBr9t11	-7.54	-6.67	0.029	0.22	0.16	7.57	$5.36\cdot10^{-5}$	$4.10\cdot10^{-5}$

Standard Deviation Distribution and Spectral Analysis

The spatial standard deviation distributions for the tail angle variation are given in Figure 4.25 in terms of σ_I and x/δ_0. It appears that the values near the bump leading edge do not show significant variation; it is comparable to the baseline bump interaction. On the other hand, increased values are observed on the tail part where compression waves are observed which coalesce in a shock. The expansion fan becomes more distinctive, and the values are reduced near the reflection shock wave.

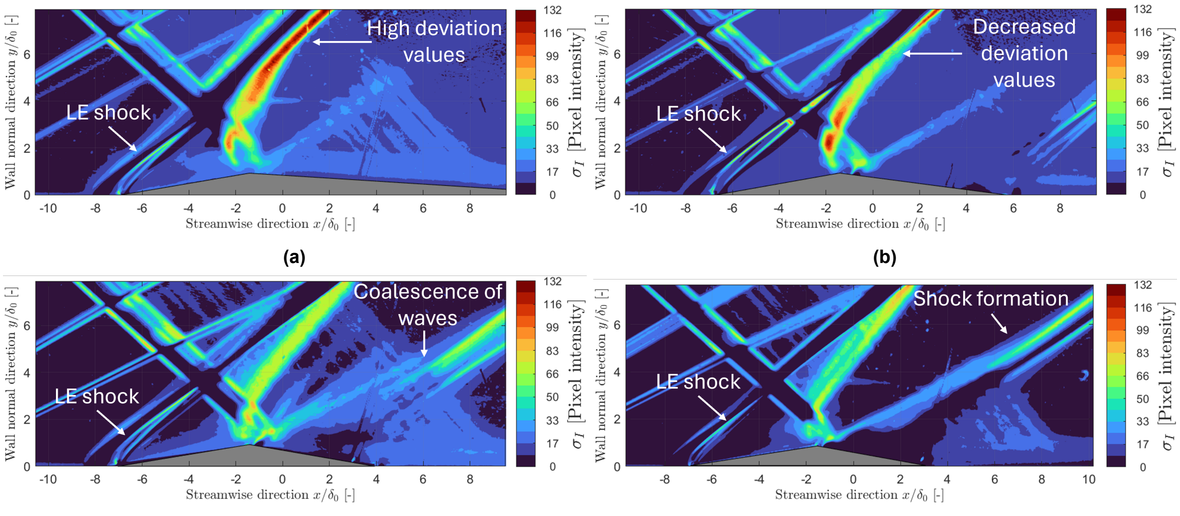

(a)

(b)

(c)

(d)

Figure 4.25: Spatial standard deviation distribution σ_I of bump tail angle variation for: a) SCBr9t3.5, b) SCBr9t7.5, c) SCBr9t9.5, and d) SCBr9t11. Coordinates are nondimensionalised by δ_0.

The spectral analysis for the tail angle variation is given in Figure 4.26. This plot also includes the baseline and uncontrolled interaction. The same plot in terms of frequency is given in Appendix B. It reveals that the content of the characteristic Strouhal region ($0.02 \leq St_{L_{int}} \leq 0.09$) of the uncontrolled interaction is removed for all the bumps. Only small regions with broadband Strouhal numbers are obtained close to the brighter areas in the Schlieren images. This is also the case for SCBr7t5.5 for the ramp variation.

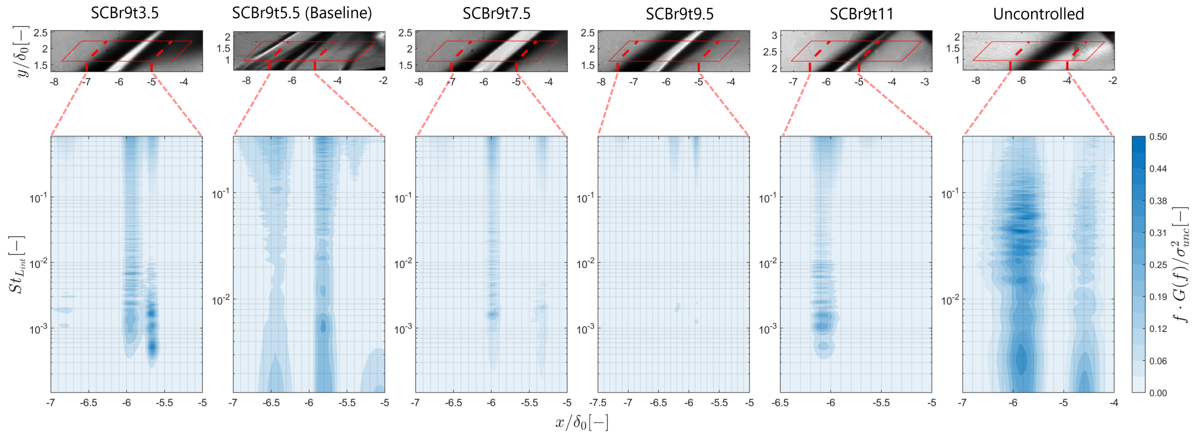

Figure 4.26: Pre-multiplied variance-normalised PSD distribution ($K = 8$ segments, $f_s = 25$ kHz) of the bumps with tail angle variation including the definition of the spectral boxes. The baseline and uncontrolled interaction are included as reference ($f_s = 10$ kHz, $L = 512$). Distributions are in terms of the nondimensional frequency $St_{L_{int}}$ and x/δ_0.

The variation in tail angle shows a primary trend on the tail part of the bumps. The Schlieren images show an increase in the generation of compression waves when the tail angle increases. On the other hand, the shock from the bump leading edge does not seem to change. Consider Figure 4.27 for a physical hypothesis which shows a simplified sketch of the SCBr9t11 flow structure in Figure 4.27b. The streamlines in region (A) are deflected by $\phi_B = 9°$ due to compression ramp shock (C_2) to region (B). These are then deflected due to the transmitted shock (C_3) to region (C) and eventually approach the expansion fan. Once traversed through this fan, they flow along the bump tail and approach the flat plate through a short distance. This relative abrupt change in curvature causes the streamlines to compress locally generating an array of compression waves. The waves coalesce in a shock, and the streamlines continue in the streamwise direction.

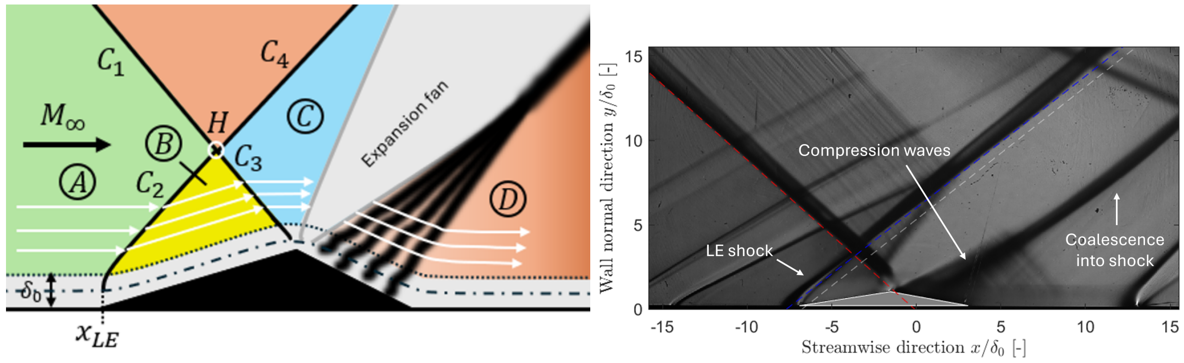

(a) (b)

Figure 4.27: Left: a simplified sketch of the 2D flow dynamics for the SCBr9t11 including the boundary layer, recirculation zone, streamlines, and annotated flow region and shock waves. Right: Average Schlieren image of SCBr9t11 including annotations, incident (red) reflection (blue), and uncontrolled reflection (grey) dashed lines. Coordinates normalised by δ_0.

Considering the spectral analysis, it appears that no characteristic low-frequency unsteadiness is obtained for all the bumps. This is similar to the flow dynamics of the baseline bump where the separation shock was replaced by a compression ramp shock. Since the flow experiences an increase in pressure due to the compression ramp shock rather than the impinging shock, a separation shock cannot be generated. For the shock emanating from the tail section of SCBr9t11, a spectral analysis was performed which is plotted in Figure 4.28. This figure shows the average Schlieren image of the spectral box (left) and the pre-multiplied variance-normalised PSD distribution of the spectral box (right). There seems to be no appreciable increase in spectral content in Strouhal numbers above $St_{L_{int}} = 0.01$. There are very low-frequency contributions suspected to be from the alternating current from the Dutch power grid. The downstream content is most likely the result of the Schlieren integration effect.

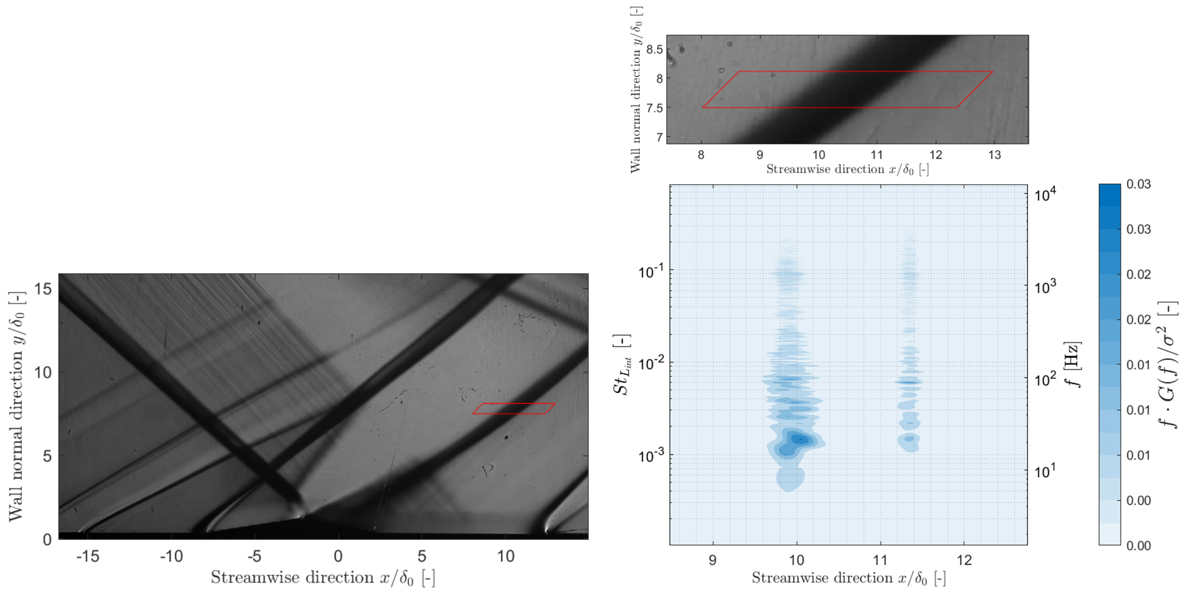

(a)

(b)

Figure 4.28: Left: average Schlieren image of SCBr9t11 with a spectral box for the shock emanating from the tail. Right: pre-multiplied variance-normalised PSD distribution for the spectral box shown in terms of the interaction length-based Strouhal number, frequency, and x/δ_0.

Another interesting observation is that the upstream dynamics are not altered by changes in the downstream geometry. This is in line with free-interaction theory, as discussed in subsection 2.1.3, which states that the upstream pressure rise is only a function of upstream influences (M_∞ and $c_{f,0}$) and not downstream parameters.

Occasional regions of broadband frequencies are observed in the spectral analysis for both the ramp and tail angle variation. It is suspected that this results from the spanwise integration effect of the Schlieren technique and the dark-bright regions near the bump leading edge observed in the Schlieren images. The dark-bright combination is the result of the 'connectivity' between the flat plate and the bump. In some cases, the wall transitioned as a step change rather than a smooth compression ramp since the bump was installed using double-sided tape. Thin tape was used during campaign A to mitigate this, but it influenced the oil flow process during wind tunnel runs. The tape was therefore discarded during campaign B. To illustrate this, consider Figure 4.29 which shows a close-up of the flat plate and leading edge of the bump. The streamlines (in red) need to traverse the bump curvature such that a compression region is formed followed by an expansion region. This could induce fluctuations which are not associated with the shock itself. Overall, there is no clear trend between the darker-brighter region or the integration effect on the concentrated fluctuating regions in the spectral analysis. It would be beneficial to utilise a different experimental technique such as PIV to possibly remove these spurious regions.

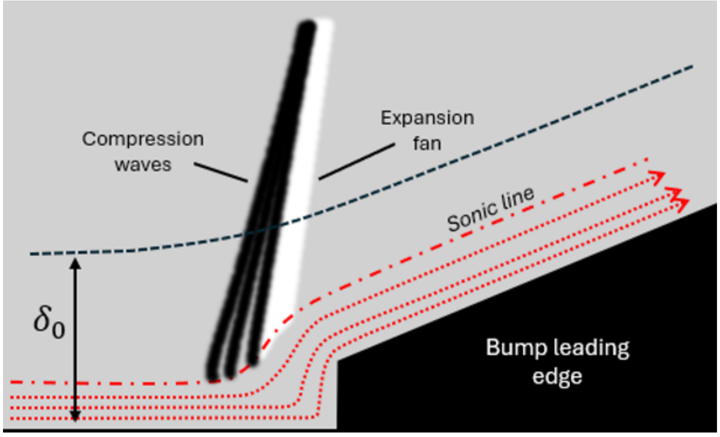

Figure 4.29: Simplified sketch showing the step change between flat plate and bump (i.e. 'connectivity'). The sketch includes the boundary layer (δ_0, $--$), streamlines (red, ··), the compression-expansion region, and the sonic line ($- \cdot -$).

Having explored both the bump geometry variation and impingement location, it can be questioned if the bump is suitable for reducing SWTBLI unsteadiness. A more optimal 'filling' of the separation bubble tends to show the highest reduction in the separation shock unsteadiness. This was primarily observed for the baseline bump interaction and change in impingement location. An increase in ramp angle or impingement in the upstream direction initiates the separation behaviour and generates unsteady behaviour. On the other hand, a downstream impingement or increase in tail angle shows no significant alteration in unsteady behaviour. Hence, the bump can reduce low-frequency unsteadiness, but the validity of this depends on the bump shape and impingement location. The industrial applications in which this design would function properly are restricted to cases with limited variation in impingement location for a fixed SCB shape. This could be in supersonic compression inlets during cruise flight, but the bump could only generate additional viscous drag and/or wave drag during other parts of the flight. An array of three-dimensional bumps would be more suitable as proposed by Ogawa and Babinsky (2008) and Ogawa et al. (2008). A form of surface morphing of the bumps could also be beneficial in achieving particular performance benefits during various parts of the flight. Another implementation would be an integrated approach with the bumps and industrial applications to obtain the desired performance benefits.

4.3. Discussion on the Methodology

The strengths and limitations of the utilised methods will be discussed in this section. First, the baseline bump will be discussed in subsection 4.3.1. Second, the edge-detection algorithm will be discussed in subsection 4.3.2. Third, the method of Welch (1967) will be discussed in subsection 4.3.3.

4.3.1. Baseline Bump Design

The baseline bump proposed in section 3.2 was based on PIV data and the inviscid model of the oblique SWTBLI. However, it can be questioned if the baseline design adequately represented the isobaric boundary. Based on the Schlieren and edge-detection results, the impinging and reflection shock lines were retrieved which can be investigated in more detail. The baseline bump height h and ramp length l_r were calculated using the incident shock angle β_{SG} or β_{inc} and the flow deflection angle due to the separation shock (see the methodology in subsection 3.2.1). The calculated impinging and reflection shock lines can aid in understanding if the bump was designed adequately. Therefore, consider Table 4.5 which shows the incident and reflection shock wave angles, β_{inc} and β_{ref} respectively, of the uncontrolled and baseline interaction. A counter-clockwise orientation of the angle is considered positive.

Table 4.5: Shock wave angles of the incident and reflection shocks of the uncontrolled and baseline bump interaction based on the linear regression of the edge-detection algorithm.

	β_{inc} [degrees]	β_{ref} [degrees]
Uncontrolled	-40.62	38.78
Baseline	-40.95	40.21

The uncontrolled and baseline bump interaction results show that the impinging shock angle is close to the theoretical shock wave angle of $\beta = -41.5°$ corresponding to $\phi = 12°$. The deviations are within a degree which results in a maximum flow deflection angle deviation to $\phi = 11°$ (Anderson, 2017). The deviation can be the result of the roughness of the shock generator or the calculation method used by the edge-detection algorithm. For this, see the results in subsection 4.1.1 and the discussion on the algorithm in subsection 4.3.2. As a result, the height and ramp length are influenced by this angle, but the deviation of one degree would not impose large changes on the design.

The reflection shock angle for the uncontrolled and baseline interaction has a corresponding flow deflection angle of $\phi \approx 9.5°$ and $\phi \approx 10.5°$, respectively (Anderson, 2017). The latter differs quite extensively from $\phi = 9.0°$ calculated in subsection 3.2.1. From the Schlieren images in subsection 4.1.1, the baseline bump reflection shock line does not accurately represent the LE shock location; the LE shock has a lower angle than the computed reflection shock line. The uncontrolled reflection shock line represents the separation shock more adequately but is still not parallel to the separation shock. Hence, it appears that the calculations of the flow deflection angles based on the PIV data are more in line with the Schlieren images than the lines of the edge-detection algorithm. This shows that the baseline bump angles and height are a sufficient first-order approximation of the inviscid SWBLI isobaric boundary.

Further improvement of the baseline bump design could be performed by calculating the mean separation location more accurately for the position of the bump LE. Additionally, the isobaric boundary is based on the sonic line of the boundary layer, and further analysis of the PIV data in this regard could result in a more optimum height of the bump (the distance between the wall and point *I* in the model). Finally, the bump geometry was designed using the interaction length reported in literature ($7\delta_0$). It would be more suitable to use the interaction length based on the PIV data rather than the literature.

4.3.2. Canny Edge-Detection Algorithm

The edge-detection algorithm was able to detect edges in the Schlieren frames. However, there are various factors which influence the detection and calculation of the impingement and separation location:

- Image resolution. For every analysed frame, it contained a pixel grid with an intensity. Therefore, the spatial dimensions of a pixel influence the calculation of the impingement and separation. If a frame has a high resolution, there will be less spatial ambiguity about the location of the shock edge and this edge can be better approximated. This could also lead to less variation in the impingement and separation location. Hence, the calculation error associated with the edge detection is of the order of the pixel dimension;
- Image quality. The detection of edges is significantly influenced by the level of noise in a frame (i.e. random or 'salt-and-pepper' noise) originating from dents, dust, or the camera. This aspect is discussed in section 4.1. As a result, edges can be misidentified such that the linear regression and the extrapolated locations are inaccurate. This noise needs to be adequately filtered using methods like background subtraction and/or image filtering;
- Gaussian filtering. The Canny algorithm filters the pixel intensity and its surrounding pixels based on the Gaussian distribution with a certain standard deviation σ. The subset of filtered pixels will increase as the standard deviation increases resulting in blurring of the image. Blurring can have the effect that edges are detected at a certain offset from the true edge. Thus, Gaussian filtering is helpful to reduce the effect of noise but also influences the detection of edges;
- Hysteresis thresholding. The final step of the Canny algorithm explained in subsection 3.4.2 is to apply hysteresis thresholding. The general idea is to identify edges within the user's initialised threshold range. If this range is small, relatively few edges will be retrieved. On the other hand,

if the range is unnecessarily large a subset of the retrieved edges is not associated with the true edge. For this reason, image quality is of high importance to reduce the unnecessary subset of edges. It can provide, however, a useful tool to suppress edges related to dust/noise with a relatively low threshold; and

- Box definition to extract points. As seen in the flow diagram of Figure 3.18 in subsection 3.4.1, a box is required to extract the points from the calculated edges. When the box size is relatively small, a small variance in the points can result in a large variance of the calculated impingement and/or separation location through linear regression. If the box is designed as large as possible, the linear regression of the shock will improve (provided that the variance is sufficiently small). Additionally, the shape of the box, as is done for the impinging shock, can help to reduce the effect of spurious edges on the linear regression.

In frequent cases, the edge-detection algorithm calculates an impingement or separation location relatively far from the mean of the distribution. This can be seen especially for the impingement locations which are expected to be close to $x/\delta_0 = 0.0$. To observe the accuracy of the algorithm in determining the locations, consider Figure 4.30. This figure shows the calculated impingement and separation location through time by the algorithm for the uncontrolled interaction. It includes the mean, maximum, and minimum values of these locations. The minimum and maximum values of the impingement and separation location have an associated linear regression of the extracted points. The extracted points, the linear regression, and the impingement and separation location are visually shown in Figure 4.31. This figure includes the raw Schlieren image in which the minimum and maximum impingement and separation locations were calculated. The red and blue squares indicate the mean impingement and separation location calculated by the algorithm.

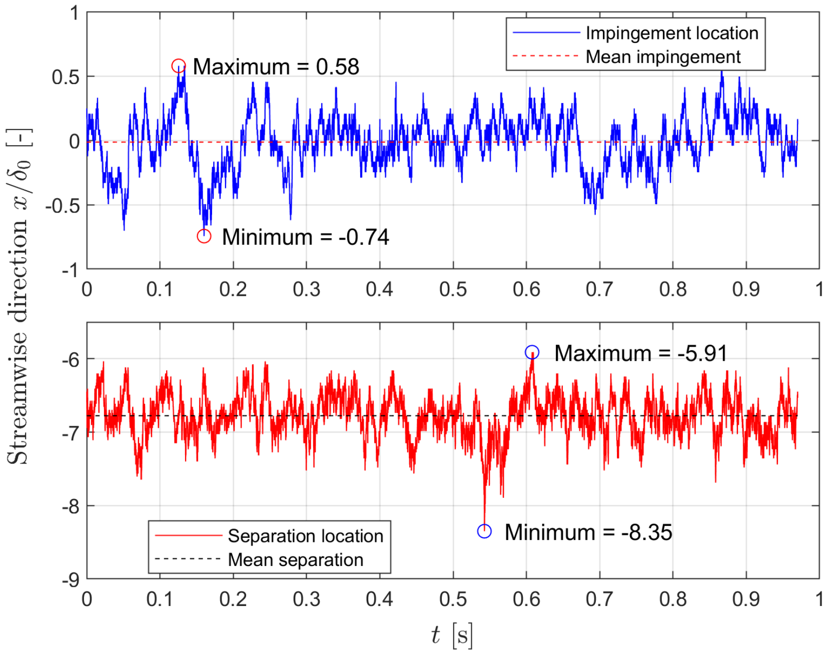

Figure 4.30: Impingement (upper) and separation (lower) location of the uncontrolled interaction through time calculated by the edge-detection algorithm including the mean, maximum, and minimum values of these locations ($f_s = 10$ kHz, $T = 0.9701$ s).

Considering the impingement locations, the results suggest that the points of the impinging shock edge (in green) are obtained close to this shock. Only points are obtained which are associated with the shock edge. The linear regression seems to approximate the shock adequately, but the impinging location differs from the mean location. For the separation locations, the extraction of points also seems to approximate the reflection shock, but the variation of the extrapolated separation location is larger compared to the impinging locations. The coefficient of determination R^2 can be useful to quantify how the linear regression fits the obtained points. This coefficient varies between zero and one, and a value of one indicates that the linear regression is an exact approximation of the data. All cases have an $R^2 = 0.99$ showing that the linear regression adequately represents these points. Hence, the shock shape or the approximation of the edge by the Canny algorithm seems most likely to generate excessive variation in the edge-detection data.

The impinging shock appears to change shape between frames which can be due to the corner effects or the Mach waves from the test section clamps. If the latter is the case, then the Mach waves are strong enough to cause refraction of the impinging shock. It can be observed that the Mach waves from the clamps are not parallel suggesting that these waves are weak shocks which can deflect the flow. This then affects the impinging shock, and it seems to be frame-dependent. It is more likely, however, that the change in edge shape results from the shock generator roughness or noise in the Schlieren frames. The choice of the reflection shock region for the separation location is also questionable since alterations in the separation shock position change the shape of the reflection shock. This affects the linear regression and translates to excessive variations in the data (as seen for the minimum case of the uncontrolled reflection shock).

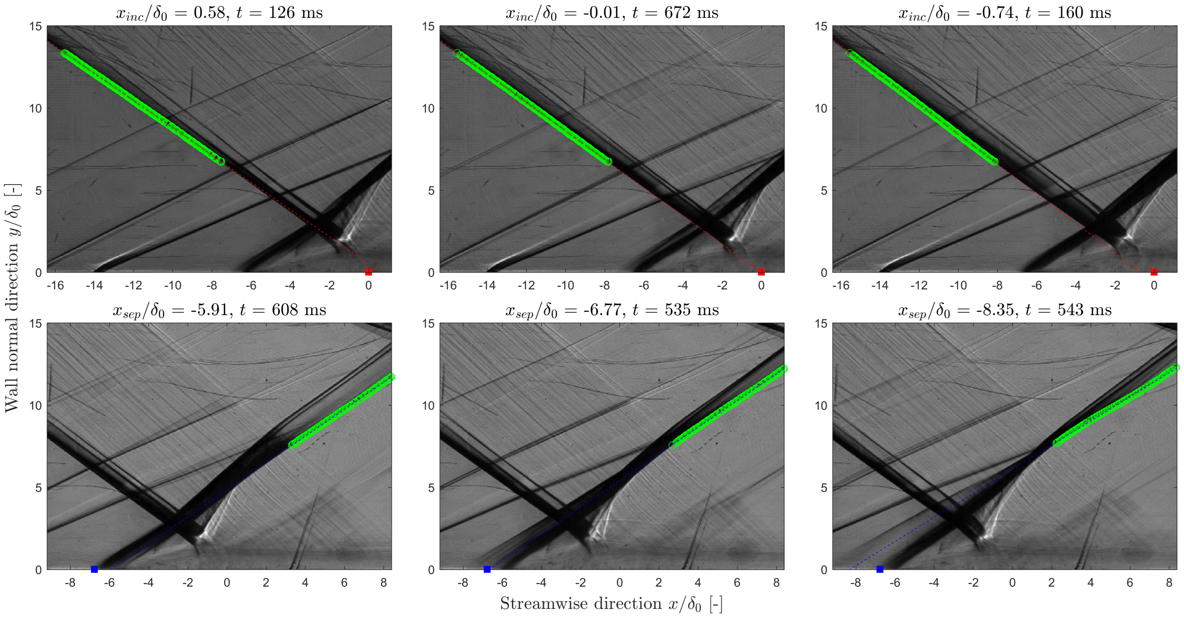

Figure 4.31: Visualisation of linear regression from the edge-detection in instantaneous Schlieren images and the effect on the extrapolated impingement and separation location. The uncontrolled interaction, impinging (upper figures, red line) and separation (lower figures, blue line) shock approximations are given. The green points are the points of the edges. The red and blue squares are the mean impingement and separation values, respectively.

The Canny algorithm uses local Gaussian filtering of the pixels to mitigate noise. The Gaussian distribution can be changed by the variance σ^2, and this alteration is investigated in Figure 4.32. It shows two zoomed-in Schlieren frames of the impinging shock during the uncontrolled interaction with the maximum extrapolated impingement location of $x/\delta_0 = 0.58$. It includes the definition of the box (red), extracted points (green) and resulting linear regression (dashed red). The left image has the default standard deviation of $\sigma = \sqrt{2}$ (as discussed in subsection 3.4.2) and the right uses $\sigma = 0.1$. The effect of the Gaussian filter reduces as the value approaches zero (see Equation 3.1), and 0.1 has been chosen since the Gaussian filtering cannot be deactivated in the algorithm. No significant changes are visible in the detected edges or linear regression while comparing both frames. The extrapolated impingement location for both cases equals the maximum impingement location of $x_{inc}/\delta_0 = 0.58$. In conclusion, it seems that the noise, as discussed in this section and subsection 4.1.1, affects the shape of the shock and, as a result, the detection of the edges and the extrapolated location.

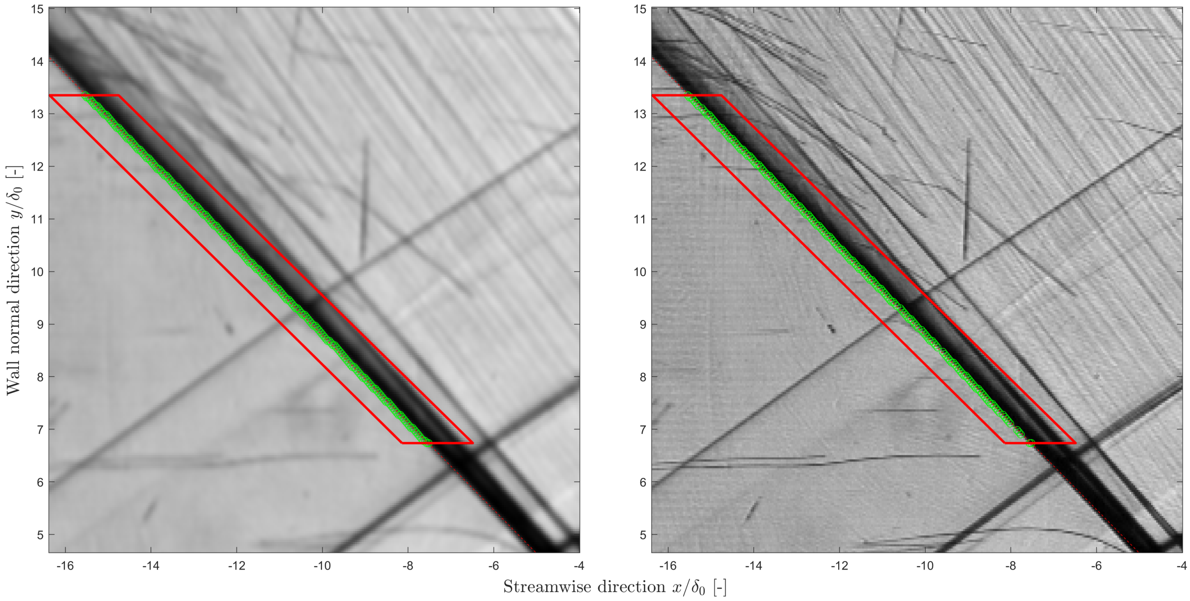

Figure 4.32: Images showing the effect of Gaussian filtering by the Canny-based edge-detection algorithm on the detection of edges. Figures include the spatial box (red) to extract the edges (green) and the linear regression (red dashed line). The left image uses $\sigma = \sqrt{2}$ (default value) and the right image uses $\sigma = 0.1$. Thresholds = [0.1, 0.25] (see subsection 3.4.1).

To illustrate the effect of noise filtering on the calculations, Figure 4.33 shows the effect of three noise mitigation methods on the separation location of the SCBr11t5.5 interaction. The left figure does not filter the raw images, the middle uses background subtraction, and the right uses background subtraction and preliminary Gaussian filtering (in addition to the Canny filtering). For this case, the calculations show that the separation location standard deviation increases for background subtraction relative to the results based on the raw images. For additive Gaussian filtering, however, the mean separation location shifted by approximately $\delta_0/2$ in the downstream direction. Gaussian filters obscure images such that edges lose their distinctive character. As such, the line detection has an offset and can influence the standard deviation and mean separation location. As discussed in section 4.1, it was assumed that the images had an Additive White Gaussian Noise (AWGN) distribution, but often the noise is distributed in a significantly more anisotropic way (Lim, 2006). Thus, it seems that the quality of the Schlieren images and the noise mitigation method are the main parameters influencing the results of the edge-detection method. It can detect the edges in the frames but needs further optimisation to calculate reliable results for the unsteady behaviour of the shock system.

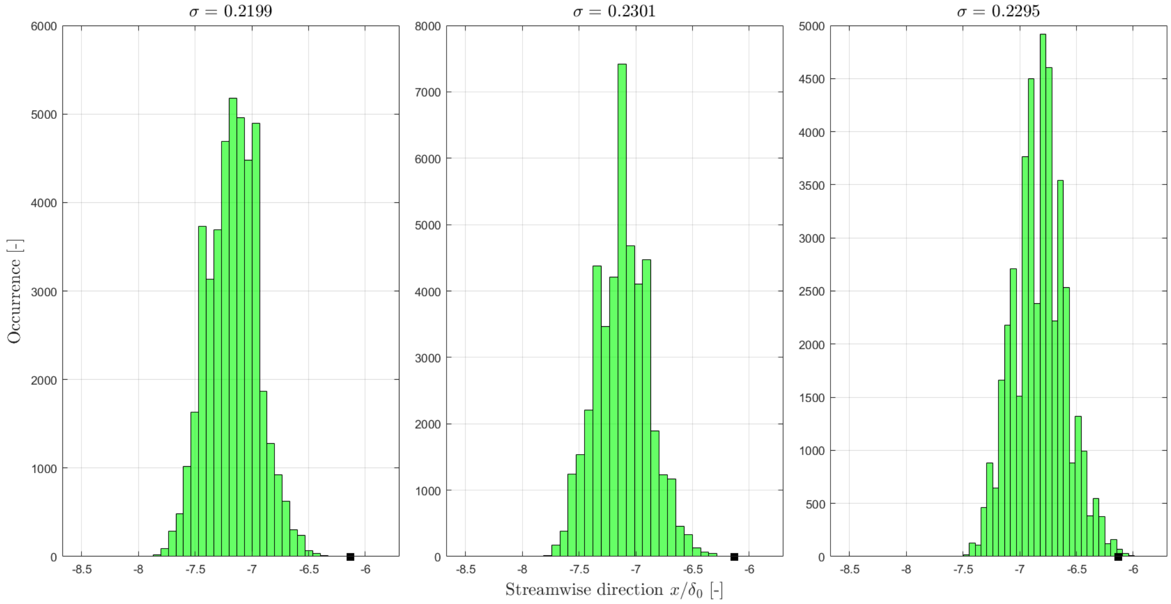

Figure 4.33: Sensitivity analysis of the edge-detection algorithm for the SCBr11t5.5 separation location with left) no background subtraction, middle) only background subtraction, and right) background subtraction and preliminary Gaussian filtering ($\sigma = 0.8$, bins = 25, 3σ-method applied). Black squares indicate the bump leading edge.

Throughout this section, it has been established that the accuracy of the edge-detection algorithm is mainly influenced by the noise in the Schlieren images and the noise mitigation methods. The background subtraction and Gaussian filtering of the Canny algorithm are insufficient to exclude the effect of noise on edge detection. The shock lines through time for the uncontrolled interaction showed that the shape of the shock mainly influences the edge-detection results for the algorithm settings. A close examination of the Gaussian filtering by the Canny algorithm seemed to suggest that this filtering does not influence the extrapolated impingement location. Additional Gaussian filtering of the images before the edges were computed showed that the results for the SCBr11t5.5 reflection shock were shifted and did not impose extra artificial variation due to the blurring of the edges. Hence, the noise mitigation can be improved. One method which could improve the results is subtracting the background images from the instantaneous frames in the frequency domain (Estruch et al., 2008; Li et al., 2019). A follow-up would be an (automated) optimisation between the Gaussian filtering, hysteresis thresholding, and the computed results. If the results continue to show unexpected fluctuating behaviour, the Schlieren image quality could be improved through an investigation of the camera settings and the noise levels in these images. Finally, a different method could be used instead of the Canny algorithm.

4.3.3. Welch's Method

Welch's method is based on computing the PSDs of *segments* of the input signal and averaging these segments to reduce the effect of noise. As a result, the size of these segments influences the obtained PSDs. If the segments are small, the noise will be equalised at the expense of reduced frequency resolution. This is vice versa for longer segments. Hence, it becomes a trial-and-error process to determine the optimum segment length. To illustrate this, a sensitivity analysis for different segment lengths is performed for the separation shock region of the uncontrolled interaction. These results in terms of pre-multiplied variance-normalised PSDs are given in Figure 4.34 with the Strouhal number and frequency in the streamwise direction. The effect of noise becomes more visible when the segment length increases. The increase in frequency resolution and range is also visible as the segment length increases. The methods described by Iwata et al. (2016) can be used to determine the optimum window length for the spectral analysis and transfer the trial-and-error to an analytically-based methodology.

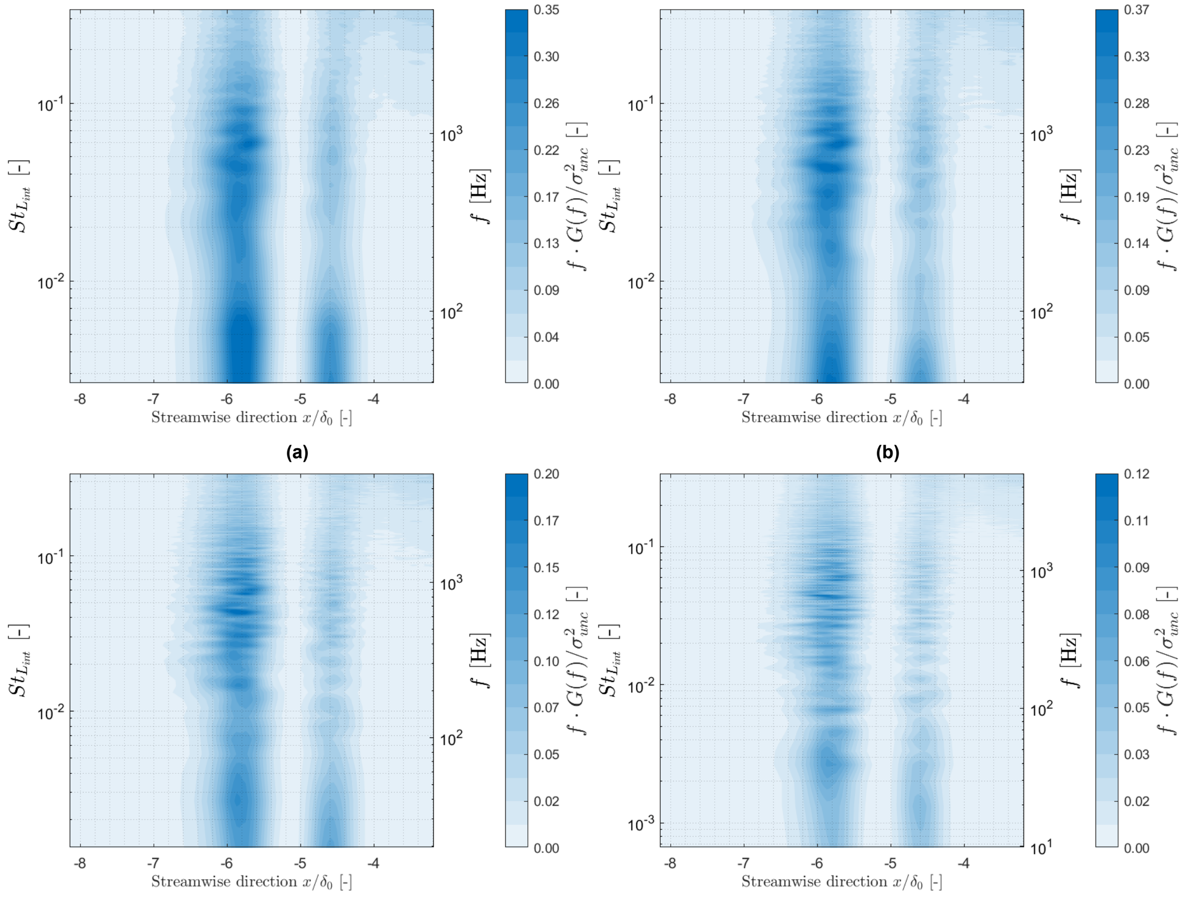

(a) (b) (c) (d)

Figure 4.34: Sensitivity analysis of Welch's method for the uncontrolled separation shock interaction for varying segment lengths: a) $L = 128$, b) $L = 256$, c) $L = 512$, and d) $L = 1024$. Results are the pre-multiplied variance-normalised PSDs for $St_{L_{int}}$ and f in the streamwise direction.

During the analysis, a standard Hamming window was used to compute the spectral content. Although this is a default setting of the *pwelch* function, different windows can be used such as the rectangular or Blackman window. They each have their characteristics regarding resolution and spectral leakage, and it would be interesting for further analysis if a trade-off could be made between different windows for the spectral analysis.

Overall, it can be argued that the Schlieren technique is an appropriate experimental technique to capture the spectral dynamics of an oblique SWTBLI. Although the main content is observed as documented by literature, a range of frequencies are captured which could be due to the integration effect of the Schlieren technique. Therefore, arriving at conclusions is difficult, and different techniques have to be sought to give definite conclusions.

5

Conclusion and Recommendations

This section concludes this research in section 5.1 and provides recommendations for future research in section 5.2.

5.1. Conclusion

An impinging Shock Wave-Turbulent Boundary Layer Interaction (SWTBLI) at Mach 2 and $\phi = 12^\circ$ was investigated experimentally while implementing two-dimensional Shock Control Bumps (SCBs) as a passive flow control technique. The objective was to identify the alteration in unsteadiness in the separation shock region due to this bump and its variation in geometry on a fundamental level. The isobaric boundary of the inviscid oblique SWBLI model served as the foundation of the bump design. The flow structure was investigated using Schlieren and oil flow visualisations, and the unsteadiness of the separation shock was quantified through a Canny-based edge-detection algorithm and spectral analysis using Welch's method.

Experimental campaign A was conducted to design the spanwise geometry of the baseline bump such that the flow structure showed a nominal two-dimensional behaviour. This bump design was used in experimental campaign B to observe the alteration in unsteady dynamics due to bump geometry variation. The ramp and tail angle of the bump were changed individually, and a range of angles was tested to observe a possible trend. Campaign A revealed that a bump with a spanwise length equal to the wind tunnel test section generated nominal two-dimensional behaviour. The uncontrolled separation shock was effectively replaced by a compression ramp shock originating from the bump leading edge, and the standard deviation based on the edge-detection algorithm results of this shock showed the highest decrease compared to the uncontrolled interaction. Spectral analysis of the uncontrolled separation shock retrieved a range of (interaction length-based) Strouhal numbers between $0.02 \leq St_{L_{int}} \leq 0.09$ with relatively high peaks near $St_{L_{int}} \approx 0.04 - 0.05$. This is close to $St_{L_{int}} = 0.03$ frequently reported in literature. The Strouhal range is suspected to result from corner effects in the wind tunnel. The aforementioned bump design showed that the characteristic spectral content was removed. Other spanwise bump designs showed a more three-dimensional, unsteady behaviour based on the edge-detection and spectral analysis results.

For campaign B, an increase in ramp angle showed the generation of a separation bubble upstream of the bump leading edge. The spectral analysis indicated similarities with the uncontrolled interaction but no characteristic low-frequency unsteadiness. It is suspected that the pressure gradient due to the impinging shock becomes more dominant compared to the compression ramp pressure gradient as the ramp angle increases. This allows for separation shock behaviour, but the separation bubble is terminated and the flow reattaches again as the flow traverses to the bump leading edge. This does not allow the full development of separation bubble breathing and shear layer flapping to unlock the characteristic low-frequency unsteadiness. The variation in tail angle showed no significant unsteadiness alterations in the bump leading edge region while compression waves were generated downstream on the bump crest coalescing in a shock. An alteration in impingement location on the bump showed that downstream shifting did not generate additional unsteady behaviour in the bump leading edge region while upstream shifting generated unsteady dynamics comparable to the increase in ramp angle. The same hypothesis for increasing ramp angle applies: the increased exposure of the boundary layer to the incident shock pressure gradient induces separation, but this suppresses the separation bubble breathing and shear layer flapping.

Frequently, results indicated that the Schlieren images contained a high degree of random noise. This was observed most notably in the edge-detection of the incident shock, which consistently detected the impingement location centred around $x/\delta_0 = 0.0$ with a standard deviation $\sigma/\delta_0 \approx 0.2$. Similar conclusions were drawn from the spatial standard deviation distributions. The results based on Welch's method were more convincing as it is specifically designed to mitigate noise in a signal. This showed that the edge-detection algorithm results were not trustworthy although such a method could have potential in detecting shock edges in Schlieren images. The noise in the Schlieren images can be seen as the measurement uncertainty, and it is most likely that it originates from the cameras during the experiment.

5.2. Recommendations

The following areas of interest are proposed for future research:

1. The computation of the impingement and separation location through the edge-detection algorithm could be improved. Specifically, the methods to mitigate noise in Schlieren images should be investigated and the requirements of the Schlieren images to perform adequate edge-detection. This can be achieved by performing frequency-domain background subtraction (Estruch et al., 2008; Li et al., 2019), optimising the Canny algorithm (Gaussian filtering and hysteresis thresholding) and Schlieren camera settings, or using a different technique proposed by Bulut et al. (2022) and Nazari et al. (2020);
2. Despite the efforts regarding mitigating the corner effects in the wind tunnel, it would be advantageous to obtain a better (quantitative) understanding of the flow dynamics. This can be obtained through, for instance, PIV. In this research, the Schlieren technique integrates the deflection of light rays due to changes in density over the spanwise direction which translates to the observation of three-dimensional effects (if present). This was primarily the case for the uncontrolled interaction. If planar PIV is applied to the centred interaction, more quantitative flow dynamics can be obtained for further, more detailed, unsteady analysis. As an example: turbulence intensity levels and separation probability distributions (Bulut et al., 2024), Spectral Proper Orthogonal Decomposition (SPOD) (e.g. Cottier et al., 2019), autocorrelation distributions (Souverein et al., 2009; van Oudheusden et al., 2011) or spectral analysis. Other techniques can also be applied such as unsteady pressure transducers or Unsteady Pressure Sensitive Paint (uPSP);
3. The results obtained through this research (or from more advanced techniques) can be combined with a verification and validation study through numerical simulations of LES and/or DNS. (U)RANS methods remain to this day unable to capture the unsteady flow dynamics of the interaction (as pointed out by Gaitonde (2015)), and LES and DNS have successfully been applied to SWTBLIs (Laguarda et al., 2024; Pasquariello et al., 2017). This technique allows for stability analysis of the low-frequency unsteadiness through for example (Sparsity Promoting) Dynamic Mode Decomposition ((SP)DMD); and
4. The design space for the 2D-SCB in this research is limited to specific applications in the aeronautical industry. This technique, however, could potentially have beneficial outcomes in duct-shaped supersonic flow such as engine inlets. In this case, it would also only work for specific flight conditions. Hence, an integrated approach with the bumps and an industrial application could fully unlock the benefits associated with these bumps. Surface morphing and 2D-SCBs would be advantageous to obtain performance benefits over a larger range of conditions instead of a single optimised condition.

References

Aditya, A. (2022). *Experimental study of shock wave / boundary-layer interactions over fluttering panels* [Master's thesis, Delft University of Technology]. https://resolver.tudelft.nl/uuid:ab721f52-f6b3-4dfc-b646-21fb91adabc8

Allerhand, P. (2020). *An experimental investigation of shock-induced panel flutter using simultaneous piv and dic* [Master's thesis, Delft University of Technology]. https://resolver.tudelft.nl/uuid:69f3db7f-1bf4-46a2-9aed-2e1021b1e8a2

Anderson, J. (2017). *Fundamentals of aerodynamics*. McGrawHill.

Babinsky, H., & Harvey, J. (2011). *Shock wave-boundary-layer interactions*. Cambridge University Press.

Babinsky, H., Oorebeek, J., & Cottingham, T. (2013). Corner effects in reflecting oblique shock-wave/boundary-layer interactions. *51st AIAA Aerospace Sciences Meeting including the New Horizons Forum and Aerospace Exposition*. https://doi.org/10.2514/6.2013-859

Beresh, S., Clemens, N., & Dolling, D. (2002). Relationship between upstream turbulent boundary-layer velocity fluctuations and separation shock unsteadiness. *AIAA Journal*, *40*(12). https://doi.org/10.2514/2.1609

Bruce, P., & Colliss, S. (2015). Review of research into shock control bumps. *Shock Waves*, 451–471. https://doi.org/10.1007/s00193-014-0533-4

Bruce, P., Colliss, S., & Babinsky, H. (2014). Three-dimensional shock control bumps: Effects of geometry. *52nd Aerospace Science Meeting*. https://doi.org/10.2514/6.2014-0943

Bulut, J., Schrijer, F., & van Oudheusden, B. Effect of shock control bumps on oblique shock wave turbulent boundary layer interactions. In: In *56th 3af international conference on applied aerodynamics*. 2022.

Bulut, J., Schrijer, F., & van Oudheusden, B. Investigation of shock control bump geometry variation on oblique shock wave boundary layer interactions (unpublished). In: In *57th 3af international conference on applied aerodynamics*. 2023.

Bulut, J., Schrijer, F., & van Oudheusden, B. (2024). Impinging shock wave boundary layer interactions control with shock control bumps. *AIAA Aviation Forum and SCEND, 2024*. https://doi.org/10.2514/6.2024-4526

Chapman, D., Kuehn, D., & Larson, H. (1958). *Investigation of separated flows in supersonic and subsonic streams with emphasis on the effect of transition* (tech. rep. No. NACA-TR-1356). NACA.

Clemens, N., & Narayanaswamy, V. (2014). Low-frequency unsteadiness of shock wave/turbulent boundary layer interactions. *Annual Review Fluid Mechanics*, 469–492. https://doi.org/10.1146/annurev-fluid-010313-141346

Colliss, S., Babinsky, H., Bruce, P., Nübler, K., & Lutz, T. (2012). An experimental investigation of three-dimensional shock control bumps applied to transonic airfoils. *50th AIAA Aerospace Sciences Meeting including the New Horizons Forum and Aerospace Exposition*. https://doi.org/10.2514/6.2012-43

Colliss, S., Babinsky, H., Nübler, K., & Lutz, T. (2014). Joint experimental and numerical approach to three-dimensional shock control bump research. *AIAA Journal*, *52*(2). https://doi.org/10.2514/1.J052582

Colliss, S., Babinsky, H., Nübler, K., & Lutz, T. (2016). Vortical structures on three-dimensional shock control bumps. *AIAA Journal*, *43*(4), 1–13. https://doi.org/10.2514/1.J054669

Cottier, S., Combs, C., & Vanstone, L. (2019). Spectral proper orthogonal decomposition analysis of shock-wave/boundary-layer interactions. *AIAA Aviation 2019 Forum*. https://doi.org/10.2514/6.2019-3331

Cui, S., Wang, Y., Qian, X., & Deng, Z. (2013). Image processing techniques in shockwave detection and modeling. *Journal of Signal and Information Processing*, *4*, 109–113. https://doi.org/10.4236/jsip.2013.43B019

D’Aguanno, A. (2023). *Physics and control of transonic buffet* [Doctoral dissertation, Delft University of Technology]. https://doi.org/https://doi.org/10.4233/uuid:7e4f868b-7716-4c36-8fa0-b55572d1572b

Delery, J. (1985). Shock wave/turbulent boundary layer interaction and its control. *Progress in Aerospace Science*, *22*, 209–280.

Dolling, D. (2001). Fifty years of shock-wave/boundary-layer interaction research: What next? *AIAA Journal*, *39*(8). https://doi.org/10.2514/2.1476

Dores, F. (2024). *Passive control of shock wave turbulent boundary layer interaction over a perforated wall* [Master’s thesis, Technical University Delft].

Dupont, P., Haddad, C., & Debiève, J. (2006). Space and time organization in a shock-induced separated boundary layer. *Journal of Fluid Mechanics*, *559*, 255–277. https://doi.org/10.1017/S0022112006000267

Dussage, J., Dupont, P., & Debiève, J. (2005). Unsteadiness in shock wave boundary layer interactions with separation. *Aerospace Science and Technology*, *10*. https://doi.org/10.1016/j.ast.2005.09.006

Erengil, M., & Dolling, D. (1991). Unsteady wave structure near separation in a mach 5 compression ramp interaction. *AIAA Journal*, *29*(5). https://doi.org/10.2514/3.10647

Estruch, D., Lawson, N., MacManus, D., Garry, K., & Stollery, J. (2008). Measurement of shock wave unsteadiness using a high-speed schlieren system and digital image processing. *Review of Scientific Instruments*, *79*. https://doi.org/10.1063/1.3053361

Fan, J., Uy, K., Hao, J., & Wen, C. (2024). Coexistence of different mechanisms underlying the dynamics of supersonic turbulent flow over a compression ramp. *Physics of Fluids*, *36*(1). https://doi.org/10.1063/5.0185961

Forsyth, D., & Ponce, J. (2011). *Computer vision: A modern approach, second edition*. Pearson.

Gaitonde, D., & Adler, M. (2023). Dynamics of three-dimensional shock-wave/boundary-layer interactions. *Annual Review of Fluid Mechanics*, *55*, 291–321. https://doi.org/10.1146/annurev-fluid-120720-

Gaitonde, D. (2015). Progress in shock wave/boundary layer interactions. *Progress in Aerospace Sciences*, *72*, 80–99. https://doi.org/10.1016/j.paerosci.2014.09.002

Ganapathisubramani, B., Clemens, N., & Dolling, D. (2007). Effects of upstream boundary layer on the unsteadiness of shock-induced separation. *Journal of Fluid Mechanics*, *585*, 369–394. https://doi.org/10.1017/S0022112007006799

Ganapathisubramani, B., Clemens, N., & Dolling, D. (2009). Low-frequency dynamics of shock-induced separation in a compression ramp interaction. *Journal of Fluid Mechanics*, *636*, 397–425. https://doi.org/10.1017/S0022112009007952

Giepmann, R. (2016). *Flow control for oblique shock wave reflections* [Doctoral dissertation, Delft University of Technology]. https://doi.org/https://doi.org/10.4233/uuid:597489bb-0b41-4da2-8ec4-b1bc390f8d2c

Glezer, A., & Amitay, M. (2002). Synthetic jets. *Annual Review of Fluid Mechanics*. https://doi.org/10.1146/annurev.fluid.34.090501.094913

Gramann, R., & Dolling, D. (1992). A preliminary study of the turbulent structures associated with unsteady separation shock motion in a mach 5 compression ramp interaction. *30th Aerospace Sciences Meeting and Exhibit*. https://doi.org/10.2514/6.1992-744

Grilli, M., Schmid, P., Hickel, S., & Adams, N. (2012). Analysis of unsteady behaviour in shockwave turbulent boundary layer interaction. *Journal of Fluid Mechanics 700*, *700*, 16–28. https://doi.org/10.1017/jfm.2012.37

Hadjadj, A., Larsson, J., Morgan, B., Nichols, J., & Lele, S. (2010). Large-eddy simulation of shock/boundary-layer interaction. *Center for Turbulence Research: Proceedings of the Summer Program 2010*.

Hu, W., Hickel, S., & van Oudheusden, B. (2022). Unsteady mechanisms in shock wave and boundary layer interactions over a forward-facing step. *Journal of Fluid Mechanics*, *949*. https://doi.org/10.1017/jfm.2022.737

Huang, W., Wu, H., Yang, Y., Yan, L., & Li, S. (2020). Recent advances in the shock wave/boundary layer interaction and its control in internal and external flows. *Acta Astronautica*, *174*, 103–122. https://doi.org/10.1016/j.actaastro.2020.05.001

Humble, R., Elsinga, G., Scarano, F., & van Oudheusden, B. (2009). Three-dimensional instantaneous structure of a shock wave/turbulent boundary layer interaction. *Journal of Fluid Mechanics*, *622*, 33–62. https://doi.org/10.1017/S0022112008005090

Irie, K., Woodhead, I., McKinnon, A., & Unsworth, K. (2009). Measured effects of temperature on illumination-independent camera noise. *24th International Conference Image and Vision Computing New Zealand*. https://doi.org/10.1109/IVCNZ.2009.5378403

Iwata, H., Umebayashi, K., Tiiro, S., Lehtomäki, J., Lóped-Benítez, M., & Suzuki, Y. (2016). Welch fft segment size selection method for spectrum awareness system. *IEICE Transactions on Communications*, *E99-B*(8). https://doi.org/10.1587/transcom.2015EBP3401

Jana, T., & Kaushik, M. (2022). Survey of control techniques to alleviate repercussions of shock-wave and boundary-layer interactions. *Advances in Aerodynamics*, *4*. https://doi.org/10.1186/s42774-022-00119-9

Katzer, E. (2006). On the lengthscales of laminar shock/boundary-layer interaction. *Journal of Fluid Mechanics*, *206*, 477–496. https://doi.org/10.1017/S0022112089002375

Kingsbury, N. (1990). *Aerospace technology: Technical data and information on foreign test facilities* (tech. rep.). United States General Accounting Office.

Laguarda, L., Hickel, S., Schrijer, F., & van Oudheusden, B. (2024). Reynolds number effects in shock-wave/turbulent boundary-layer interactions. *Journal of Fluid Mechanics*, *989*, A20. https://doi.org/10.1017/jfm.2024.361

Li, G., Agir, M., Kontis, H., Ukai, T., & Rengarajan, S. (2019). Image processing techniques for shock wave detection and tracking in high speed schlieren and shadowgraph systems. *Journal of Physics: Conference Series*, *1215*. https://doi.org/10.1088/1742-6596/1215/1/012021

Lim, S. (2006). Characterization of noise in digital photographs for image processing. *Digital Photography II*, *6069*. https://doi.org/10.1117/12.655915

Loginov, M., Adams, N., & Zheltovodov, A. (2006). Large-eddy simulation of shock-wave/turbulent-boundary-layer interaction. *Journal of Fluid Mechanics*, *565*, 135–169. https://doi.org/10.1017/S0022112006000930

Mahmood, G., Hill, M., Nelson, D., Ligrani, P., Moon, H., & Glezer, B. (2000). Local heat transfer and flow structure on and above a dimpled surface in a channel. *45th International Gas Turbine and Aeroengine Congress and Exhibition*. https://doi.org/10.1115/1.1333694

McClure, W. (1992). *An experimental study of the driving mechanism and control of the unsteady shock induced turbulent separation in a mach 5 compression corner flow* [Doctoral dissertation, University of Texas].

Missing, T., Babinsky, H., & Schrijer, F. A novel shock control bump for oblique shock wave boundary layer interactions (unpublished). In: In *58th 3af international conference on applied aerodynamics*. 2024, March.

Nazari, A., Ishino, Y., Ito, F., Kondo, H., Yamada, R., Motohiro, T., Saiki, Y., Miyazato, Y., & Nakao, S. (2020). Quantitative schlieren image-noise reduction using inverse process and multi-path integration. *Journal of Flow Control, Measurement & Visualisation*, *8*, 25–44. https://doi.org/10.4236/jfcmv.2020.82002

Nichols, J., Larsson, J., Bernardini, M., & Pirozzoli, S. (2017). Stability and modal analysis of shock-/boundary layer interactions. *Theoretical and Computational Fluid Dynamics*, *31*, 33–50. https://doi.org/10.1007/s00162-016-0397-6

Ogawa, H., & Babinsky, H. (2008). Shock / boundary-layer interaction control using three-dimensional bumps in supersonic engine inlets. *46th AIAA Aerospace Sciences Meeting and Exhibit*. https://doi.org/10.2514/6.2008-599

Ogawa, H., Babinsky, H., Pätzold, M., & Lutz, T. (2008). Shock-wave/boundary-layer interaction control using three-dimensional bumps for transonic wings. *AIAA Journal*, *46*(6). https://doi.org/10.2514/1.32049

Pasquariello, V., Hickel, S., & Adams, N. (2017). Unsteady effects of strong shock-wave/boundary-layer interaction at high reynolds number. *Journal of Fluid Mechanics*, *823*, 617–657. https://doi.org/10.1017/jfm.2017.308

Photron. (n.d.-a). *Fastcam sa1.1 ultra high-speed video system [fact sheet]* (tech. rep.). https://www.highspeedimaging.com/wp-content/uploads/2023/12/Fastcam_SA1_Datasheet.pdf

Photron. (n.d.-b). *Photron nova s12 [fact sheet]* (tech. rep.). https://www.highspeedimaging.com/photron-fastcam-nova-s12/

Pipponiau, S., Dussauge, J., Debiève, J., & Dupont, P. (2009). A simple model for low-frequency unsteadiness in shock-induced separation. *Journal of Fluid Mechanics*, *629*, 87–108. https://doi.org/10.1017/S0022112009006417

Pirozzoli, S., & Grasso, F. (2006). Direct numerical simulation of impinging shock wave/turbulent boundary layer interaction at m=2. *Physics of Fluid*, *18*. https://doi.org/10.1063/1.2216989

Plotkin, K. (1975). Shock wave oscillation driven by turbulent boundary-layer fluctuations. *AIAA Journal*, *13*(8), 1036–1040. https://doi.org/10.2514/3.60501

Poggie, J., Bisek, N., Kimmel, R., & Stanfield, S. (2015). Spectral characteristics of separation shock unsteadiness. *AIAA Journal*, *53*(1), 200–214. https://doi.org/10.2514/1.J053029

Priebe, S., & Martín, M. (2011). Low-frequency unsteadiness in shock wave-turbulent boundary layer interaction. *Journal of Fluid Mechanics*, *699*, 1–49. https://doi.org/10.1017/jfm.2011.560

Radaelli, M. (2024). *An experimental investigation into shock-induced panel flutter* [Master's thesis, Delft University of Technology]. https://repository.tudelft.nl/record/uuid:72f1e27c-eb0a-494e-b3b7-bda2877513db

Rohlfs, L., Stab, I., & Weiss, J. (2022). Experimental investigation of incident shockwave boundary layer interactions in a continuously operating supersonic wind tunnel. *AIAA Aviation 2002 Forum*. https://doi.org/10.2514/6.2022-4134

Sabnis, K., & Babinsky, H. (2023). A review of three-dimensional shock wave-boundary-layer interactions. *Progress in Aerospace Sciences*. https://doi.org/10.1016/j.paerosci.2023.100953

Saric, W. (1994). Görtler votices. *Annual Review of Fluid Mechanics*, *26*, 379–409. https://doi.org/10.1146/annurev.fl.26.010194.002115

Souverein, L., Bakker, P., & Dupont, P. (2013). A scaling analysis for turbulent shock-wave/boundary-layer interactions. *Journal of Fluid Mechanics*, 505–535. https://doi.org/10.1017/jfm.2012.495

Souverein, L., Dupont, P., Debiève, J., Dussauge, J., van Oudheusden, B., & Scarano, F. (2010). Effect of interaction strength on unsteadiness in turbulent shock-wave-induced separtions. *AIAA Journal*, *48*(7), 1480–1493. https://doi.org/10.2514/1.J050093

Souverein, L., van Oudheusden, B., Scarano, F., & Dupont, P. (2009). Application of a dual-plane particle image velocimetry (dual-piv) technique for the unsteadiness characterization of a shock wave turbulent boundary layer interaction. *Measurement Science and Technology*, *20*(7). https://doi.org/10.1088/0957-0233/20/7/074003

Stanewsky, E., Dèlery, J., Fulker, J., & de Matteis, P. (2002). *Euroshock ii: Drag reduction by shock and boundary layer control*. Springer. https://doi.org/10.1007/978-3-540-45856-2

Thomas, F., Putnam, C., & Chu, H. (1994). On the mechanism of unsteady shock oscillation in shock wave/turbulent boundary layer interactions. *Experiments in Fluids*, *18*, 69–81. https://doi.org/10.1007/BF00209362

Touber, E., & Sandham, N. (2009). Large-eddy simulation of low-frequency unsteadiness in a turbulent shock-induced separation bubble. *Theoretical and Computational Fluid Dynamics*, *29*, 79–107. https://doi.org/10.1007/s00162-009-0103-z

Touber, E., & Sandham, N. (2011). Low-order stochastic modelling of low-frequency motions in reflected shock-wave/boundary-layer interactions. *Journal of Fluid Mechanics*, *671*, 417–465. https://doi.org/10.1017/S0022112010005811

Tropea, C., Yarin, A., & Foss, J. (2007). *Springer handbook of experimental fluid mechanics*. Springer.

Vadillo, J., Agarwal, R., & Hassan, A. (2005). Active control of shock/boundary layer interaction in transonic flow over airfoils. *43rd AIAA Aerospace Sciences Meeting and Exhibit*. https://doi.org/10.2514/6.2005-486

van Oudheusden, B., Jöbsis, A., Scarano, F., & Souverein, L. (2011). Investigation of the unsteadiness of a shock-reflection interaction with time-resolved particle image velocimetry. *Shock Waves*, *21*, 397–409. https://doi.org/10.1007/s00193-011-0304-4

Wang, B., Sandham, N., Hu, Z., & Liu, W. (2015). Numerical study of oblique shock-wave/boundary-layer interaction considering sidewall effects. *Journal of Fluid Mechanics*, *767*, 526–561. https://doi.org/10.1017/jfm.2015.58

Welch, P. (1967). The use of fast fourier transform for the estimation of power spectra: A method based on time averaging over short, modified periodograms. *IEEE Transactions on audio and electroacoustics*, *15*.

White, F., & Majdalani, J. (2022). *Viscous fluid flow* (Fourth). McGrawHill.

Wu, M., & Martín, P. (2008). Analysis of shock motion in shockwave and turbulent boundary layer interaction using direct numerical simulation data. *594*, 71–83. https://doi.org/10.1017/S0022112007009044

Xiang, X., & Babinsky, H. (2019). Corner effects for oblique shock wave/turbulent boundary layer interactions in rectangular channels. *Journal of Fluid Mechanics*, *862*, 1060–1083. https://doi.org/10.1017/jfm.2018.983

Zhuang, Y., Tan, H., Li, X., Sheng, F., & Zhang, Y. (2018). Letter: Görtler-like vortices in an impinging shock wave/turbulent boundary layer interaction flow. *Physics of Fluid*, *30*(6). https://doi.org/10.1063/1.5034242

Ziemer, R., Tranter, W., & Fannin, D. (1998). *Signal & systems: Continuous and discrete, fourth edition*. Prentice-Hall.

A

Average Schlieren Images Without Impinging Shock Wave

This appendix shows the average Schlieren images of the used bumps without an impinging shock wave. This includes the baseline bump and the bumps with alteration in ramp and tail angle.

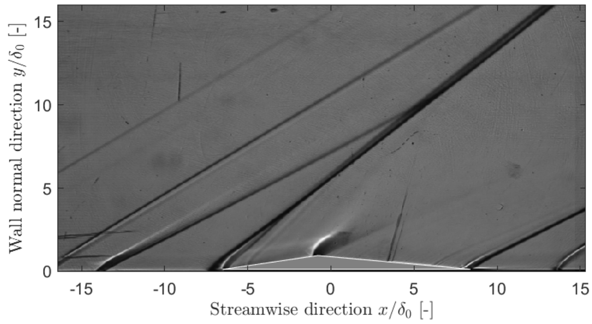

(a)

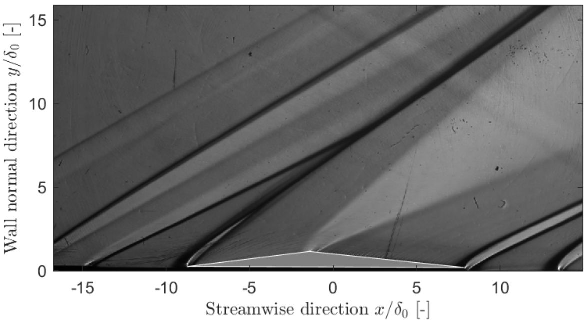

(b)

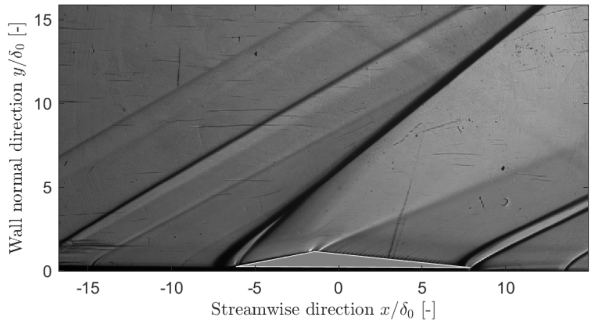

(c)

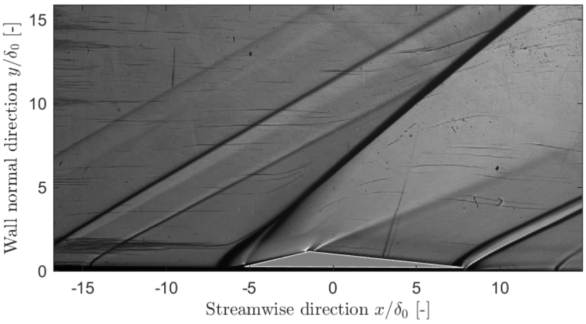

(d)

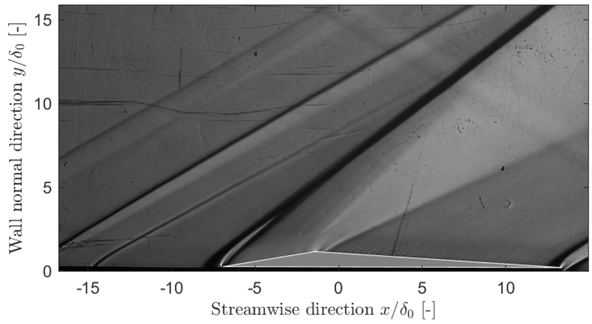

(e)

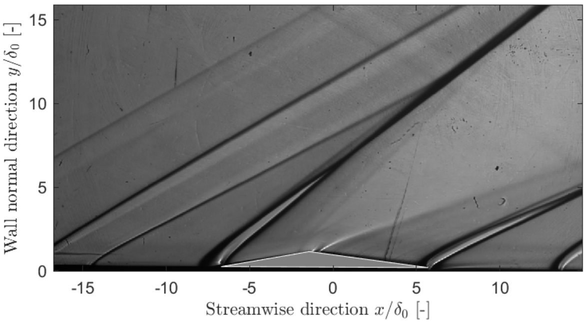

(f)

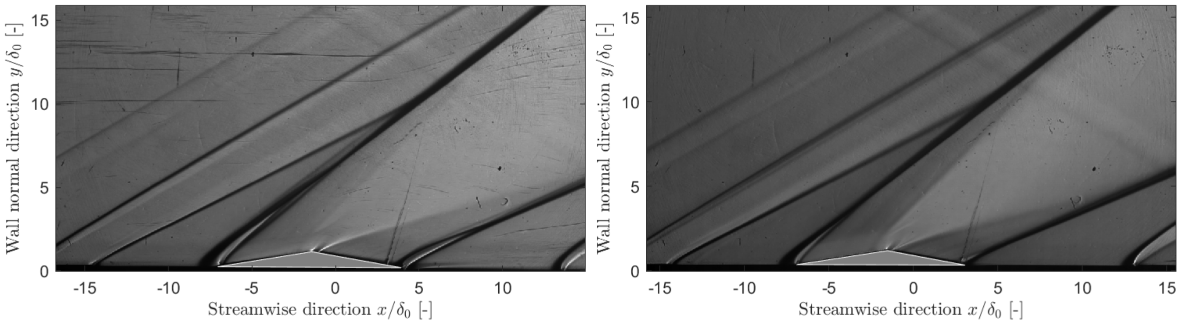

(g)

(h)

Figure A.1: Average Schlieren images of the Shock Control Bumps without impinging shock: a) Baseline, b) SCBr7t5.5, c) SCBr11t5.5, d) SCBr13t5.5, e) SCBr9t3.5, f) SCBr9t7.5, g) SCBr9t9.5, and h) SCBr9t11 bump. Spatial coordinates are normalised by the boundary layer thickness δ_0.

B

Spectral Analysis of Bump Geometry Variation

This appendix shows the pre-multiplied variance-normalised PSDs for the ramp and tail angle variation in terms of frequency instead of the interaction length-based Strouhal number $St_{L_{int}}$. Figure B.1 shows the spectral analysis for the ramp angle variation and Figure B.2 shows the analysis for the tail angle variation. Both figures include the baseline and uncontrolled interaction for comparison.

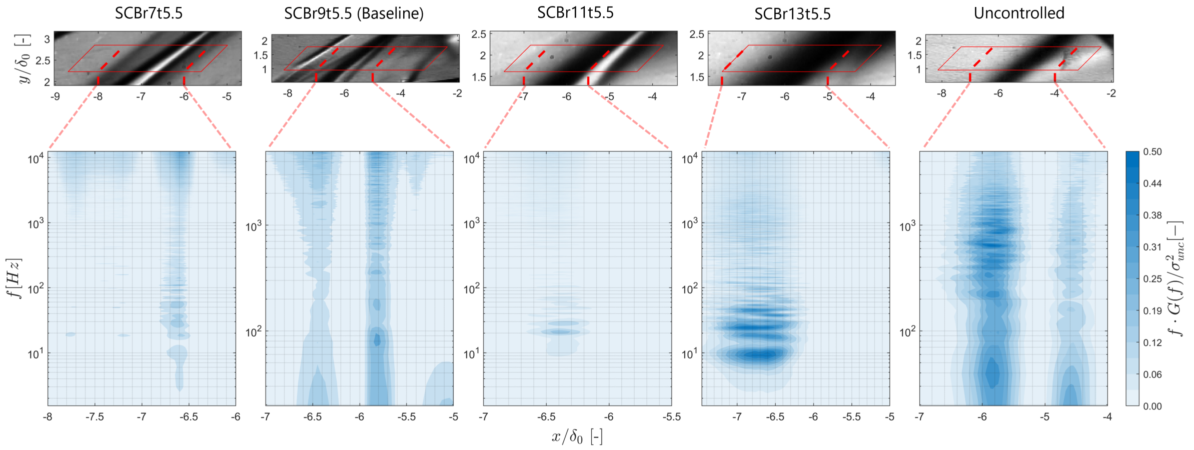

Figure B.1: Pre-multiplied variance-normalised PSD distribution ($K = 8$ segments, $f_s = 25$ kHz) of the bumps with ramp angle variation including the definition of the spectral boxes. The baseline and uncontrolled interaction are included for comparison ($L = 512$, $f_s = 10$ kHz). Distributions are in terms of frequency and the nondimensional streamwise direction x/δ_0.

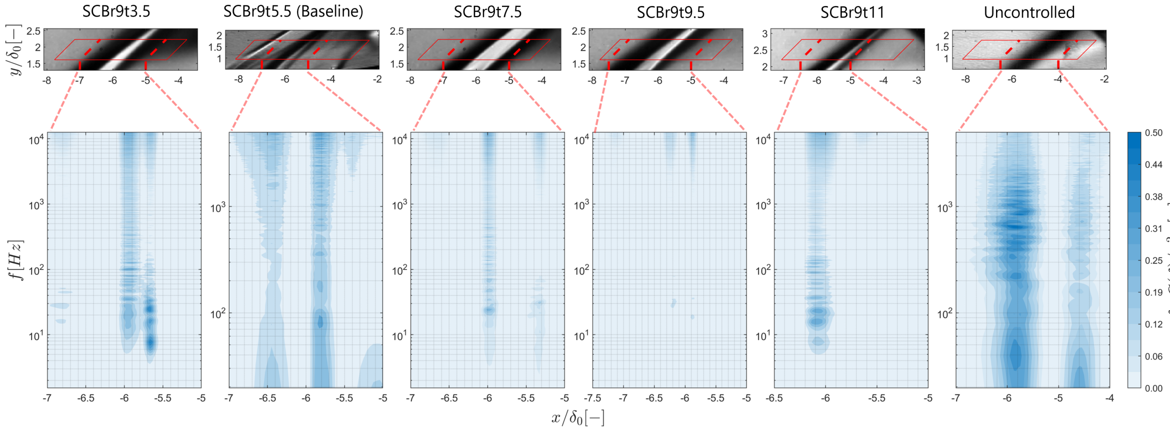

Figure B.2: Pre-multiplied variance-normalised PSD distribution ($K = 8$ segments, $f_s = 25$ kHz) of the bumps with tail angle variation including the definition of the spectral boxes. The baseline and uncontrolled interaction are included for comparison ($L = 512$, $f_s = 10$ kHz). Distributions are in terms of frequency and the nondimensional streamwise direction x/δ_0.

C

Test Matrices of Experimental Campaigns

This appendix states the test matrices used during the experimental campaigns. The matrices are twofold: the first for campaign A regarding the bump spanwise variation and the second for the SCB geometry alteration during campaign B.

Table C.1: Test matrix for experimental campaign A. Bump type: -) Uncontrolled interaction, 1) Baseline, 2) Short, and 3) Smooth bump.

Run no.	Date and Time	Technique	Bump type	T_0 [°C]	p_0 [bar]	Notes
1	14/10/2024 & 17:05	Schlieren	-	16.3	3	-
2	14/10/2024 & 15:45	Schlieren	1	15.2	3	The tape generates mach waves.
3	15/10/2024 & 10:18	Schlieren	2	19.1	3	-
4	14/10/2024 & 16:32	Schlieren	3	16.1	3	-
-	14/10/2024	Schlieren	-	-	3	Background Image
-	14/10/2024	Schlieren	1	-	3	Background Image
-	17/10/2024 & 9:09	Schlieren	1	-	3	Background image without shock generator for run no. 5.
-	15/10/2024	Schlieren	2	-	3	Background Image
-	14/10/2024	Schlieren	3	-	3	Background Image
5	17/10/2024 & 08:55	Schlieren	1	19	3	2D bump without shock generator
6	17/10/2024 & 14:47	OFV	-	17	3	Camera settings: 1/60, F22, iso 2200
7	17/10/2024 & 11:45	OFV	1	19	3	-
8	16/10/2024 & 16:00	OFV	2	19	3	Bump without tape to have better flow of the oil.
9	17/10/2024 & 16:00	OFV	3	17.5	3	Bump was blown away, but recording is sufficient.
10	18/10/2024 & 11:25	Schlieren	1	19	3	With shock generator moved downstream
11	18/10/2024 & 11:35	Schlieren	1	19	3	With shock generator moved upstream
12	18/10/2024 & 16:14	OFV	1	19	3	With SG downstream
13	18/10/2024 & 16:48	OFV	1	19	3	With SG upstream

Table C.2: Test matrix for experimental campaign B. Bump types: 1) SCBr7t5.5, 2) SCBr11t5.5, 3) SCBr13t5.5, 4) SCBr9t3.5, 5) SCBr9t7.5, 6) SCBr9t9.5, and 7) SCBr9t11.

Run no.	Date & Time	Technique	Bump type	T_0 [degrees C]	p_0 [bar]	Notes:
1	28/11/2024 & 17:05	Schlieren	1	19.5	3	Measurements on f_s = 25 [kHz], f = 300 [mm].
2	29/11/2024 & 9:03	Schlieren	2	18.5	3	
3	29/11/2024 & 9:50	Schlieren	3	17.1	3	
4	3/12/2024 & 12:15	Schlieren	4	17.7	3	
5	3/12/2024 & 11:19	Schlieren	5	19	3	
6	29/11/2024 & 10:23	Schlieren	6	18.7	3	
7	9/12/2024 & 10:37	Schlieren	7	19.1	3	
8	3/12/2024 & 14:04	Schlieren	1	17.7	3	Measurements without shock generator, f_s = 25 [kHz], f = 300 [mm].
9	29/11/2024 & 11:22	Schlieren	2	19	3	
10	29/11/2024 & 12:25	Schlieren	3	18.7	3	
11	3/12/2024 & 12:35	Schlieren	4	17.1	3	
12	3/12/2024 & 10:34	Schlieren	5	18.6	3	
13	3/12/2024 & 10:18	Schlieren	6	18.6	3	
14	9/12/2024 & 11:03	Schlieren	7	18.4	3	
15	-	Schlieren	1	-	3	Measurements on 80 [kHz], f = 200 [mm].
16	3/12/2024 & 16:01	Schlieren	**2**	17.5	3	
17	3/12/2024 & 16:23	Schlieren	**3**	17	3	
18	-	Schlieren	4	-	3	
19	3/12/2024 & 17:15	Schlieren	**5**	16.1	3	
20	3/12/2024 & 16:52	Schlieren	**6**	16.7	3	
21	6/12/2024 & 16:55	Schlieren	**7**	17.1	3	
22	5/12/2024 & 16:35	OFV	Uncontrolled	17.9	3	First a drop of oleic acid, then smearing it out, wipe off excess with a wipe, then oil with a smooth brush.
23	5/12/2024 & 17:00	OFV	1	18.7	3	
24	6/12/2024 & 9:55	OFV	2	18.7	3	
25	6/12/2024 & 11:45	OFV	3	17.5	3	
26	6/12/2024 & 12:54	OFV	4	17.7	3	
27	6/12/2024 & 14:44	OFV	5	17.5	3	
28	6/12/2024 & 15:15	OFV	6	17.7	3	
29	6/12/2024 & 15:51	OFV	7	17.4	3	